

Microrheology of crowded systems

Thesis submitted for the degree of
“Doctor of Philosophy”

By

Adar Sonn-Segev

Submitted to the Senate of Tel-Aviv University

November 2016

This work was carried out under the supervision of

Dr. Yael Roichman

And

Prof. Haim Diamant

School of Chemistry, Tel-Aviv University

Acknowledgements

This had been an amazing, fun, difficult and enlightening journey, and I am grateful to many people for their guidance, help, support, and friendship through it.

First and foremost, I owe great gratitude to my advisors, Yael Roichman and Haim Diamant, it was a privilege and an honor working with you. The last 6 years were like a roller-coaster ride, and your confidence in its successful end, together with the hours you both invested in nurturing, educating and supporting me professionally as well as personally, made this ride an outstanding experience.

I would like to thank all the members of the Roichman group: Maya, Dror, Kfir, David, Tal, Yulia, Elad, Omer, Barak, Tamir, Harel, Maayan and Lina. Thank you guys for creating a fun, stimulating environment to work, learn and grow in. In particular, I would like to thank David Kapfenberger for being a wonderful collaborator, in our joined work on holographic imaging and microrheology. It was always extremely fun working with you.

I am in debt to Anne Bernheim for our very fruitful collaboration on actin networks. Thank you for teaching me everything I know on actin, your specialty in actin and myosin, together with your work standard have influenced me greatly. I would like to thank the members of the Bernheim group, Orit, Barak, Anat, and Yaron. I am especially grateful to Yaron Ideses for teaching me how to work properly with myosin motors. I would also like to thank my collaborators abroad, Jerzy Blawdziewicz, Maria Ekiel-Jezewska and Elek Wajnryb. Their insights contributed considerably to our understanding of the behavior of sedimented particles.

Finally, I wish to thank my wonderful family. My love and gratitude goes to my parents Amos and Orit for their devoted support, love and faith in me always, and especially throughout this time. My warmest thanks are reserved for my best friend and my love, my husband, Gideon for always being there for me. Your support, help, encouragement, belief and love were an essential part of this journey. I love you and Danielle very much and look forward for our next adventure.

Abstract

This thesis describes the application of microrheology to characterize the structural, dynamical and mechanical properties of three soft, crowded materials: a quasi-two-dimensional colloidal suspension above a rigid wall, an entangled actin solution, and an active actin-myosin network. We demonstrate that by looking only at the fluctuations of particles embedded in a material, a large amount of information can be extracted regarding the structure, dynamics and mechanics of that material, and the relations between these properties.

The first system we investigated was a quasi-two-dimensional suspension of sedimented silica colloids above a planar substrate. We studied experimentally the structure and dynamics of the suspension as its density was increased, i.e., area fraction of particles was increased. This detailed investigation included 3D imaging by two independent techniques, holographic and confocal imaging, as well as 2D imaging by epi-fluorescence microscopy. The particles' location and motion were analyzed and revealed a rather sharp formation of a distinct second layer at an area fraction of ~ 0.3 , way below close packing. We found that this transition to a two-layer structure, which is driven by entropy, strongly affects the diffusivity of particles adjacent to the substrate, and its dependence on particle density. These experimental results were verified by simulations.

In the second set of experiments, we studied the microrheology of entangled F-actin networks, a model system for networks of semi-flexible polymers. A careful, high-precision analysis of two-point microrheology experiments led us to the discovery of a new regime of mechanical response in actin networks. This is despite the fact that the microrheology of actin networks had been extensively investigated earlier. The intermediate response was observed at surprisingly large distances of a few microns. It turned out to be of much more general nature, inherent to any two-component complex fluid. This discovery revealed that the bulk properties of complex fluids set in at distances much larger than the characteristic structural length-scale of the material (e.g., the mesh size of the actin network).

Subsequently, we utilized the discovery of the intermediate response to develop a new analysis scheme for microrheology experiments, based on the theoretical description of this regime. Using a combination of one-point and two-point microrheology, we were able to extract from the intermediate and bulk responses the dynamic correlation lengths of actin networks as a function of several parameters, such as concentration and filament length. This work has established a new characterization tool for complex fluids. Application of our new analysis scheme to entangled actin networks with increasing filament length enabled us to study the relation between dynamic and static correlation lengths. Contrary to the prevailing view, according to de Gennes, that the dynamic correlation length is equivalent to the structural mesh size of the network, we found that the dynamic correlation length starts increasing as soon as the filament length enters the newly discovered intermediate regime (i.e., when it is still much larger than the mesh size).

In the final set of experiments, we studied the fluctuations of particles in a model active soft matter system: an active actin-myosin gel. The non-equilibrium nature of these active networks was investigated as their activity was varied, either by increasing the motor concentration or by changing the size of the motor proteins. While analyzing the motion of embedded tracer particles, we observed that at sufficiently large concentration of myosin motor protein, the distribution of particles' step sizes features a sequence of distinct peaks at large displacements, indicating discrete events of motor activity. This observation is in contrast to the commonly found distributions, which feature Gaussian or exponential statistics. These peaks in the distributions are due to active processes in the networks, which have a cut-off distance, or a characteristic length-scale. We have performed simple simulations that reproduce these features and therefore support our interpretations of the results. We used these observations further to estimate the force that a single motor exerts on the network.

Contents

Acknowledgments	i
Abstract	iii
1 Thesis Outline	1
2 Introduction	7
2.1 Microrheology	7
2.1.1 Passive microrheology	8
2.1.2 One-point (1P) microrheology	15
2.1.3 MSD inversion procedures - connecting G^* to the MSD	15
2.1.4 Limitations of 1P microrheology	18
2.1.5 Two-point (2P) microrheology	23
2.1.6 Statistical considerations in microrheology experiments	27
2.1.7 Active microrheology	29
2.1.8 Applications of microrheology	30
2.2 Colloidal suspensions	33
2.2.1 Interparticle forces	34

2.2.2	Brownian motion	38
2.2.3	Hydrodynamic interactions	41
2.2.4	Colloidal suspension near a rigid surface	44
2.3	Cytoskeleton networks	46
2.3.1	Cytoskeleton filaments	47
2.3.2	Actin networks	48
2.3.3	Actin as a model system for semi-flexible polymers	49
2.3.4	Actin as a model system for cell mechanics	52
3	Articles	55
3.1	Structure and dynamics of sedimented colloidal suspensions	55
3.2	Viscoelastic response of F-actin networks at intermediate distances . .	56
3.3	Publications	57
4	Statistics of discrete motor-driven events in reorganizing active networks	77
4.1	Introduction	77
4.2	Material and sample preparation	80
4.3	Results and discussion	81
4.4	Conclusion	95
5	Summary and future directions	97
5.1	Colloidal suspension near a rigid wall	97
5.2	Actin networks	99
	Bibliography	103

Chapter 1

Thesis Outline

Particles suspended in a fluid move in a random jiggling manner. This motion, which is called Brownian motion, is named after the botanist Robert Brown, who first observed this in 1827. Only many years after Brown, was it understood that this eternal random dancing of particles is a result of thermal fluctuation in the fluid. A complete theoretical framework of this phenomenon was formulated by Einstein in 1905, which offered a compelling evidence for the atomic hypothesis. In this thesis we rely on these seminal insights to decode the jiggles resulting from thermal and active motion of particles in a variety of soft materials.

Soft matter constitutes a class of materials that show a complex behavior between those of viscous fluids and elastic solids, and that we encounter every day in the form of food, glues, soaps, digital displays, and, in fact, most materials of biological origin. Soft matter such as polymer networks, colloidal suspensions, surfactants and liquid crystals is made of subunits larger than single molecules, and its overall structures are governed by the interplay of thermal energy and weak interactions. As a result, these materials display a rich and fascinating range of behaviors. They are the basis of many modern technologies, and their study has already yielded new insights into condensed matter and fundamental physics in general.

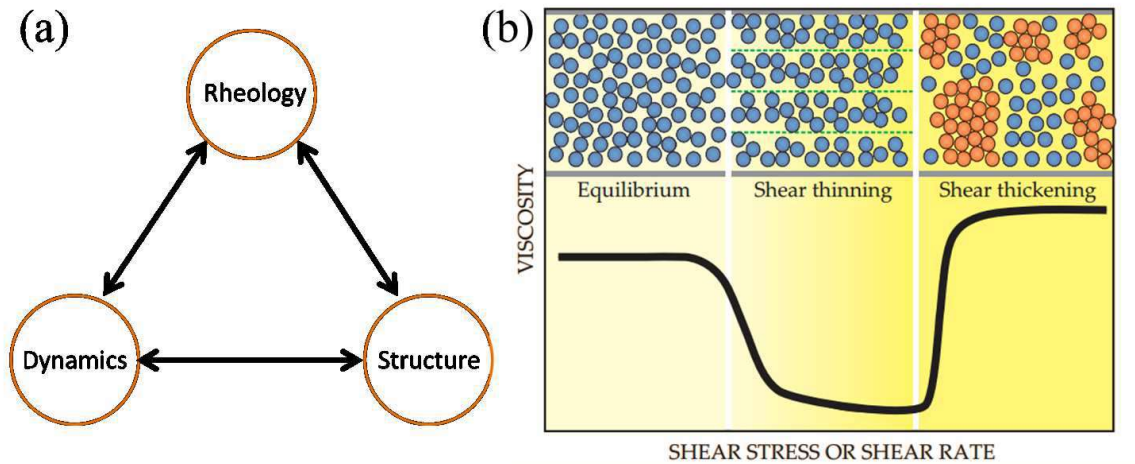


Figure 1.1: (a) Relationship between structure, dynamics, and rheology in soft matter. (b) An example of the relationships in the shear thinning-shear thickening transition in hard sphere colloidal suspensions. Adapted from [1].

Characterization of a soft material requires that the relationships between its structure, its equilibrium and non-equilibrium dynamics, and its rheology be determined. These categories, sketched in Fig. 1.1(a), are not independent. In most materials they are coupled, although not in a simple universal manner. A concrete example is the hard sphere colloidal suspension, illustrated in Fig. 1.1(b). In equilibrium, random collisions among particles (blue spheres) with liquid-like order make the suspension resistant to flow. As the shear stress or, equivalently, the shear rate increases, the particles become ordered into lane-like configurations. These lane-like configurations have a lower viscosity relative to the more randomized configurations. At yet higher shear rates, hydrodynamic forces between particles dominate over stochastic ones, a change that disrupts the order and creates clusters, i.e. transient fluctuations in particle concentration. The difficulty that particles have in flowing around each other in such a strong flow leads to a higher rate of energy dissipation and a sharp increase in viscosity [1].

An important way by which we learn about the structure and dynamics of soft matter is to probe them mechanically. Rheology is the study of the deformation

and flow of materials in response to an applied force. Simple solids store energy and provide a spring-like, elastic response, whereas simple liquids dissipate energy through viscous flow. Real materials, and especially soft materials, are neither ideal solids nor ideal liquids. Real soft materials exhibit both elastic and viscous responses and are therefore called viscoelastic. The internal structures of soft solids and complex fluids, composed of colloidal particles, filamentous polymers, and other supra-molecular arrangements, lead to complicated mechanical responses. As a result, the rheological response of these materials is not simply characterized by elastic and viscous constants; rather, these relations can be functions of time (frequency), direction, and extent of deformation. The goal of rheological experiments is to quantify the viscoelasticity of a material over as wide a range of time scales as possible and, ultimately, to relate these viscoelastic properties to the molecular meso- and macro- structure of the material. Twenty years ago, owing in part to innovations in digital video microscopy, it was realized that rheological information can be extracted from an analysis of the motions of micron-scale probe particles embedded in the material. This measurement technique, termed *microrheology*, has expanded the scope of materials and the range of length and time scales that can be studied mechanically. Importantly, microrheology has enabled the study of materials in situations wherein traditional rheometers are difficult to use, e.g., when the material is available only in very low quantities (< 1 mL). Moreover, microrheology has been useful in situations where removal of materials from their natural (in situ) contexts alters their ability to function, such as in living cells.

This thesis describes the application of microrheology, i.e., analysis of particle motion, to study the structural, dynamical and rheological properties of three soft matter systems. The first system is a monolayer of colloidal particles above a rigid surface. Such a suspension near a geometrical confinement is a good model system to study properties of many real-life scenarios, where particles are adjacent to a planar boundary, e.g., proteins near the cell membrane, or nanoparticles in microfluidic channels. In this system, we were interested in the structural and dynamical properties of the monolayer as it becomes more crowded, i.e., the density of the colloids in the monolayer increases. The second system is entangled actin networks. These

networks are excellent experimental models for semi-flexible polymers and the study of their properties has provided useful insights into the physics of semi-flexible polymers. We studied the microrheology of these networks at different crowded states, i.e., at increasing polymer concentrations, or increasing filament lengths. The third system is an active actin-myosin network. In contrary to the other two systems described above, this system is not in thermodynamic equilibrium, and consists of molecular motors that generate internal forces in the actin network, by the use of chemical fuel. Such active networks are used as model systems for the cytoskeleton, in order to study the underlying physical mechanisms of cellular mechanics. We were interested in the structure and dynamics of these networks as their activity is increased, i.e., the motor concentration and size are increased. Here the increase in motor activity created different crowding states.

One prominent character common to all the three systems is that they are crowded or dense solutions, composed of at least two-components, where there is a complex interplay between their structure, dynamics and rheology. Microrheology was the major experimental tool in my research. This technique is an umbrella term for various methodologies that characterize material properties through the correlation in motion of particles embedded in it. These correlations are both time and length-scale dependent, and include auto and cross correlations in particle motion.

This thesis is organized as follows. In Chapter 2 we introduce the theoretical foundations, practice and application of microrheology methodologies. A specific emphasis is given to microrheology because it was the main tool used in all of my projects, and was further generalized in our work to broaden its application. In addition, we introduce the three experimental systems which we have investigated.

In chapter 3 we review and present three peer-reviewed journal papers summarizing our investigation of the first two systems. The first article presents a comprehensive study on the structure and dynamics, including 3D imaging by two independent techniques, of a quasi-two-dimensional suspension of sedimented silica colloids above a planar substrate. This work revealed the rather sharp formation of a distinct second layer at an area fraction of only ~ 0.3 , much lower than the close

packing. This transition to a two-layer structure was found to strongly affect the diffusivity of particles adjacent to the substrate. The second article presents a careful investigation into the microrheology of entangled actin networks, which resulted in the discovery of a new regime of mechanical response at intermediate distances. Our work revealed that this intermediate response, which was observed at surprisingly large distances of a few microns, is of much more general nature, inherent to any two-component complex fluid. We generalized the framework of microrheology, based on the theoretical description of this regime, to include its response, and to extract the dynamic correlation length of actin networks. Our work has established a new characterization tool for complex fluids. The third article describes in detail this characterization tool, based on the new analysis scheme for microrheology experiments presented for the first time in the previous article. In addition, this article describes its application to relate the dynamic correlation length with the structure of actin networks. This was achieved by introducing another length scale, the average filament length, without altering the network's mesh size. We found that the dynamic correlation length starts increasing once the filament length is on the order of the size of the newly discovered intermediate regime (i.e., when it is still much larger than the mesh size). This finding is in contrast to the common view, according to de Gennes, that the dynamic correlation length and the static correlation length (mesh size in polymer networks) are equivalent.

Chapter 4 describes the unpublished study of the third system, active actin-myosin networks. The non-equilibrium nature of these active networks was investigated using embedded tracer particles. Contrary to the commonly found distribution of step sizes, which features Gaussian or exponential distributions, we observed a sequence of distinct "shoulders" in the distribution, indicating discrete events of motor activity. We used these observations further to estimate the force that a single motor exerts on the network.

A concluding discussion regarding our work is presented in chapter 5, where we recapitulate the main results which we have achieved, with special emphasis on further implications and applications of our work, and discuss its possible future directions.

Chapter 2

Introduction

2.1 Microrheology

Rheology is the study of the deformation and flow of material in response to applied stress. Simple solids store energy and provide a spring-like, elastic response, whereas simple liquids dissipate energy through viscous flow. For more complex viscoelastic materials, rheological measurements reveal both the solid- and fluid-like responses and generally depend on the time scale at which the sample is probed [2]. One way to characterize rheological response is to measure the shear modulus as a function of frequency. Traditionally, these measurements have been performed on several milliliters of material in a mechanical rheometer by imposing a small oscillatory mechanical strain and quantifying the resulting stress. Although conventional mechanical techniques have given valuable insight into the mechanical response of a wide range of materials, they work on bulk samples, hence precluding the study of rare or precious materials and many biological samples such as Actin, which are difficult to obtain in large quantities. Moreover, a conventional rheometer provides an average measurement of the bulk mechanical properties, not allowing more detailed measurement of local properties in inhomogeneous materials. In addition, the mechanical nature of a rheometer's measurements limits their frequency range, thus

preventing the characterization of high frequency regimes. To address these issues, a new class of microrheology methods has emerged, enabling the study of material response at micrometer length scales with microliter sample volumes [3]. Microrheology methods typically use embedded micron-sized probes to locally deform the sample. The use of small colloidal particles theoretically extends the accessible frequency range by shifting the onset of inertial effects to the MHz regime; in practice, the measurable frequency range varies with the details of the experimental apparatus. There are two broad classes of micro-rheology techniques: those involving the active manipulation of probes by local application of stress and those measuring the passive motions of particles due to thermal or Brownian fluctuations. The former is termed active microrheology, while the latter is termed passive microrheology.

In the following I will introduce the theoretical underpinnings of these methodologies. Much of the material on microrheology is covered in review articles [4, 5] and in Book chapter [6].

2.1.1 Passive microrheology

Passive microrheology techniques use Brownian dynamics of embedded colloids to measure the rheology and structure of a material. Tracer particles undergo diffusion in the medium they are embedded in due to thermal fluctuations. This behavior is often represented by the mean square displacement (MSD), a time dependent position correlation function of individual tracers. The MSD function is defined as

$$\langle \Delta \vec{r}^2(\tau) \rangle = \langle |\vec{r}(t + \tau) - \vec{r}(t)|^2 \rangle, \quad (2.1)$$

where \vec{r} is the d -dimensional particle position, τ the lag-time, and the brackets indicate an average over all particles and all times t . The time-averaging assumes the fluid is always in thermal equilibrium and the material properties do not evolve in time (ergodicity). For a spherical particle with radius a diffusing in a Newtonian fluid of viscosity η , the particle's MSD is related to the diffusivity D via $\langle \Delta \vec{r}^2(\tau) \rangle = 2dD\tau$ where

$$D = \frac{k_B T}{6\pi\eta a}. \quad (2.2)$$

Equation (2.2) is known as the Stokes-Einstein relation (SER) and is the theoretical cornerstone of all passive microrheology measurements. It asserts that measurements of a particle's thermally excited diffusivity can be used to extract the viscosity of the fluid, thus relating the dynamics of embedded tracer particles to the rheology of the medium. Owing to the importance of the SER in microrheology, it is useful to derive Eq. (2.2) from first principles. In order to do so, it is instructive to break the derivation down into two steps and critically examine the assumptions underlying each of the steps. The first step is to view Eq. (2.2) as a statement that a stochastic quantity (D) is related to the temperature times a deterministic, mechanical quantity (M), i.e. $D = k_B T M$, where M is the particle's mobility in the fluid. This is the Einstein part of Stokes-Einstein due to the fact that it was Einstein who considered it in 1905. The second step is relating the deterministic particle response (mobility, M) to the medium's rheological properties (fluid viscosity, η). M describes the relation between the velocity (v) of a particle embedded in the medium to a force (F) applied to it via $v = M \cdot F$. Solving the Stokes equations for a Newtonian fluid with viscosity η around a spherical particle of radius a yields the expression for the mobility, $M = 1/6\pi\eta a$. This result, first carried out by Stokes in 1851, comprises the Stokes part of Stokes-Einstein.

Finally, to apply this approach to viscoelastic materials, the SER is generalized to account for materials that do not behave as Newtonian fluids, namely their rheological properties are frequency-dependent and have real as well as imaginary parts.

Einstein component: relating diffusivity to mobility

Consider a collection of particles diffusing in one dimension, and let us define $c(x, t)$ as the concentration of the particles at a position x at time t . If this concentration is not spatially uniform, there will be a flux $j(x, t)$, which is proportional to the spatial gradient of the concentration. This flux is described by Fick's first law of diffusion:

$$j(x, t) = -D \frac{\partial c}{\partial x}, \quad (2.3)$$

where D is the diffusivity, or diffusion coefficient. Eq. (2.3) dictates that the flux of particles will always be from higher concentration regions to lower concentration regions, while in equilibrium the concentration is uniformly distributed and does not change over time. If there is an external potential $U(x)$ acting on the particles, then Fick's law must be modified. The potential exerts a force

$$F = -\frac{\partial U}{\partial x} \quad (2.4)$$

on the particles, producing a non-vanishing mean particle velocity v which, assuming the force is weak, is linearly related to F via the particle's mobility (M): $v = M \cdot F$. This average velocity of the particles in response to the external potential gives rise to an additional flux cv which should be added to Eq. (2.3), yielding a total flux of

$$j(x, t) = -D \frac{\partial c}{\partial x} - c \left(M \cdot \frac{\partial U}{\partial x} \right). \quad (2.5)$$

In equilibrium, the concentration must be independent of time and is given by the Boltzmann distribution:

$$c_{eq} \propto \exp \left(-\frac{U(x)}{k_B T} \right). \quad (2.6)$$

Detailed balance requires the net probability flux j to vanish in equilibrium, so that a particle in a potential field U obeys

$$j(x, t) = -D \frac{\partial c_{eq}}{\partial x} - c_{eq} \left(M \cdot \frac{\partial U}{\partial x} \right) = 0. \quad (2.7)$$

Solution of Eq. (2.7) using a concentration profile provided by Eq. (2.6) yields

$$D = k_B T M. \quad (2.8)$$

This expression, commonly known as the Einstein relation, connects a stochastic fluctuating quantity (diffusivity) to a deterministic mechanical property (mobility).

Stokes component: relating particle mobility to material rheology

The calculation of the functional form of mobility M is based on the Navier-Stokes equations, and was first obtained for a spherical particle steadily translating in a Newtonian fluid by Stokes in 1851 [7]. For low-Reynolds number flows, where viscous damping dominates over inertial effects, the Navier-Stokes and continuity equations as applied to fluid phases reduce to

$$\eta \nabla^2 \vec{u} = \vec{\nabla} p, \quad \vec{\nabla} \cdot \vec{u} = 0. \quad (2.9)$$

Here \vec{u} is the local velocity field of the incompressible flow far away from sources and sinks and p is the local pressure. Equations (2.9) are known as the Stokes flow equations and can be solved for \vec{u} and p by considering appropriate boundary conditions for the fluid at the probe particle surface (no-slip) and at infinity (unbounded) to relate the probe mobility to the viscosity of the medium. For a sphere of radius a translating through a fluid of viscosity η at constant velocity $\vec{v} = v \hat{x}$, Eqns.(2.9) yield the following solutions for \vec{u} and p :

$$\begin{aligned} \frac{u_\alpha(\hat{r})}{v} &= \frac{3a}{4} \left(\frac{\delta_{\alpha x}}{r} + \frac{x r_\alpha}{r^3} \right) + \frac{a^3}{4} \left(\frac{\delta_{\alpha x}}{r^3} + \frac{3x r_\alpha}{r^5} \right) \\ p(\vec{r}) &= \frac{3\eta a}{2} \frac{\vec{r} \cdot \vec{v}}{r^3}, \end{aligned} \quad (2.10)$$

where $\vec{r} = (x, y, z)$ is the vector distance from the center of the sphere.

Once solved for, the velocity field \vec{u} and pressure p can be used to determine the stress tensor $\sigma_{\alpha\beta}$ via

$$\sigma_{\alpha\beta} = -p \delta_{\alpha\beta} + \eta (\nabla_\alpha u_\beta + \nabla_\beta u_\alpha). \quad (2.11)$$

The viscous drag force on the particle (and consequently the mobility) is calculated by integration of the stress tensor ($\sigma_{\alpha\beta}$) over the particle surface:

$$F_\alpha = \int_S \sigma_{\alpha\beta} dS_\beta. \quad (2.12)$$

Substituting Eqns. (2.10) into Eqns. (2.11) and (2.12) and solving for the viscous drag ζ via $\vec{F} = \zeta\vec{v}$, we obtain $\zeta = 6\pi\eta a$, resulting in the Stokes mobility

$$M = \zeta^{-1} = (6\pi\eta a)^{-1}. \quad (2.13)$$

The ηa combination could have been guessed from simple dimensional analysis of the drag force; however, the prefactor 6π is a direct consequence of the no-slip boundary condition for the fluid velocity on the sphere's surface. Combining Eq. (2.13) with Eq. (2.8) yields the known Stokes-Einstein relation of Eq. (2.2). The next step is to generalize this relation to materials that are viscoelastic, having viscosity which is both frequency-dependent and complex ($\eta \rightarrow \eta^*(\omega)$).

Generalized Stokes-Einstein relation

The crucial assumption in the generalization of the Stokes mobility is that the functional form of the generalized Stokes mobility (GSM) $M^*(\omega)$ and the resistance $\zeta^*(\omega)$ is precisely the same as their Newtonian analogs, with the Newtonian viscosity η replaced by the material's frequency-dependent complex viscosity $\eta^*(\omega)$:

$$M^*(\omega) = \frac{\eta}{\eta^*(\omega)} M, \quad \text{or} \quad \zeta^*(\omega) = \frac{\eta^*(\omega)}{\eta} \zeta. \quad (2.14)$$

The basis of this assumption is within the underlying linearity of Stokes equations, Eqns. (2.9), which, when solved in the non-inertial regime, admit viscous and viscoelastic solutions exhibiting isomorphic correspondence [8]. Mason and Weitz [3] used this assumption to derive the relationship between the probe's MSD and $M^*(\omega)$, starting from a generalized Langevin equation describing the forces acting on a small particle of mass m and velocity $V(t)$ in a complex material:

$$m\dot{V}(t) = F(t) - \int_0^t \zeta(t - \tau)V(\tau)d\tau. \quad (2.15)$$

Here $F(t)$ represents random forces acting on the particle, including both the contributions of the surrounding fluid and those that are due to any interactions with any other particles or structures in the medium. The force is assumed to be a

Gaussian random variable with zero mean and to be completely decoupled from any past velocity. $\zeta(t)$ is the time-dependent hydrodynamic resistance, whose Laplace transform is the inverse of the mobility $\tilde{\zeta}(s) = \tilde{M}(s)^{-1}$. $\zeta(t)$ is also known as the time-dependent memory function, since it accounts for energy being stored by the elasticity of the medium and returned at a later time. This equation can be solved by taking the unilateral Laplace transform to obtain an expression for $\tilde{V}(s)$:

$$\tilde{V}(s) = \frac{mV(0) + \tilde{F}(s)}{ms + \tilde{\zeta}(s)}, \quad (2.16)$$

where $\tilde{V}(s)$ denotes the Laplace transform of $V(t)$ and s is the Laplace frequency. The first term in the denominator of Eq. (2.16) reflects the contribution of inertial effects, whereas the second term reflects viscous effects. Since F is a stochastic quantity, $V(t)$ should be treated statistically; therefore, Eq. (2.16) is multiplied by $V(t=0)$ and is ensemble-averaged to give:

$$\langle V(0)\tilde{V}(s) \rangle = \frac{m\langle V(0)^2 \rangle + \langle V(0)\tilde{F}(s) \rangle}{ms + \tilde{\zeta}(s)}. \quad (2.17)$$

Assuming that the random force is uncorrelated with the velocity, $\langle FV \rangle = 0$, and using the equipartition theorem, $\frac{1}{2}m\langle V(0)^2 \rangle = \frac{1}{2}k_{\text{B}}T$, we obtain the velocity autocorrelation for d -dimensional probe motion in the Laplace domain:

$$\langle V(0)\tilde{V}(s) \rangle = \frac{dk_{\text{B}}T}{ms + \tilde{\zeta}(s)}. \quad (2.18)$$

For low enough frequencies, the resistance $\tilde{\zeta}(s)$ dominates over the probe inertia (typically $< \text{MHz}$ for colloidal systems [9]) and Eq. (2.18) is reduced to

$$\langle V(0)\tilde{V}(s) \rangle \approx dk_{\text{B}}T\tilde{\zeta}^{-1}(s) = dk_{\text{B}}T\tilde{M}(s). \quad (2.19)$$

Finally, the Laplace transform of the velocity autocorrelation can be related to the MSD via the identity

$$\langle V(0)\tilde{V}(s) \rangle = \frac{s^2}{2}\mathcal{L}\{\langle \Delta\vec{r}^2(t) \rangle\} \equiv \frac{s^2}{2}\langle \Delta\vec{r}^2(s) \rangle, \quad (2.20)$$

where \mathcal{L} denotes Laplace transformation, to give

$$\langle \Delta \tilde{r}^2(s) \rangle \approx \frac{2dk_B T}{s^2 \tilde{\zeta}(s)} = \frac{2dk_B T}{s^2} \tilde{M}(s). \quad (2.21)$$

Equation (2.21) is also known as the Fluctuation-dissipation theorem connecting stochastic properties (MSD) to deterministic properties (M), and is more commonly written in terms of the frequency-dependent shear modulus $\tilde{G}(s) = s\eta(s)$, which is related to the probe mobility by $\tilde{M}(s) = (6\pi a \tilde{G}(s)/s)^{-1}$. The resulting expression is known as the Generalized Stokes-Einstein Relation (GSER):

$$\langle \Delta \tilde{r}^2(s) \rangle = \frac{dk_B T}{3\pi a s \tilde{G}(s)} \quad (2.22)$$

which is the basis for all passive microrheology methods. It can be recast into a more familiar form by the use of the transform of the time-dependent diffusion coefficient, defined as $D(t) = 1/2d\partial\langle\Delta r^2(t)\rangle/\partial t$, and the complex viscosity spectrum, $\tilde{\eta}(s) = \tilde{G}(s)/s$. When these are substituted into Eq. (2.22), the transformed diffusion coefficient takes a familiar form

$$\tilde{D}(s) = \frac{k_B T}{6\pi a s \tilde{\eta}(s)}. \quad (2.23)$$

In the limit of a freely diffusing particle in a purely viscous solution Eq. (2.23) reduces to the simple Stokes-Einstein relation (SER), and the frequency-independent viscosity can be recovered ($\eta_0 = k_B T/6\pi a D$), where D is the diffusion coefficient of the particle in the fluid.

An equivalent representation of Eq. (2.22) in terms of the Fourier components, more commonly encountered in oscillatory macrorheological data, can be readily obtained via analytic continuation $s = i\omega$. In practice, the Laplace or Fourier transformed MSD is typically not obtained directly from the time-domain data, since the dynamic range is limited to only a few decades in conventional measurement schemes. Instead, local power laws are used to approximate the time-domain MSD and the transforms are generated via algebraic expressions based on the values of the power law exponents. More details of this procedure will be given below, in Sec. 2.1.3.

2.1.2 One-point (1P) microrheology

The procedure described above interprets the dynamics of individual probe particles as a viscoelastic response. This technique has come to be known as one-particle (1P) passive microrheology (or one-point passive microrheology). In 1P microrheology the rheological properties are inferred from the self-diffusion of the tracer particles, and thus inherently sensitive to the local properties of the material, $\tilde{G}_\ell(s)$, rather than its bulk properties, $\tilde{G}(s)$. This feature (and consequently limitation) is further elaborated in the following section.

1P passive microrheology uses the generalized Stokes-Einstein relation (GSER),

$$\langle \Delta \tilde{r}^2(s) \rangle = \frac{k_B T}{\pi a s \tilde{G}_\ell(s)} \quad (2.24)$$

to determine the local shear moduli $\tilde{G}_\ell(s)$ from the measured single-particle mean-square displacement, $\langle \Delta r^2(\tau) \rangle \equiv \text{MSD}^{1\text{P}}$ [3]. Here $\langle \Delta \tilde{r}^2(s) \rangle$ is the Laplace transform of $\langle \Delta r^2(\tau) \rangle$ as a function of Laplace frequency s , a is the particle radius, and $k_B T$ is the thermal energy. Shear moduli and MSD may be readily converted between the Fourier, Laplace and lag time domains with simple numerical routines [3, 10]. These routines are discussed in the next section.

2.1.3 MSD inversion procedures - connecting G^* to the MSD

Image-based passive microrheology schemes typically report the MSD in terms of lag-time, i.e., $\langle \Delta r^2(\tau) \rangle$. In the previous section we defined the mathematical relationship [GSER - Eq. (2.22)] that allows analytical calculation of rheological properties from the MSD, a process called inversion. From Eq. (2.22) it is clear that in order to determine the frequency-dependent shear modulus, the MSD must first be converted to a frequency-space representation (Laplace or Fourier). The Laplace/Fourier Transform integral spans all times from zero to infinity, requiring data sets spanning this same interval in order to do the conversion exactly. Conventional image-based methods yield MSD data that are limited to < 5 decades of

temporal dynamic range, precluding direct numerical calculation of the transform using either numerical integration or Fast Fourier Transform (FFT) algorithms. In both cases, truncation of the data introduces substantial errors into the transformed MSD, particularly near the dynamic range extrema, which might then be propagated into the moduli.

One early approach attempted to overcome the problem by fitting an empirical functional form to either $\langle \Delta r^2(\tau) \rangle$ or $\langle \Delta \tilde{r}^2(s) \rangle$, and then using the empirical functional form with fitted parameters in place of the experimental MSD to compute the transform analytically [3]. This approach requires the choice of an arbitrary functional form, which potentially can distort the data by, for instance, smoothing out subtle features of the data. To overcome these weaknesses, approaches have been developed that instead estimate the transforms algebraically using local power law around a frequency of interest, ω , and retaining the leading term [11]:

$$\langle \Delta r^2(\tau) \rangle = \langle \Delta \tilde{r}^2(1/\omega) \rangle (\omega\tau)^{\alpha(\tau)}, \quad (2.25)$$

where $\langle \Delta r^2(1/\omega) \rangle$ is the magnitude of $\langle \Delta r^2(\tau) \rangle$ at $\tau = 1/\omega$ and

$$\alpha(\tau) = \left. \frac{d \ln \langle \Delta r^2(\tau) \rangle}{d \ln \tau} \right|_{\tau=1/\omega}, \quad (2.26)$$

is the power law exponent describing the logarithmic slope of $\langle \Delta r^2(\tau) \rangle$ at $\tau = 1/\omega$. In practice, the slope is obtained by fitting the logarithm of both the MSD and τ values at each τ point, in the local neighborhood of this τ . Equation (2.25) is an identity if the MSD is an exact power law, i.e., $\langle \Delta r^2(\tau) \rangle \sim \tau^\alpha$, therefore this equation is a good approximation for near-power-law functional forms of the MSD. For probe particles driven only by thermal energy, α must lie between $0 < \alpha < 1$. The bound values correspond to particles embedded in a Newtonian fluid ($\alpha = 1$) or Hookean solid ($\alpha = 0$). Using the evaluation of the unilateral Fourier transform and Eq. (2.25):

$$\langle \Delta r^2(\omega) \rangle = \int_0^\infty \langle \Delta r^2(\tau) \rangle e^{i\omega\tau} d\tau \approx \langle \Delta r^2(1/\omega) \rangle \int_0^\infty (\omega\tau)^\alpha e^{-i\omega\tau} d\tau, \quad (2.27)$$

leads to

$$\langle \Delta r^2(\omega) \rangle \approx (i\omega)^{-1} \langle \Delta r^2(1/\omega) \rangle \Gamma[1 + \alpha(1/\omega)] \cdot e^{-i\pi\alpha(1/\omega)/2}, \quad (2.28)$$

where Γ is the gamma function, $\Gamma(x) = \int_0^\infty \tau^{x-1} e^{-\tau} d\tau$. Substitution of Eq. (2.28) into the GSER of Eq. (2.22), with $s = i\omega$, yields

$$G^*(\omega) \approx \frac{k_B T}{\pi a \langle \Delta r^2(1/\omega) \rangle \Gamma[1 + \alpha(1/\omega)]} e^{i\pi\alpha(1/\omega)/2}, \quad (2.29)$$

for the complex shear modulus. The elastic (G') and viscous (G'') moduli are

$$\begin{aligned} G'(\omega) &= |G^*(\omega)| \cos[\pi\alpha(1/\omega)/2] \\ G''(\omega) &= |G^*(\omega)| \sin[\pi\alpha(1/\omega)/2]. \end{aligned} \quad (2.30)$$

Equations (2.30) provide physical intuition for the relation between the moduli in terms of the power law behavior of the MSD. For the case of a Newtonian fluid ($\alpha = 1$), the $G^*(\omega)$ is purely $G''(\omega)$, and for the second limit of Hookean solid ($\alpha = 0$), the $G^*(\omega)$ is purely $G'(\omega)$. Equations (2.29) and (2.30) are exact in the limit where the MSD has a purely power-law form. For other more general forms, these equations are an excellent approximation at lag times where the MSD is well approximated locally by a power-law. However, when the MSD contains regions of high curvature the error in the estimation of $G^*(\omega)$ can be $\sim 15\%$. Another limitation is that the weaker of the two moduli always contains larger error. To remedy these situations, empirically modified versions of Eqns. (2.30) have been developed which include second order logarithmic time derivatives of the MSD [12]. This modification helps to better account for curvature, gives a better estimate of the moduli in curved regions of the data, and improves the results for the weaker component of the modulus. The modified equations that are used for extracting the moduli are

$$\begin{aligned} G'(\omega) &= G(\omega) \left\{ \frac{1}{1 + \beta'(\omega)} \right\} \cos \left[\frac{\pi\alpha'(\omega)}{2} - \beta'(\omega)\alpha'(\omega) \left(\frac{\pi}{2} - 1 \right) \right] \\ G''(\omega) &= G(\omega) \left\{ \frac{1}{1 + \beta'(\omega)} \right\} \sin \left[\frac{\pi\alpha'(\omega)}{2} - \beta'(\omega)[1 - \alpha'(\omega)] \left(\frac{\pi}{2} - 1 \right) \right] \end{aligned} \quad (2.31)$$

where

$$G(\omega) = \frac{k_{\text{B}}T}{\pi a \langle \Delta r^2(1/\omega) \rangle \Gamma [1 + \alpha(1/\omega)] [1 + \beta(\omega)/2]}. \quad (2.32)$$

The second-order logarithmic time derivative of the MSD is denoted by $\beta(\omega)$, while $\alpha'(\omega)$ and $\beta'(\omega)$ denote the local first- and second-order logarithmic derivatives of $G(\omega)$, i.e., $\alpha'(\omega) = \frac{d \ln G(\omega)}{d \ln \omega}$ and $\beta'(\omega) = \frac{d^2 \ln G(\omega)}{d(\ln \omega)^2}$. Using simulated data it was estimated that the scheme described in Eqns. (2.31) and (2.32) can improve the maximum errors in the computation of $G'(\omega)$ and $G''(\omega)$ from 40% to 4% [12].

2.1.4 Limitations of GSER in 1P microrheology

One-point microrheology is a powerful tool to study the rheological properties of samples with extremely small sample volumes at frequencies inaccessible to bulk measurements. However, this technique has several limitations. Here we mention two important limitations related to the probed time-scales and the material's heterogeneous length-scale.

The first limitation is related to the range of frequencies over which the GSER of Eq. (2.24) is valid. Theoretical work by Levine and Lubensky [9] showed that the GSER describes the thermal response of a bead embedded in a viscoelastic medium within a certain frequency range, $\omega_c < \omega < \omega_i$. The lower limit, ω_c , is the time scale at which longitudinal, or compressional, modes become significant compared to the shear modes that are excited in the system. In bulk rheology, the applied strain has only a shear component, whereas the thermally driven probe particle responds to all of the thermally excited modes of the system, including the compressional modes of the elastic network. Consequently, the GSER would measure a different viscoelastic modulus $G^*(\omega)$ than bulk rheology. At frequencies lower than ω_c the network compresses and fluid drains from denser regions of the network to more rarefied regions in a sponge-like manner. Above ω_c , the network locks in with the incompressible fluid with the result that compressional modes are suppressed. Consequently, the GSER should measure the same $G^*(\omega)$ as bulk rheology. An estimate of the lower crossover frequency, ω_c , can be determined by

balancing local viscous and elastic forces. The viscous force per unit volume exerted by the solvent on the network is $\sim \eta\nu/\xi^2$, where ν is the velocity of the fluid relative to the network, η is the viscosity of the fluid, and ξ is the characteristic length scale of the elastic network. The local elastic force per unit volume exerted by the network is $G'\nabla^2u \sim Gu/a^2$ at the bead surface where G' is the elastic modulus of the network, u is the network displacement field and a is the radius of the bead. Force balance dictates that viscous coupling between the fluid and network will occur when $\eta\nu/\xi^2 > Gu/a^2$, leading to a crossover frequency

$$\omega_c \geq \frac{G'\xi^2}{\eta a^2}. \quad (2.33)$$

For typical soft materials studied using passive microrheology, with elastic modulus of $G \approx 0.1$ Pa, viscosity of $\eta \approx 0.001$ Pa·s, and characteristic length scale of $\xi \approx 0.1a$, this crossover frequency ω_c is approximately 1 Hz.

The upper frequency limit, ω_i , is the frequency at which inertial effects set in at the length scale of the bead size. Recall that one assumption in the derivation of the GSER in Eq. (2.19) was the neglect of inertia. Shear waves propagated by the motion of the tracer decay exponentially from the surface of the bead through the surrounding medium. The characteristic length scale of this decay is called the viscous penetration depth and it is proportional to $\sqrt{G^*/\rho\omega^2}$, where ρ is the density of the surrounding fluid and ω is the frequency of the shear wave [13]. When the viscous penetration depth becomes comparable to the size of the bead, inertial effects become significant and cannot be neglected [14, 15]. For a particle of radius a , this occurs at a frequency given by

$$\omega_i = \sqrt{\frac{G^*}{\rho a^2}}. \quad (2.34)$$

For typical soft materials studied using microrheology, with properties of $G^* \approx 0.1$ Pa, $\rho \approx 1000$ Kg/m³, and $a \approx 0.5$ μ m, this frequency is $\omega_i \approx 20$ kHz. From these analyses, we find under typical conditions a large frequency range $1 \text{ Hz} < \omega < 20 \text{ kHz}$ where the GSER accurately measures the shear modulus.

The second limitation of the 1P microrheology technique concerns the local inhomogeneities on the level of the probe particle. 1P microrheology assumes that the local environment of the bead reflects that of the bulk. This is true only if the medium is homogeneous on the scale of the particle size a . When the particle diameter is comparable to or smaller than the any length scale of structures in the medium, the tracers can move within small cavities and their motions are not only a measure of the viscoelastic response, but also of the effect of steric hindrances caused by the cavity walls [16] or the effect of cage-hopping dynamics between transient pores [17]. Interestingly, even if the tracer particle is larger than the mesh-size, if the network has another length-scale larger than the tracer, e.g. the filament length, 1P microrheology experiments describes an effective local environment that is different from the network's bulk properties [18]. This feature of 1P microrheology can be exploited to distinguished between the heterogeneities in structure or in the elasticity. Statistical techniques have been introduced for the interpretation of multiple particle-tracking techniques and mapping of spatial and temporal variation in mechanical response [16]. Furthermore, particles in similar microenvironments can be grouped together into a meaningful ensemble, and average rheological and structural properties can be obtained. This statistical framework revealed the heterogeneous probe statistics within agarose gels to result from true porosity, rather than heterogeneous elasticity [16]. By contrast, F-actin networks exhibited spatiotemporal heterogeneity [17]. Using this framework, it was shown that cross-linked poly-acrylamide gels exhibit heterogeneous elasticity [19].

In addition to the effect of probe particle size, physical or chemical interactions between the probe and the material can alter the local material environment and cause the one-particle response to reflect the local microenvironment rather than bulk rheology, regardless of bead size. Physical interactions, e.g. depletion and electrostatic, can alter the local environment and affect diffusivity in a measurable way. For example, colloids embedded in solutions of semiflexible polymers such as actin and DNA are surrounded by depletion zones of the order of the polymer correlation length [20], as evidenced by the depletion forces that such polymers establish between colloids [21,22]. In a theoretical calculation of the complex mobility $M^*(\omega)$ of

a spherical probe in a viscoelastic two-fluid material the probe-material interaction were modeled by surrounding the probe with a thin spherical shell with different material properties [9,23]. The computed self mobility $M^*(\omega)$ of a single probe was highly sensitive to the local material environment.

Chemical interactions between the embedded probe and sample are of much interest and are highly system dependent. For example, in studies with an uncross-linked flexible polymer solution, no effect of bead chemistry was found [12]. However, surface chemistry seems to have significant effects in contact with biopolymer networks [24], since the charged groups used to stabilize commercially available colloids react readily with many proteins, leading to nonspecific binding. In a study with F-actin networks, the bead chemistry was changed to either inhibit or encourage binding of actin to the bead surface [24]. The beads that prevented actin binding were insensitive to changes in the mechanical properties of the network. By contrast, beads that bound to actin filaments reflected the bulk properties of the networks more accurately. However, a precise control of protein adsorption onto the beads is usually hard to achieve. Moreover, there may be consequences to the binding of probe particles. In the worst-case scenario, there is significant aggregation of the probes and the macroscopic gel-like structures are significantly altered. In less extreme cases, the presence of the bead affects only the surrounding local network but the bulk properties are unchanged. In this case, it is possible to obtain a modulus from 1P microrheology but it is unclear whether the measured local modulus reports the bulk response.

Figure 2.1 shows schematic illustrations of several scenarios in which the embedded probe particle is either chemically inert and is larger (Fig. 2.1(a)) or smaller (Fig. 2.1(b)) than the network mesh size, or chemically adsorbed with controlled binding properties (Fig. 2.1(c)) or with nonspecific binding properties (Fig. 2.1(d)).

As described in detail above, the information extracted from a single-particle dynamics can be highly dependent on the microenvironment. To determine bulk rheology without consideration of surface chemistry or structure heterogeneity a slightly different approach is taken; this method is called two-point microrheology.

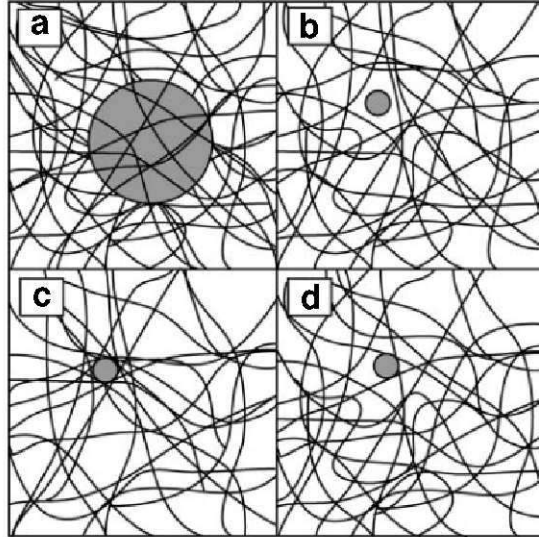


Figure 2.1: Sketch illustrating several physical scenarios for the way colloidal particles can be embedded in a network. Adapted from ref. 25. (a) Chemically inert particle with radius $a \gg \xi$, can provide information which is directly related to the linear viscoelastic moduli of the material. If the particle is larger than all important length-scales of the network (i.e. filament length, persistence length), the viscoelastic properties extracted from its motion reflect bulk properties; otherwise the motion reflects local viscoelasticity. (b) Particles with radius of $a \leq \xi$ which are resistant to protein adsorption can move within small microenvironments and their motion is sensitive to the viscosity of the solvent and hydrodynamic interactions with the network, but does not reflect the bulk viscoelasticity. (c) For $a \leq \xi$, sticky particles, which adsorb protein, recruit polymer filaments to their surface and possibly modify the local polymer concentration close to the sphere. In this scenario, particle motions do reflect network fluctuations; however, the tracers may sample unusually and artificially stiff regions of the network, leading to uncertainty in the interpretation of the particle dynamics and the network dynamics. (d) For $a \leq \xi$, even a small amount of protein adsorption can cause particles to adhere to the network filaments, leading to unusual coupling to the network dynamics, and hence to uncertainty in the interpretation of particle motion.

2.1.5 Two-point (2P) microrheology

Particles immersed in a fluid excite long-ranged flows as they move, and similarly move in response to fluid motion. By generating and reacting to a fluid's local velocity, colloidal particles experience hydrodynamic interactions with each other and with the walls of their container. These interactions, in turn, are dominated by large-scale properties of the material, rather than local regions surrounding the tracers that may arise due to sample inhomogeneity or boundary effects at the particle-material interface. These large-scale material properties are length-scale dependent and are effected by the material length-scale properties, which at large enough distances (larger than any important length-scale of the material) conform to the bulk properties which are measured by macrorheology. In 2000 a new technique was developed, called two-point (2P) microrheology [26], which takes advantage of the interparticle coupling to robustly extract bulk material properties. This technique eliminates motion due to purely local structure and mechanics by measuring the cross-correlated motion of pairs of tracers within the sample. The correlated motion of the particles at sufficiently large separations is not affected by the size of the tracer beads and is independent of the specific coupling between the probe and the medium. 2P microrheology directly maps the long-range deformation or flow of the material due to a single particle's motion. Since one tracer's strain field will entrain a second particle, we can measure the strain field by cross-correlating two tracers' motions. In a medium that is homogeneous at long length-scales, this strain field is proportional to the tracer motion and decays as a/r , where r is the distance from the tracer. Local heterogeneities, whether intrinsic to the material or created by the presence of the probe, will affect individual particle motions, but these effects will be uncorrelated at large distances.

In 2P microrheology the vector displacement of individual tracers is calculated, $\Delta r_\alpha(t, \tau) = r_\alpha(t+\tau) - r_\alpha(t)$, where t is the absolute time and τ is the lag time. Then the ensemble-averaged tensor product of the vector displacements is calculated:

$$D_{\alpha,\beta}(r, \tau) = \langle \Delta r_\alpha^i(t, \tau) \Delta r_\beta^j(t, \tau) \delta[r - R^{ij}(t)] \rangle_{i \neq j, t}, \quad (2.35)$$

where i and j label different particles, α and β label different coordinates, and

$R^{ij}(t)$ is the distance between particles i and j at time t . The average is taken over the distinct terms ($i \neq j$); the self term yields $\langle \Delta r^2(\tau) \rangle \times \delta(r)$, the one-particle mean-squared displacement ($\text{MSD}^{1\text{P}}$). The two-point correlation for particles in an incompressible continuum is calculated by treating each thermal particle as a point stress source and mapping its expected strain field [27].

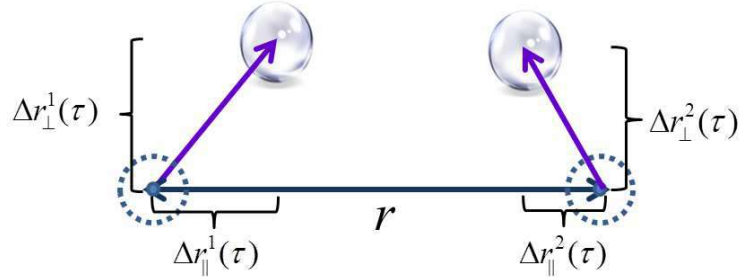


Figure 2.2: Schematic of two-point displacement components. In this sketch, the longitudinal component $D_{\parallel} = \langle \Delta r_{\parallel}^1(\tau) \Delta r_{\parallel}^2(\tau) \rangle$ is the product of the displacement component projected along the line separating the tracers by distance r . The transverse component $D_{\perp} = \langle \Delta r_{\perp}^1(\tau) \Delta r_{\perp}^2(\tau) \rangle$ is the product of the displacement component projected perpendicular to the line connecting the pair.

Spatially, $D_{\alpha,\beta}(r, \tau)$ can be decomposed into a longitudinal D_{\parallel} and transverse D_{\perp} components, where the former is the component of the motion along the center-to-center separation vector of the two tracers (see Fig. 2.2), while the latter is the component orthogonal to the separation vector. In an isotropic medium the off-diagonal component vanishes by symmetry. For an incompressible medium, to lowest order in a/r , the amplitudes of the two components are related via

$$D_{\perp} = \frac{1}{2} D_{\parallel}. \quad (2.36)$$

Typically, D_{\parallel} is the stronger component and hence easiest to measure in experiments from a signal-to-noise perspective.

The Brownian motion of a single probe is the superposition of all modes with wavelengths greater than the particle radius. The correlated motion of two particles with separation r is driven only by modes with wavelengths greater than the

separation distance. Therefore, two tracers that are separated by more than the coarse-grained length-scale in an inhomogeneous medium will depend on the coarse-grained, macroscopic complex modulus. If the strain field decay is $D_{\parallel}(r, \tau) \sim 1/r$ within a certain range of interparticle distances, the material can be treated as a homogeneous continuum at those length scales, and the shear modulus of the material can be determined using the relation [26]

$$\tilde{D}_{\parallel}(r, s) = \frac{k_B T}{2\pi r s \tilde{G}(s)}, \quad (2.37)$$

where $\tilde{D}_{\parallel}(r, s)$ is the temporal Laplace transform of $D_{\parallel}(r, \tau)$. It is instructive to derive Eq. (2.37) using the Oseen tensor analysis utilized in Ref. [28]. The overdamped Langevin equation with pairwise hydrodynamic coupling yields the equation of motion for a collection of N particles:

$$v_i(t) = \sum_{j=1}^N \mathbf{H}_{ij}(|\vec{r}_i - \vec{r}_j|) f_j(t) + \chi_i(t). \quad (2.38)$$

Here the velocity of particle i is the sum of self ($i = j$) and distinct ($i \neq j$) terms representing hydrodynamic coupling to deterministic external forces $f_i(t)$ as well as stochastic noise $\chi_i(t)$. The hydrodynamic interactions of the particles with the surrounding fluid are described by their hydrodynamic mobility tensor, H_{ij} , which is also known as the Oseen tensor, and has the components:

$$\mathbf{H}_{ii} = \frac{\mathbf{I}}{\zeta}, \quad \mathbf{H}_{ij}(r) = \frac{1}{8\pi\eta r} (\mathbf{I} + \hat{\mathbf{r}}\hat{\mathbf{r}}), \quad (2.39)$$

where $\zeta = 6\pi\eta a$ is the Stokes drag for a sphere in Newtonian fluid derived in Sec. 2.1.1, \mathbf{I} denotes the $d \times d$ -dimensional identity matrix, $\hat{\mathbf{r}}$ is a unit vector along the vector connecting the centers of two particles separated by a distance r . Equation (2.39) is derived from solving the Stokes flow equations and is essentially the Green's function for a point force solution [29]. The elements of the Oseen tensor in Eq. (2.39) are the leading order components ($O(a/r)$). The next-to-leading order components are $O[(a/r)^4]$ for the diagonal elements and $O[(a/r)^3]$ for the off-diagonal elements [30]. It is apparent from Eq. (2.39) that interparticle coupling does not depend on the radius of the particles, and its calculation does not

assume any boundary condition on the interface of particle-material [30]. Brownian forces are represented by the stochastic noise term $\chi_i(t)$ which satisfies the following correlations:

$$\langle \chi_i(t) \rangle = 0, \quad \langle \chi_i(t) \chi_j(t') \rangle = 2k_B T \mathbf{H}_{ij} (|\vec{r}_i - \vec{r}_j|) \delta(t - t'). \quad (2.40)$$

Equation (2.40) assumes that the random forces are consistent with Gaussian white noise with zero mean and also with the fluctuation-dissipation theorem (FDT). Explicitly, for two particles termed 1 and 2, Eq. (2.38) yields the coupled equations:

$$\begin{aligned} v_1(t) &= \mathbf{H}_{11} f_1(t) + \mathbf{H}_{12} f_2(t) + \chi_1(t) \\ v_2(t) &= \mathbf{H}_{21} f_1(t) + \mathbf{H}_{22} f_2(t) + \chi_2(t). \end{aligned} \quad (2.41)$$

In the absence of external forces $f_1(t) = f_2(t) = 0$, Eqns. (2.42) reduce to $v_i(t) = \chi_i(t)$. Computing the ensemble average of the cross-correlation $\langle v_1(t) v_2(t') \rangle$ yields

$$\begin{aligned} \langle v_1(t) v_2(t') \rangle &= \langle \chi_1(t) \chi_2(t') \rangle \\ &= 2k_B T \mathbf{H}_{12}(r_{12}) \delta(t - t') \\ &= \frac{k_B T}{2\pi\eta r_{12}} \delta(t - t'), \end{aligned} \quad (2.42)$$

where r_{12} is the distance between the two particles. Taking the Laplace transform of Eq. (2.43) and using the identity $\langle \tilde{v}_1(s) \tilde{v}_2(s) \rangle = s^2 \langle \Delta \tilde{r}_1(s) \Delta \tilde{r}_2(s) \rangle = s^2 \tilde{D}_{\parallel}(r, s)$ and the frequency generalization for complex fluids $\tilde{\eta}(s) = \tilde{G}(s) s^{-1}$ give the Generalized Stokes-Einstein relation for 2P microrheology described in Eq. (2.37). Significantly, Eq. (2.37) has no explicit dependence on the particle size, a , suggesting that it is independent of the tracer's size, shape and boundary conditions with the medium in the limit $r \gg a$. This is the advantage of 2P measurements that has enabled it to overcome the inhomogeneity issue that limited the application of the GSER in microrheology.

Comparing the longitudinal two-point correlation to the generalized Stokes-Einstein equation used in 1P microrheology suggests defining a new quantity: the two-point (2P) mean-squared displacement, $\text{MSD}^{2\text{P}}$, as [26]

$$\text{MSD}^{2\text{P}} = \frac{2r}{a} D_{\parallel}(r, \tau). \quad (2.43)$$

This is the thermal motion obtained by extrapolating the long-wavelength thermal fluctuations of the medium to the bead radius. If the material is homogeneous, isotropic on length scales significantly smaller than the tracer, incompressible, and connected to the tracers by uniform no-slip boundary conditions over their entire surfaces, the 2P mean-squared displacement will match the conventional 1P MSD. Any difference between them can provide insights into the local microenvironment experienced by the tracers [16, 31].

Unlike 1P microrheology, 2P microrheology is successful in determining the bulk rheological behavior of an inhomogeneous medium. This allows measurements in a larger range of materials that were previously inaccessible to 1P microrheology. Although 2P microrheology is an excellent technique to measure distance-dependent and bulk properties of materials, its application has not been as vast as 1P microrheology. The reason is the difficulties in extracting a reliable signal of the particles' displacement correlations which are due to statistical noise. The statistical considerations in microrheological experiments are discussed below.

2.1.6 Statistical considerations in 1P and 2P microrheology experiments

The statistical error in particle MSDs is readily estimated. If we approximate the distribution of tracer displacements as a Gaussian, the standard error for the variance is simply $2\langle x^2 \rangle / \sqrt{N_{\text{eff}}}$, where N_{eff} is the number of statistically uncorrelated measurements in the distribution. If an image series contains N_t tracers and spans a time interval T , then $N_{\text{eff}} \approx N_t T / \tau$. That is, if we image a single particle for 10 sec at 50 frames per second, we have roughly 500 independent samples of the displacement for a lag time of 1/50 sec, but only 10 independent samples for a lag time of 1 sec. All this assumes that the intrinsic correlation time of particle fluctuations is much smaller than τ , which is always valid in such measurements. This dependence

on τ causes the statistical errors to increase dramatically at longer lag times. As an example, if we were imaging a sample containing 100 tracers at 50 frames per second, and we wanted no more than 1% statistical error in the MSD over the lag times from 1/50 to 1 sec, then we would need $N_{\text{eff}} = 10^4$ independent samples at $\tau = 1$ sec. If we image 50 tracers in our field of view, then we need $T = 200$ sec of data. The large amount of information (5000 images and 500,000 tracer positions for this modest example) is efficiently analyzed by an automated image analysis software.

In general, 2P correlation functions have much higher statistical noise, requiring the acquisition of significantly higher statistical power, higher tolerance of noisier data, or both. The origin of this is straightforward to understand. The value of D_{\parallel} is the mean of a distribution of numbers $\langle \Delta r_1 \Delta r_2 \rangle$, since both Δr_1 and Δr_2 are single-particle displacements, the widths of the distributions of $\langle \Delta r_1 \Delta r_2 \rangle$ is roughly $\langle \Delta x^2(\tau) \rangle$, the conventional MSD in the limit of weak correlation. In general, the two-point correlated motion, D_{\parallel} , is much smaller than the single particle MSD. As shown above, under the most favorable case of incompressible homogeneous medium, the ratio of these two quantities according to Eq. (2.43) is $2r/a$, which typically has a value of 10-20. We then expect that reliable measurements of the 2P MSD would require averaging at least $(2r/a)^2$ or several hundred times [i.e., $(10 - 20)^2$] more $\Delta r_1 \Delta r_2$ measurements, relative to Δx^2 measurements to compute a conventional 1P MSD, in order to reach a similar statistical noise.

Fortunately, we are using video-based microscopy which enables us to image $\sim 100 - 200$ particles simultaneously. Each particle might have 10-20 neighbors within the proper distance range for computing 2P correlations. Thus, each image gives us not 100 samples of $\langle \Delta r_1 \Delta r_2 \rangle$, as for the example above, but more like several thousand. For this reason, the statistical noise of 2P measurements is highly sensitive to the number of tracers in the field of view. In general, if there are roughly 100 tracers in a microscope field of view, then about 10 times as many images are required to accurately compute a 2P MSD than a conventional 1P MSD. Alternatively, the statistical noise of the 2P measurement will be about $\sqrt{10}$, or just a few times higher than that of conventional 1P MSD computed from the same data.

It should be noted, however, that more statistical power is required for materials where the 1P MSD is much larger than the two-point MSD, according to the square of $\text{MSD}^{1\text{P}}/\text{MSD}^{2\text{P}}$ ratio. In highly porous materials, for example, the 2P signal can be so small compared to the background noise of uncorrelated tracer motion that it becomes hopelessly impractical to measure from a statistical point of view.

2.1.7 Active microrheology

So far we have focused on the basic theory of passive microrheology measurements utilizing broadband thermal energy to excite fluctuations that can be related to the material’s underlying linear rheology via the FDT. In this thesis we focus on this passive approach; however, it is worthwhile mentioning the complementary technique to passive microrheology, which is based on applying external forces to actively manipulate the embedded particles. This technique is called Active Microrheology. The forces are generated by the use of magnetic fields, electric fields, or micromechanical forces.

The principle of active microrheology measurements is the same as an oscillatory macroscopic rheometry measurement; however, there are several notable differences in practice. First, there is a difference in the length scales probed. Just as in the case of passive microrheology, the active microrheological measurement is more prone to the confounding effects of micron-scale inhomogeneities than macrorheology. In macrorheology the length scale of the deformation is much larger than any of the material’s intrinsic length scales, with the consequence that bulk rheology is always measured. However, the smaller length scale of active microrheology measurements has several advantages over macrorheology. For example, inertial effects, which arise at high frequencies when the viscous penetration depth is comparable to the sample thickness, can severely limit the upper frequency range of macrorheology measurements (typically < 100 Hz). The micrometer length scales of microrheology measurements enable probing of much higher frequency measurements, owing to the fact that the frequency criterion for the dominance of inertial effects is $\omega \geq \sqrt{G/\rho\ell^2}$ where G is the shear modulus, ρ is the density of the surrounding fluid, and ℓ is

the length scale of the shear deformation ($\ell = a$ for microrheology) [13,23]. Finally, a more subtle effect is that the strain field around an oscillating probe is not viscometric (shear-only) but rather contains both shear and extensional components. At low frequencies in viscoelastic gels, for example, fluid can freely drain from the network, effectively decoupling the two and causing micro/macro disagreement [23]. No analog occurs in macroscopic rheometry as the strain field is viscometric (pure shear).

Active microrheology inherits many of the features of passive microrheology, but offers at least one potential and significant advantage: because the FDT constrains passive microrheology to the materials' linear response, it is conceivable that active microrheology can be used to extend microrheology to characterize the non-linear rheology of complex fluids [32,33]. This could be accomplished using an optical trap, for example, by increasing the amplitude of the trap displacement to be much larger than the probe size over a duration much shorter than the Brownian relaxation time of the material. In addition, active microrheology can probe properties of active materials, such as active cytoskeleton networks [34]. This feature is another advantage over the passive technique that is again constrained by the validity of FDT. Any differences between properties measured using passive and active microrheology can be attributed to the internal active forces in these materials [34].

2.1.8 Applications of microrheology

The first and foremost application of microrheology is to measure the rheological properties of materials. The microrheology technique has several advantages in measuring rheological properties over the traditional, macrorheological measurements. First, the frequency range probed by microrheology can be extremely wide, extended in particular towards high frequency (\sim MHz). Secondly, microrheology measurements require only small volumes of samples (of $\sim \mu$ L), allowing to study materials that are not available in large quantities, such as proteins. In addition to samples volume, microrheological experiments can be conducted in non-conventional geometries, such as thin films, the interior of biological cells, membranes, and is not

restricted to the geometry of the mechanical rheometer. Thirdly, the probed samples can have very low viscosity (like water) and very low elasticity (tenuous gels), which in some rheometers cannot be studied. Another advantage is the price of equipment for microrheology experiments. The cost of a state-of-the-art rheometer is around \$100 000, whereas particle tracking can be carried out with a conventional optical microscope and a video camera for around a third of the price. Sample volume can be as small as 10 μL , compared to at least a few mL in traditional rheometers. This may also have the effect of reducing the cost of an experiment, or even making the experiment practically possible.

In addition to the original purpose and application of microrheology in measuring rheological properties of materials, several applications were developed extending the information that can be extracted from these experiments. Here we mention a few applications.

Since microrheology uses micron-sized tracer particles that locally probe the material properties, it is ideally suited for heterogeneous systems, where bulk methods give average distributions that are often very difficult if not impossible to deconvolve. Microrheology is not constrained to ensemble averages. Furthermore, careful analysis of 2P correlated motion can give length-scale and time-scale resolution of dynamical modes [18,35]. For example, Chen et al. used 1P and 2P measurements to distinguish between local and bulk material properties in a polymer solution, and thus to ascertain features of the depleted region around the tracer particles, and its relation to the polymer correlation length [35]. Microrheology can also give information on other forms of non-uniformity, for example the directional anisotropy in dense sheared DNA solution [36]. If spatial heterogeneity is found to be present, careful statistical analysis is required to test its significance. Individual particle movements must be considered since different particles may be exploring different microenvironments. Statistical techniques have been developed to compare the individual particles and map spatial and temporal variation in mechanical response [16]. Furthermore, particles in similar microenvironments can be grouped together into a meaningful ensemble and average rheological and structural properties can be obtained. It is also important to test trends in MSD as a function of bead size to

determine the nature of the constraints felt by the bead. For example, a plateau in the MSD that is observed at the long lag times indicates that the particles are constrained by the material. However, examination of the dependence of this plateau on particle size can reveal the nature of the constraint, i.e., if it is as a result of local elasticity of the material, or rather as a result of steric constraints, and report information regarding the size of the pores in the material.

Microrheology can also highlight physical processes in the material that would not be seen by any other bulk-averaged technique. Examples of the power of this method come from the study of inhomogeneous systems, where there can be a dependence of the rheology on the spatial length-scale, for example the effect of actin filament length on the rheology of entangled actin networks [18].

In 2P microrheology measurements, a comparison between the longitudinal component D_{\parallel} , and the transverse one, D_{\perp} , can give information on the compressibility of the material. In incompressible medium the ratio $D_{\perp}/D_{\parallel} = 0.5$, however the compressibility changes the anisotropy of the strain field, and modifies the relative amplitude of the tensor components (D_{\parallel}, D_{\perp}). Thus, measuring the ratio between the different tensor components should enable measurement of compressibility. In practice, it is possible to measure frequency and length-scale dependent compressibility using microrheology via this ratio $D_{\perp}/D_{\parallel} < 0.5$. It is important to note that the compressibility discussed here is of the overall fluid, including the solvent, and not only one of its components (e.g., the network).

In this thesis we describe our contribution to the applications of microrheology. First, by investigating the distance-dependent viscoelastic response of actin networks using 2P microrheology, we were able to discover a new regime of mechanical response at intermediate distances. In addition, based on the theoretical predictions of this regime we developed a new analysis scheme of microrheology experiments, combining 1P and 2P measurements, to characterize in more detail the mechanical response of complex fluids, and to measure their dynamic correlation length and structural properties.

2.2 Colloidal suspensions

The principal characteristic which determines if a particle is colloidal is its size, where this size range encompasses particles on the order of nanometers up to the micrometer scale. Colloidal suspensions are everywhere to be seen in our daily life: obvious examples are toothpaste, salad dressing and paint. Another example is molten chocolate, which is a colloidal suspension of sugar crystals and cocoa solids in oil. Finally, many biological systems can be viewed as colloidal suspensions, e.g., blood is a suspension of cells and globular proteins in water. In addition to the technological relevance of these suspensions, from a fundamental point of view colloids are excellent model systems to study questions of relevance in condensed matter physics, such as the phase behavior of fluids or fluid response to mechanical perturbations. The major benefit of colloidal systems arises from the mesoscopic particle size which allows convenient and non-invasive particle imaging with optical microscopes. One is therefore not restricted to the analysis of averaged physical quantities as typically obtained in scattering experiments on atomic matter. Moreover, particle-particle and particle-substrate interactions in colloidal systems can be both realized in a large variety and modified continuously.

There are a variety of forces brought to bear by the presence of colloidal particles within a fluid. Hydrodynamic, Brownian, and interparticle forces compete against one another to determine the dynamic and thermodynamic properties of the suspension [29]. Stability and phase behavior are governed by the balance between Brownian motion and interparticle forces such as electrostatic repulsion, and attraction due to dispersion forces. These interactions completely determine the suspension microstructure. In addition, when a boundary is present, e.g. a rigid wall, the structure and dynamics of the suspension is governed also by the boundary interactions with the colloidal particles. In order to deconvolve some of the forces present in such a system, a theoretical overview of individual forces and their role in determining the dynamics of the suspension is given below. The bulk of the theoretical overview will assume a monodisperse suspension of hard sphere colloids, which is a simplification, but relevant in many applications and in most of the stud-

ies discussed in this thesis. The polydispersity has an important consequence in sedimented suspension as described in the first article in Chapter 3.

2.2.1 Interparticle forces

Charged colloidal particles suspended in water interact through a variety of interparticle forces such as hard core repulsions, van der Waals attractions and Coulomb interactions. The particles' influence on the surrounding medium modifies these interactions, for instance leading to screening of Coulomb interactions by atomic-scale simple ions. In this section we concentrate on the static forces acting between particles, where the following sections discuss dynamic interactions.

Van der Waals forces

All atoms can be thought of as fluctuating dipoles because the electrons surrounding the nucleus do not form a uniform barrier or screen. The average distribution of charge around a molecule may be symmetrical, thus there is no net dipole moment. However, the electrons move about at any instant of time, resulting in an instantaneous distorted distribution of electron which creates a small dipole. The resultant, attractive force between atoms is known as a van der Waals force [29]. There are three kinds of interactions contributing to van der Waals forces: (i) interactions between thermally fluctuating permanent dipoles, known as Keesom forces; (ii) interactions between thermally fluctuating, induced and permanent dipoles, known as Debye forces; and (iii) interactions between quantum-mechanically induced dipoles, known as London forces. The long range attractive interactions between colloidal particles originate from London forces, where although the net permanent dipole moment may be zero, the induced interaction can produce a net attraction. These forces are proportional to the polarizability of the atoms and inversely proportional to the sixth power of the distance between two interacting atoms. Since the particles in a colloidal system are large compared to atomic dimensions, macroscopic interactions can be approximated by the summations of the pairwise interactions of

the constituent molecules in the individual particles. Therefore, the scaling up of van der Waals forces depends on the geometry of the particles involved.

For two spheres of equal radius, a , at a surface to surface separation distance, $K \ll a$, apart along the center to center axis, the total interaction energy, V_A , is given by [37]

$$V_A(K) = -\frac{A_H a}{12K}. \quad (2.44)$$

The quantity A_H is called the Hamaker constant, and contains information regarding the detailed potential energy between two atoms in the interacting spheres and the density of these spherical particles.

The overall van der Waals interactions are always attractive and contribute to the destabilization of colloidal suspensions. The stability of the suspension is provided by other repulsive interactions such as electrostatic and steric forces.

Electrostatic interactions

Particles that are dispersed in a fluid of high dielectric constant, such as water, usually develop charges on their surfaces. This surface charge can be a result of two possible processes: (1) ionization or dissociation of surface groups, which leaves behind a charged surface, and (2) adsorption (binding) of ions from solution onto a previously uncharged surface. The adsorption of ions from solution can also occur onto oppositely charged sites, also known as ion exchange. Since the system as a whole is electrically neutral, the dispersing medium must contain an equivalent charge of opposite sign. These charges are carried by ions, by an excess of ions of one sign on the particle surface and an excess of ions of the opposite sign in the solution. Hence, if we consider an individual particle immersed in the liquid, it is surrounded by an electric double layer, which consists of the charges on the surface of the particle and in the solution. As a result of thermal motion the electric charge carried by the layer in the solution extends over a certain distance from the particle surface, and dies out gradually with increasing distance into the bulk liquid phase.

Theories such as the Debye-Hückel approximation and Gouy-Chapman theory

have been used to explain the electrical double layer of colloidal suspensions. In this theory the average charge distribution and the corresponding electrical potential functions have been related on the basis of the Poisson-Boltzmann equation (PBE):

$$\nabla^2\psi = \frac{-1}{\epsilon_0\epsilon} \sum_i n_i^0 z_i e \exp\left(\frac{-z_i e\psi}{k_B T}\right), \quad (2.45)$$

where ψ is the electrical potential, n_i^0 the number density of ions of valency z_i , ϵ_0 the permittivity of vacuum, ϵ the dielectric constant of the fluid and e the elementary charge.

The derivation of Eq. (2.45) was done under several simplifying assumptions; (i) the electrolyte is an ideal solution with uniform dielectric properties, (ii) the ions are point charges, and (iii) the potential of mean force and the average electrostatic potential are identical. According to this theory, the average charge density at a given point can be calculated from the average value of the electrical potential at the same point with Boltzmann's theorem, and the electrical potential distribution can be related to the charge density with the aid of Poisson's equation.

Linearization of the Poisson-Boltzmann equation (Eq. 2.45) yields an approximate solution which is valid for weak potentials, i.e. $e\psi \ll k_B T$,

$$\psi(r) = \frac{Ze}{4\pi\epsilon_0\epsilon} \frac{\exp(\kappa a) \exp(-\kappa r)}{1 + \kappa a} \frac{1}{r}, \quad (2.46)$$

with r the distance from the center of the colloidal particle, and Z is the number of surface charges. The potential (2.46) constitutes the well known Debye-Hückel potential. Note that the finite geometry of the colloid is taken into account by the second factor which matches unity for point-like particles ($a = 0$). The inverse screening length κ is

$$\kappa = \sqrt{\frac{\epsilon_0\epsilon k_B T}{\sum_i e z_i^2 n_i^0}}. \quad (2.47)$$

When two like-charged particles approach each other, their electrical double layers will start to overlap, resulting in a repulsive force that opposes further approach. This pair interaction between colloids is obtained by linearly superimposing

Eq. (2.46) yielding

$$V_R(r) = \frac{Z^2 e^2}{4\pi\epsilon_0\epsilon} \left(\frac{\exp(\kappa a)}{1 + \kappa a} \right)^2 \frac{\exp(-\kappa r)}{r} \quad (2.48)$$

with r now the center-to-center distance between the colloidal particles. The last factor in Eq. (2.48) reflects the fast decay of the pair interaction with respect to the distance r originating from screening effects due to thermal motions of the mobile ions.

The DLVO theory, named after its developers: Derjaguin and Landau [38], Verwey and Overbeek [39], describes the force between charged surfaces interacting through a liquid medium. It combines the effects of the London-van der Waals attraction and the electrostatic repulsion due to the overlap of the double layers of counterions. The central concept of the DLVO theory is that the total interaction energy of two surfaces or particles is given by the summation of the attractive and repulsive contributions described above. This can be written as

$$V_T = V_A + V_R \quad (2.49)$$

where V_T is the total interaction energy. This theory successfully explains the long-range interaction forces observed in a large number of systems such as colloids, surfactant and lipid bilayers.

Steric forces

Steric stabilization is another method used to control the stability of colloidal suspension. Adsorbed organic molecules induce steric repulsion. The presence of the adsorbed layer has the effect of preventing the centers of the particles from coming closer than $2(a + \zeta)$, where a is the particle radius and ζ is the thickness of the adsorbed layer. In order to stabilize the suspension the thickness of the adsorbed layer ζ should be sufficiently thick in order to overcome the van der Waals attractive force.

Theories of steric interactions are not well-developed. There is no simple, comprehensive theory available as steric forces are specific, depending on molecular details of the adsorbed layer [40–42]. For example, the magnitude of the force between surfaces coated with polymers depends on the length and coverage of polymer on each surface, on whether the polymer is simply adsorbed from solution (a reversible process) or irreversibly grafted onto the surfaces, and finally on the quality of the solvent [40, 43]. Different components contribute to the force, and which component dominates the total force is situation-specific.

Although this repulsive interaction is complex, we can give several intuitive explanations for its mechanism. Generally, the steric mechanism has two effective elements which contribute to the overall colloidal stability. One is the osmotic contribution, relating to the increase in the local density of adsorbed molecules, which results in the diffusion of the medium into the region between the surfaces to reduce the concentration of adsorbed molecules at this region and thus to drive the particles apart. The second is the entropic contribution, relating to the reduction in the number of configuration of adsorbed polymer chains as particles get closer. This implies a reduction in the entropy of the system (ΔS) and hence an increase in the free energy (i.e., repulsion).

2.2.2 Brownian motion

In the preceding section we discussed the forces influencing the static properties of a colloidal suspension. In the two following sections we discuss the dynamic properties. These interactions between particles in suspension are mostly mediated by the fluid (in contrary to the static interactions which are direct), and hence are affected by hydrodynamic interactions. Here we describe the effect of interaction with the fluid in two sections, contributing to the motion of a single particle (Brownian motion), and influencing long-ranged correlations in suspensions (hydrodynamics).

Due to their size, colloidal particles are impacted by the motion of the suspending fluid molecules, creating a stochastic particle motion called Brownian mo-

tion. The Langevin equation describes the motion of such a colloidal particle. The equation has two contributions - a deterministic part describing friction forces from the fluid, and a random part arising from the fluctuating part of the force. For a spherical particle of radius a in a Newtonian fluid of viscosity η and density ρ , the one-dimensional Langevin equation describing its motion is [29]

$$m \frac{d^2x}{dt^2} + \zeta \frac{dx}{dt} = F(t), \quad (2.50)$$

where $x(t)$ is the particle position at time t , $m = 4\pi a^3 \rho / 3$ is its mass, $\zeta = 6\pi\eta a$ is the friction coefficient (also described before as hydrodynamic resistance) and $F(t)$ is the random fluctuating Brownian force. The function $F(t)$ represents the effect of collisions between the particle and the fluid molecules, and is assumed to be random in direction and magnitude and uncorrelated on the time scale of particle motion:

$$\langle F(t) \rangle = 0, \quad \langle F(t)F(t') \rangle = \Lambda \delta(t - t'), \quad (2.51)$$

where Λ is the noise intensity. The value of noise intensity can be determined by the equipartition theorem, which assumes that the kinetic energy is equally partitioning among the translational modes of the particle (in the present case only one mode) so that

$$\frac{1}{2}m \left\langle \left(\frac{dx}{dt} \right)^2 \right\rangle = \frac{1}{2}k_B T. \quad (2.52)$$

In the limit of $t \rightarrow \infty$, the result for the mean squared velocity from Eq. (2.50) is,

$$\left\langle \left(\frac{dx}{dt} \right)^2 \right\rangle = \frac{1}{m^2} \int_0^t dt' \int_0^t dt'' e^{-\zeta(t-t')/m - \zeta(t-t'')/m} \Lambda \delta(t' - t'') = \frac{\Lambda}{2m\zeta}. \quad (2.53)$$

Combining Eqns. (2.52) and (2.53) yields the value of $\Lambda = 2\zeta k_B T$, which relates the strength of the random Brownian fluctuations to the frictional forces that dissipate the energy. Both originate from the interaction between the particle and the solvent molecules, but differ substantially in time scales.

A typical experiment observing the Brownian motion of a particle is conducted at time scales much larger than the viscous relaxation time, $\tau_c \propto \rho a^2 / \eta$, thus it is

useful to derive the ensemble properties arising from the Langevin equation in terms of displacements rather than velocities.

Solution of Eq. (2.50) leads to a form for the mean squared displacement of a particle in the x -direction of

$$\langle x^2(t) \rangle = \int_0^t dt' \int_0^t dt'' \left\langle \frac{dx}{dt}(t') \frac{dx}{dt}(t'') \right\rangle = \frac{2m}{\zeta} \left\langle \left(\frac{dx}{dt} \right)^2 \right\rangle \left[t - \frac{m}{\zeta} (1 - \exp(-\zeta t/m)) \right]. \quad (2.54)$$

In the short time limit, $t \ll \tau_c$, Eq. (2.54) can be expanded via a Taylor series, yielding

$$\langle x^2(t) \rangle = \frac{2m}{\zeta} \left\langle \left(\frac{dx}{dt} \right)^2 \right\rangle t + \left\langle \left(\frac{dx}{dt} \right)^2 \right\rangle t^2. \quad (2.55)$$

This is called the ballistic regime.

In the limit of long times, $t \gg \tau_c$, Eq. (2.54) combined with Eq. (2.53) reduces to the familiar equation:

$$\langle x^2(t) \rangle = \frac{2m}{\zeta} \left\langle \left(\frac{dx}{dt} \right)^2 \right\rangle t = 2 \frac{k_B T}{\zeta} t = 2Dt, \quad (2.56)$$

where $D = k_B T / \zeta$ is the diffusion coefficient described in the previous sections. This equation is one of the most useful equations in experiments with colloidal suspensions. Extracting the diffusion coefficient, and assuming $\zeta = 6\pi\eta a$ for spherical particles, allows to measure the viscosity of the liquid in which the colloids are embedded (which is the basis of microrheology as described in the previous sections). It is important to note here that as the density of the colloidal suspension is increased the diffusion coefficient extracted from the mean square displacement of the particles is decreased, which is due to a different, effective viscosity of the suspension. This effective viscosity of the whole suspension (colloids and solvent) increases as the density of the colloidal particles is increased. The leading (linear) effect of a volume fraction ϕ of hard spheres on the viscosity of the bare liquid, η_0 , was calculated by Einstein [44], and found to be,

$$\eta = \eta_0 \left(1 + \frac{5}{2} \phi \right). \quad (2.57)$$

2.2.3 Hydrodynamic interactions

Particles immersed in a fluid excite long-ranged flows as they move, and similarly move in response to fluid motion. By generating and reacting to the fluid's local velocity, colloidal particles experience hydrodynamic interactions with each other and with the walls of their container. This section will focus on these interactions. In colloidal suspensions, the relative particle-fluid motions generate hydrodynamic forces that strongly influence the dynamic properties of the suspension. The disturbance caused by the motion of one particle decays so slowly with distance that interparticle effects are seldom negligible, and therefore hydrodynamic forces transmitted from one particle to another through a viscous fluid must be taken into account.

The equations describing the properties of fluid flow are the Navier-Stokes equations, which describe the velocity, the pressure and the mass of the fluid flow. These equations can be derived by considering two quantities which are conserved in an isothermal fluid flow, mass and momentum. From mass conservation we have:

$$\frac{\partial \rho}{\partial t} + \nabla \cdot (\rho \vec{u}) = 0, \quad (2.58)$$

where $\rho(\vec{r}, t)$ is the mass density of the fluid, and $\vec{u}(\vec{r}, t)$ is its velocity, at position \vec{r} and time t . For an incompressible fluid, which has constant density, Eq. (2.58) reduces to

$$\nabla \cdot \vec{u} = 0. \quad (2.59)$$

The equation for the conservation of momentum is

$$\rho \frac{d\vec{u}}{dt} = \rho \left[\frac{\partial \vec{u}}{\partial t} + (\vec{u} \cdot \nabla) \vec{u} \right] = \vec{F} - \nabla p + \eta \nabla^2 \vec{u} + \left(K + \frac{1}{3} \eta \right) \nabla (\nabla \cdot \vec{u}), \quad (2.60)$$

where $p(\vec{r}, t)$ is the pressure, $\vec{F}(\vec{r}, t)$ is an external force density, K and η are the compression and shear viscosities respectively. In the case of incompressible fluid, Eq. (2.60) reduces to the more familiar form

$$\rho \left[\frac{\partial \vec{u}}{\partial t} + (\vec{u} \cdot \nabla) \vec{u} \right] = \vec{F} - \nabla p + \eta \nabla^2 \vec{u}. \quad (2.61)$$

This non-linear equation can be further simplified in the case of a very viscous fluid where inertial effects of the fluid are negligible. This regime of behavior is also known as the low-Reynolds number regime. The Reynolds number is a dimensionless number $Re = \rho UL/\eta$, which describes the ratio between inertial and viscous forces, where L is a typical length in the system and U is a typical velocity. Low values of Re indicate negligible inertial effects and Eq. (2.61) becomes linear and simpler to handle,

$$\eta \nabla^2 \vec{u} - \nabla p + \vec{F} = 0. \quad (2.62)$$

This equation, together with the equation derived from mass conservation (Eq. (2.59)) are known as the Stokes equations, and are similar to Eq. (2.9) from Sec. 2.1.1. In the previous section, we discussed the leading order term of the solution to the linear equation, i.e., point force. In this section we first elaborated on the derivation of this linear equation and we further consider higher order terms of the solution, i.e., taking into account the size of the tracer particle $a > 0$. All the studies described in this thesis are in the regime of low-Reynolds number and, therefore, we concentrate our attention on it.

The linear equation can be solved by considering the classical Stokes problem of a rigid sphere of radius a , driven by a steady force \vec{F} through an incompressible fluid of viscosity η [45]. The fluid velocity at position \vec{r} away from the sphere's center is given by

$$\vec{v}(\vec{r}) = \vec{v}_1 + \vec{v}_2, \quad (2.63)$$

with

$$v_{1\alpha} = \frac{1}{8\pi\eta r} \left(\delta_{\alpha\beta} + \frac{r_\alpha r_\beta}{r^2} \right) F_\beta \quad (2.64)$$

$$v_{2\alpha} = \frac{a^2}{24\pi\eta r^3} \left(\delta_{\alpha\beta} - \frac{3r_\alpha r_\beta}{r^2} \right) F_\beta, \quad (2.65)$$

where Greek indices denote the coordinates (x, y, z), and repeated indices are summed over. The dominant term at large distances, \vec{v}_1 , is the flow due to a force monopole \vec{F} . Its $1/r$ decay is dictated by momentum conservation, ensuring that the integrated momentum flux (proportional to $\vec{v}_1 \sim r^2$) through any closed surface

around the sphere remain fixed. This dominant response can be decomposed into longitudinal and transverse components (force and velocity parallel and perpendicular to \vec{r} , respectively),

$$v_{1\parallel} = \frac{1}{4\pi\eta r} F_{\parallel} \quad v_{1\perp} = \frac{1}{8\pi\eta r} F_{\perp}, \quad (2.66)$$

both of which are positive. This dominant response is the Oseen tensor, mentioned previously in the section describing 2P microrheology (Sec. 2.1.5). It holds as long as momentum is conserved in the system. Turning to the correction term, the subdominant \vec{v}_2 , we point out the largely overlooked fact that it is actually made of two contributions, having the same spatial form but opposite signs and different physical origins, $\vec{v}_2 = \vec{v}_{2f} + \vec{v}_{2m}$. The first term is the flow due to a force quadrupole (a correction to the force monopole), whose longitudinal and transverse components are

$$\vec{v}_{2f} = 3\vec{v}_2, \quad v_{2f\parallel} = -\frac{a^2}{4\pi\eta r^3} F_{\parallel}, \quad v_{2f\perp} = \frac{a^2}{8\pi\eta r^3} F_{\perp}. \quad (2.67)$$

The second contribution to the subdominant term is due to a mass dipole created opposite to the direction of the sphere's displacement. It originates from mass conservation (rather than momentum like the two terms described above). Its longitudinal and transverse components are:

$$\vec{v}_{2m} = -2\vec{v}_2, \quad v_{2m\parallel} = \frac{a^2}{6\pi\eta r^3} F_{\parallel}, \quad v_{2m\perp} = -\frac{a^2}{12\pi\eta r^3} F_{\perp}. \quad (2.68)$$

In a simple Newtonian fluid, where the only important characteristic length scale is the particle size a , these two contributions to the subdominant term are summed up to a net negative correction to the longitudinal response, $\vec{v}_{2\parallel} = -a^2(12\pi\eta r^3)^{-1}F_{\parallel}$, and a positive correction to the transverse one, $\vec{v}_{2\perp} = -a^2(24\pi\eta r^3)^{-1}F_{\perp}$. Interestingly, in complex fluids or concentrated colloidal suspensions, which always have an intrinsic length scale (e.g., mesh size or correlation length in the suspension), there is a difference between the two terms of the above subdominant response. The force quadrupole depends on the bulk properties of the material η_{bulk} , as it derived from momentum conservation. However, the mass dipole term is related to mass conservation, arising from motion of mass in the local environment of the particle, and

it depends, therefore, on the local response of the material, with η_{local} . (Although it is related to the local environment, it is still long range.) If the local and bulk properties are not the same (and usually the local properties are softer than the bulk as they are related to the properties of the solvent), the two terms separate into two different contributions, and a new regime of mechanical response emerges, the intermediate response, whose origin is from mass conservation. This new regime was predicted theoretically [46] and in this thesis we describe its experimental observation and verification for the first time.

The above description of the static and dynamic interactions in colloidal suspensions is correct for an unbounded suspension. In one part of this thesis we describe the study of the structure and dynamics of suspensions adjacent to a rigid substrate. The proximity to a rigid wall adds static interactions between the colloids and the wall. In addition, it alters the particles' Brownian motion and hydrodynamic interaction, mainly because in fluid flow near a rigid wall momentum is not conserved. In the next sections we describe the characteristics of such suspensions.

2.2.4 Colloidal suspension near a rigid surface

In a wide range of practical scenarios, a suspension of particles is in close proximity to a geometrical confinement, for example diffusion near the cell membrane or in microfluidic channels. For such cases the description of forces presented above requires modifications in order to characterize correctly the suspension's properties. To a first approximation, these scenarios can be modeled as a colloidal suspension adjacent to a rigid wall.

The interactions between the colloidal particles and the rigid surface has two contributions; one, which is relatively simple, is from the static forces between the surface and the particles. For example, the van der Waals and electrostatic forces are modified to correctly describe the interaction between a colloid and an infinite wall. The second, and more complicated contribution, is to the dynamical interactions which are modified as a result of the disturbed fluid flow in the presence of an

infinite wall. The calculation of this flow field depends profoundly on the boundary condition at the surface of the wall. The simplest case is a wall whose surface can be considered as a no-slip boundary, i.e., the velocity of the fluid at the surface of the wall is zero. This condition dictates that there is a momentum loss to the rigid wall. Here we mention several static and dynamical properties of such suspensions near a rigid wall.

The electrostatic interaction between a colloid and a wall can be described as [29]

$$U_R(h) = B \exp(-\kappa(h - a)), \quad B = \frac{Z^2 e^2}{4\pi\epsilon_0\epsilon\kappa^2 a^3} \left(\frac{\kappa a}{(1 + \kappa a)} \right)^2, \quad (2.69)$$

where h is the distance between the center of the particle and the wall. This exponential decay was verified experimentally by recording the fluctuation of a colloidal particles near a wall [47]. The van der Waals interaction between a colloid and a infinite wall is [37]

$$U_A(K) \approx -\frac{A_H a}{6K}. \quad (2.70)$$

This expression is correct in cases where $a \gg K$, where K here is the surface-to-surface distance. In most practical scenarios, the colloidal particles are well separated and this VDW interaction can be neglected.

The overall structure of a colloidal suspension near a wall, which is determined from all particle-particle and particle-wall static forces, results in a disruption of the typical 3D structure of the unbounded suspension. This disruption can be, for example, in the form of a layered structure decaying away from the surface [48, 49].

The dynamical properties of a suspension near a wall are influenced by the flow field around a moving sphere. A no-slip boundary condition at the wall modifies this flow, breaking its symmetry and increasing the drag on the sphere. Faxén introduced the method of reflections in 1927 to address this question and obtained the mobility (and, hence, diffusivity) for a sphere at height h above a wall, moving parallel to the surface [45]

$$D_{\text{wall}}(h) = D_0 \left\{ 1 - \frac{9}{16} \frac{a}{h} + \frac{1}{8} \left(\frac{a}{h} \right)^3 - \frac{45}{256} \left(\frac{a}{h} \right)^4 - \frac{1}{16} \left(\frac{a}{h} \right)^5 \right\}, \quad (2.71)$$

where D_0 is the diffusion coefficient of the sphere in an unbounded fluid. This expression was verified experimentally for an isolated spherical particle near a wall [50]. This in-plane self-diffusivity holds only for dilute suspensions of particles. Once the density of the particles increases, the diffusion is expected to decrease similar to the unbounded case. However, the functional form of the decrease with increasing density is different from the unbounded case as a result of the wall presence [51]. The hydrodynamic interaction between colloidal particles can be calculated by the methods of images and was obtained for a pair of particles diffusing at a distance h above a wall [52, 53]:

$$D_{\parallel}(r \gg h) = \frac{3k_{\text{B}}Th^2}{2\pi\eta r^3}, \quad (2.72)$$

$$D_{\perp}(r \gg h) = \frac{3k_{\text{B}}Th^4}{4\pi\eta r^5}. \quad (2.73)$$

These coefficients describe the leading terms of the in-plane correlated diffusion between two colloidal particles. Note that the leading term in the hydrodynamic interaction decays as $\sim r^{-3}$, rather than r^{-1} , which is due to the unconserved momentum in the system.

In this thesis, we study monolayers of particles near a wall. The first paper in Chapter 3 presents a comprehensive investigation of the structure and dynamics of colloidal suspensions that are adjacent to a rigid surface.

2.3 Cytoskeleton networks

The cytoskeleton is a remarkable system of filaments located in every eukaryotic cell. This system pulls the chromosomes apart at cell division, and then splits the cell into two. It drives and guides the intracellular traffic of organelles, ferrying materials from one part of the cell to another. It supports the fragile plasma membrane and provides the mechanical linkages that let the cell bear stresses and strains without being ripped apart as the environment shifts and changes. It enables some cells, such as sperm, to swim, and others, such as fibroblasts and white blood cells, to

crawl across surfaces. It provides the machinery in the muscle cell for contraction and in the neuron to extend an axon and dendrite. It guides the growth of the plant cell wall and controls the amazing diversity of eukaryotic cell shapes. Unlike conventional, polymeric materials, the cytoskeleton can actively generate forces by means of active filament (de)polymerization and the action of motor proteins. As a result, cells can autonomously adapt their shape and mechanical behavior [54]. The varied functions of the cytoskeleton center on the behavior of three families of protein molecules, which assemble to form three main types of filaments. Each type of filament has distinct mechanical properties and dynamics, but certain fundamental principles are common to them all.

2.3.1 Cytoskeleton filaments

The three types of cytoskeletal filaments are *intermediate filaments*(*IF*), *microtubules* (*MT*), and *actin filaments*. *IF* are rope-like fibers with diameter of around 10 nm, made of intermediate filament proteins which constitute a large and heterogeneous family. *IF* provide mechanical strength and resistance to shear stress. *MT* are long, hollow cylinders made of the protein tubulin. With an outer diameter of 25 nm, they are much more rigid than actin filaments. *MT* determine the positions of membrane-enclosed organelles and direct intracellular transport. They are long and straight and typically have one end attached to a single microtubule-organizing center called centrosome, as shown in table 2.1. *Actin filaments* determine the shape of the cell's surface and are necessary for whole-cell locomotion. Although *actin filaments* are dispersed throughout the cell, they are most highly concentrated in the cortex, just beneath the plasma membrane. Also, *actin filaments* are the major component of muscle cells together with their motor protein, myosin. Table 2.1 compares the three types of filaments.

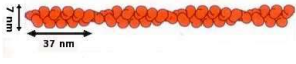
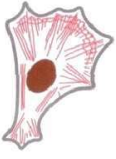
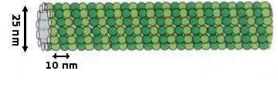

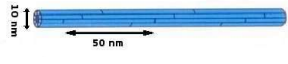

Filament type	Persistence length	Filament shape	Typical location in cell
Actin Filaments	$\sim 10 \mu\text{m}$		
Microtubules	$\sim 1000 \mu\text{m}$		
Intermediate Filaments	$\sim 1 \mu\text{m}$		

Table 2.1: Comparison between the cytoskeletal filaments (pictures adapted from [55])

2.3.2 Actin networks

Actin is the most abundant protein found in eukaryotic cells. It comprises 20% of the total protein mass in muscle cells and up to 5% in nonmuscle cells [56]. Globular actin (G-actin) polymerizes to form filamentous actin (F-actin) with a diameter, d , of $\sim 7 \text{ nm}$ and contour lengths, L , up to $50 \mu\text{m}$. An actin filament can be regarded as two parallel protofilaments that twist around each other into a right-handed helix. Actin filament growth and organization are regulated by many factors, including ionic concentrations and a variety of capping, binding, branching, and severing proteins.

The extensional modulus, or Young's Modulus, E , of F-actin is of order 10^9 Pa , similar to that of plexiglass [57]. However, because of the small filament diameter, the energy needed to bend F-actin is comparable to thermal energy, $k_B T$. This ratio defines a length, the persistence length $l_p = \kappa_0 / k_B T$, where $\kappa_0 \sim E d^4$ is the bending stiffness. This length is the distance over which vectors tangent to the filament contour become uncorrelated by the effect of thermally driven bending fluctuations.

For F-actin, $l_p \approx 8 - 17 \mu m$ [58, 59] and thus, it is semiflexible at micron length scales with a persistence length intermediate to that of DNA, $l_p \approx 0.05 \mu m$ [60], and microtubules, $l_p \approx 1000 \mu m$ [58]. F-actin appears to be the primary mechanical component of the cytoskeleton, as it provides mechanical support to the cells. In addition, the actin network is connected to trans-membrane adhesion proteins, thus facilitating the transduction of intracellular and extracellular mechanical signals, which allow cells to detect and respond to both chemical and mechanical signals from their extra-cellular environment [61].

In this thesis we study the properties of *in-vitro* reconstituted actin networks using microrheology methodology. The structural, dynamical and mechanical properties of *in-vitro* actin networks are highly interesting from two point of views. One is as a model system to understand basic physical mechanisms in polymeric networks. The second is as a simplified, controlled version of the cytoskeleton network, used to understand basic concepts and mechanisms in cellular mechanics.

2.3.3 Actin as a model system for semi-flexible polymers

The motivation for investigating the viscoelastic properties of F-actin networks, from a physicist's point of view, stems from the fact that they provide versatile model systems to study fundamental properties of polymeric fluids and gels. One major difference to synthetic polymers is the enormous contour and persistence lengths of these filaments. Thus actin filaments are a very good realization of semiflexible polymers whose material and statistical properties are very different from Gaussian chains.

The semi-flexible nature of individual actin filaments affects the mechanical properties and structure of F-actin networks profoundly. Due to their small aspect ratio, d/l_p , filaments become sterically entangled at very small volume fractions, $\phi \sim (d/l_p)^2 \sim 10^{-6}$. These networks are characterized by an average mesh size, $\xi_s = 0.3/\sqrt{c_A}$, where c_A is the actin concentration in mg/mL and ξ_s is measured in microns [62], which typically gets values of $0.1 - 2 \mu m$. The mesh size, also known as

the static correlation length of the network, depends only on monomer concentration and does not depend on the filament length l (as long as a network is formed, i.e., $l \gg \xi_s$). The dynamic correlation length, ξ_d , is the characteristic length over which dynamic correlations in the medium decay, and according to the prevailing view (by de Gennes) is equivalent to the static mesh size of the network [63, 64]. In this thesis we investigate the effect of filament length on the relation between the dynamic correlation length and the mesh size. The results of this study is described in the third article of Chapter 3, which reveals that, in contrary to the prevailing assumption, the relation between these correlation lengths is more complicated and may depend also on the filament length.

Similar to flexible polymer solutions, the mechanical properties of entangled semi-flexible polymer solutions are entropic in origin, due to the reduced number of filament conformations as a result of topological constraints. However, the mechanical properties of these solutions are qualitatively different from entangled solutions of flexible polymers. For instance, thermally induced bending fluctuations of single filaments, that lead to a high frequency mechanical response, are proportional to $\omega^{3/4}$ [65] (in contrast to flexible polymers, where high frequency behavior is characterized by power-laws in the range of $\omega^{1/2}$ to $\omega^{2/3}$ [66]). At lower frequencies, the steric constraints of the surrounding filaments prohibit large amplitude bending fluctuations and effectively constrain the filament dynamics to a tube. The elastic plateau modulus is determined by the volume of these allowed bending fluctuations [67]. Filaments can relax only by translational diffusion in the tube, or reptation, which can be on the order of hours in *in vitro* F-actin samples. Since the single filament reptation time determines the time scale over which the polymer solution flows, the storage modulus G' of entangled F-actin extends to very low frequencies, ~ 0.001 Hz.

An example for the viscoelastic moduli measured for F-actin is shown in Fig. 2.3, with two characteristic regimes [68]: viscous dominance at high frequencies, with moduli evolving with $\omega^{3/4}$; and elastic dominance at low frequency, with a plateau in the storage modulus.

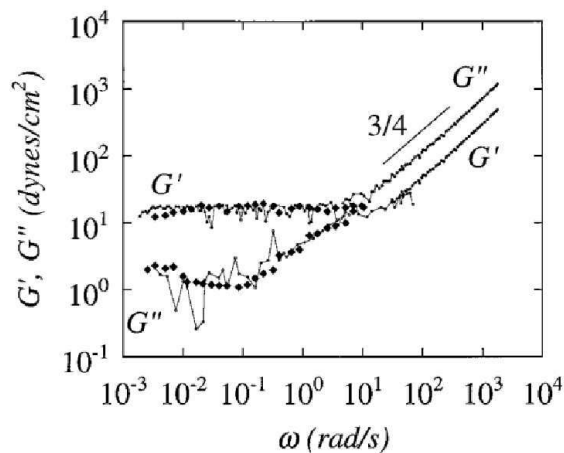


Figure 2.3: Elastic and loss moduli as measured by diffusing wave spectroscopy of a $24 \mu\text{M}$ (1 mg/mL) F-actin network. At low frequencies, F-actin networks are weak and solid-like. At high frequencies, F-actin networks are liquid-like; the loss modulus dominates the elastic modulus. The filled symbols represent elastic and loss moduli measured by mechanical rheometry. Figure adapted from Ref. [68].

Theoretical description by the two-fluid model

One theoretical model that describes the viscoelastic properties of actin networks is the two-fluid model. In this model the F-actin solution is modeled as a viscoelastic medium consisting of a viscoelastic network, characterized by a displacement variable, that is viscously coupled via a friction coefficient to an incompressible, Newtonian fluid, characterized by a velocity field. The main advantage of this model is that it is sufficiently simple to be treated analytically while delivering the key features of a complex fluid – emergent correlation length ξ and bulk viscoelastic modulus $G_b^*(\omega)$. Its main disadvantage is that it is a continuous, linear, hydrodynamic model, neglecting effects of thermal fluctuations, small-scale heterogeneities, and nonlinear advection. This model was used to validate the accuracy of the GSER in polymer networks, in particular, and complex fluid in general [9, 23]. In this thesis, we study the mechanical properties of actin networks. The experimental observations were

supported by a theoretical description of the network using the two-fluid model, which predicts the response of a generic viscoelastic network to mechanical perturbations. The resulting viscoelastic response and scaling laws were used to verify the appearance of the new intermediate regime of mechanical response, and to develop our new extension of microrheology analysis.

2.3.4 Actin as a model system for cell mechanics

Cells are complex systems composed of many different functional components. Cellular complexity is simultaneously the source of many interesting physical puzzles as well as an obstacle to understanding them. To overcome the barrier of complexity and yet to form a more complete understanding of cells, minimal model systems mimicking specific cellular components have been devised. These pave the way for an integrated thorough study of cells. Many biophysicists have focused on the structure and dynamics of the actin cytoskeleton using such bottom-up approaches [17,69–72]. The minimal model principle provides tools to study the single molecule interactions of cytoskeletal filaments and associated binding motors [73], but also tools to understand how collections of motor molecules interacting with actin filaments can lead to meso-scale active network behavior. Studies of bulk actin networks have been largely used as minimal model systems. Originally, such systems have been used mostly as a basis to understand the underlying mechanical properties of actin networks (as discussed in the previous section) [70,71,74], and more recently several studies moved on to the out-of-equilibrium behavior of actin networks containing active myosin motors [34,75–79].

The mechanical properties of actin networks confer to cells the ability to swiftly adapt their shape to perform different functions. Many researchers have focused efforts on understanding what underlying factors tune actin structure and mechanics. Such works includes a vast number of experiments on how crosslinkers of actin lead to network strain stiffening at high strains [74,80] or how they tune structure [81]. These studies were based on assays using bulk actin networks, whose composition and structure was modulated by the controlled addition of crosslinkers. Comple-

mentary to this, research on active actin-myosin gels has focused on understanding how the myosin II motor remodels the network structure and mechanical properties by generating internal stresses [82–86] and identifying the underlying dynamics of these out-of-equilibrium materials [34, 76–79].

Molecular motors and myosin II motors

Biological motors are responsible for various cellular tasks, such as transport of cargo along filamentous tracks or structural modification of the cytoskeleton for cellular motion. Each filament family has its own family of associated molecular motors. Kinesin and dynein belong to a motor families that walk along *MT*, while myosin motors are associated with actin filaments. Myosin has been the most studied of the motor proteins owing to its presence in striated muscle. The most commonly studied class of myosin is myosin II, which is found in both sarcomeric and smooth muscle, as well as in the cytoplasm. Myosin II can be split into two sections: heavy meromyosin (HMM), which has the motor domains and can hydrolyse ATP, and light meromyosin (LMM), which has a coil-coil structure and tends to form filamentous aggregates (known as mini-filaments). The thick filament in skeletal muscle is formed from huge filamentous aggregates of hundreds of myosin II, while myosin II in the cytoplasm forms mini-filaments with a small number of myosins. Myosins are in general non-processive, i.e. they detach after only a few ATPase cycles (or steps). The size of the aggregate, and hence its processivity can be tuned by control over the monovalent K^+ concentration [83], which enable detail investigation of the effect of increasing activity on the actin network's structure, dynamics and mechanics.

In this thesis we study *in-vitro* active actin-myosin networks, where we were interested in characterizing the effect of increasing activity on the networks properties. By precise control of network parameters we were able to tune the activity of networks, in the form of gradual increase in size and concentration of myosin mini-filaments, and to characterize their properties. This study is described in Chapter 4.

Chapter 3

Articles

This chapter describes our results for two out of the three experimental systems that we have investigated. In the following I will shortly review our results and present the published articles.

3.1 Structure and dynamics of sedimented colloidal suspensions

The structure and dynamics of quasi-2D suspensions of silica colloids above a single wall were investigated by a combination of experiment, simulation and theory. We performed detailed investigation of the structure and dynamics of the suspension as its density increases, by looking at the particles' motion in 3D. We discovered that as the density is increased a rather sharp formation of a second layer occurs. Surprisingly, this transition between one-layer to two-layer structure occurs at a relatively low area fraction ~ 0.3 , much lower than the packing fraction of such a 2D suspension. By looking at the dynamics of the suspension, we revealed that although the diffusion properties in each layer decreases monotonously (as expected for a dense suspension), the overall diffusion coefficient of the suspension follows a different behavior of flattening at high densities. The reason is that the second

layer, which has higher diffusivity, becomes more dominant and occupied. Thus, the prior knowledge of the two-layer structure is important to correctly interpret the overall diffusivity and, consequently, the viscosity of the suspension. In this study I conducted all the experiments and their analysis, and collaborated with other scientists from Poland and the United States who performed the simulations and theory respectively. More information on this study can be found in the first article of Sec. 3.3.

3.2 Viscoelastic response of F-actin networks at intermediate distances

We have performed detailed investigations on the microrheology of entangled F-actin networks. A careful, high precision analysis of the 2P microrheology experiments led to the discovery of a new regime of mechanical response at intermediate distances in actin networks. This is despite the fact that the microrheology of actin networks had been extensively investigated earlier. The intermediate response, arising from the effect of mass displacement rather than momentum diffusion, is enhanced by the much softer local microenvironment of the tracers compared to the bulk properties of the actin network. Consequently, the cross-over to the bulk behavior is pushed to surprisingly large distances, much larger than the mesh size, ξ , of the actin network. Since the intermediate response is related to mass conservation in the fluid, it is inherent to any two-component complex fluid, and is related to the correlation length of the material. Based on the theoretical description of this regime, we developed a new analysis scheme for microrheology experiments. Using a combination of 1P and 2P microrheology, we extracted from the intermediate and bulk responses the dynamic correlation lengths of actin networks as a function of several parameters, such as concentration and filament length. This work has established a new characterization tool for complex fluids. More information on the discovery of the new intermediate regime and its verification can be found in the second article of Sec. 3.3.

One application of our new analysis scheme is to study the relations between

the dynamic correlation length and the structure of the actin network (mesh size, ξ). This was done by introducing another new length scale, the average filament length, without altering the network's mesh size (static correlation length). Contrary to the prevailing view, according to de Gennes, that the dynamic correlation length is equivalent to the structural mesh size of the network, we found that the dynamic correlation length starts increasing as soon as the filament length enters the newly discovered intermediate regime (i.e., when it is still much larger than the mesh size). More information on this application can be found in the third article of Sec. 3.3.

3.3 Publications

In what follows the articles appear as published in the scientific press and according to the order at which they have been discussed above.

1. A. Sonn-Segev, J. Bławdziewicz, E. Wajnryb, M. L. Ekiel-Jeżewska, H. Diamant, Y. Roichman, Structure and dynamics of a layer of sedimented particles, *J. Chem. Phys.*, **143**, 074704 (2015).
2. A. Sonn-Segev, A. Bernheim-Groswasser, H. Diamant, Y. Roichman, Viscoelastic response of a complex fluid at intermediate distances, *Phys. Rev. Lett.*, **112**, 088301 (2014).
3. A. Sonn-Segev, A. Bernheim-Groswasser, Y. Roichman, Extracting the dynamic correlation length of actin networks from microrheology experiments, *Soft Matter*, **10**, 8324 (2014).

Structure and dynamics of a layer of sedimented particles

Adar Sonn-Segev,¹ Jerzy Bławdziewicz,² Eligiusz Wajnryb,³ Maria L. Ekiel-Jeżewska,³ Haim Diamant,¹ and Yael Roichman^{1,a)}

¹Raymond and Beverly Sackler School of Chemistry, Tel Aviv University, Tel Aviv 6997801, Israel

²Department of Mechanical Engineering, Texas Tech University, 7th and Boston, Lubbock, Texas 79409, USA

³Institute of Fundamental Technological Research, Polish Academy of Sciences, Pawińskiego 5B, Warsaw 02-106, Poland

(Received 12 April 2015; accepted 30 July 2015; published online 20 August 2015)

We investigate experimentally and theoretically thin layers of colloid particles held adjacent to a solid substrate by gravity. Epifluorescence, confocal, and holographic microscopy, combined with Monte Carlo and hydrodynamic simulations, are applied to infer the height distribution function of particles above the surface, and their diffusion coefficient parallel to it. As the particle area fraction is increased, the height distribution becomes bimodal, indicating the formation of a distinct second layer. In our theory, we treat the suspension as a series of weakly coupled quasi-two-dimensional layers in equilibrium with respect to particle exchange. We experimentally, numerically, and theoretically study the changing occupancies of the layers as the area fraction is increased. The decrease of the particle diffusion coefficient with concentration is found to be weakened by the layering. We demonstrate that particle polydispersity strongly affects the properties of the sedimented layer, because of particle size segregation due to gravity. © 2015 AIP Publishing LLC. [<http://dx.doi.org/10.1063/1.4928644>]

I. INTRODUCTION

Being relevant to a wide range of practical scenarios, the behavior of colloid suspensions near solid surfaces has been thoroughly studied over the years. This research effort consists of several bodies of work, for each of which we can give only a few representative references. The first category of papers concerns the disruption of the structural isotropy of a three-dimensional (3D) fluid suspension by the surface, e.g., the formation of a layered structure decaying away from the surface under equilibrium^{1,2} and nonequilibrium³ conditions. Another category addresses the effect of the anisotropic geometry on particle dynamics near a single planar surface—for isolated particles,^{4–11} particle pairs,^{4,12–14} and a 3D suspension adjacent to a surface.^{15–19}

Regarding quasi-two-dimensional (quasi-2D) layers of particles, most studies have considered the confinement of suspensions between two rigid surfaces. This research addressed structural properties of such confined suspensions,^{20–24} and the dynamics of single particles,^{25–27} particle pairs,^{28,29} and concentrated quasi-2D suspensions.^{30–32} Another type of quasi-2D suspensions has also been studied, where a particle layer is confined to a fluid interface.^{33–36}

In cases where the surface attracts the particles and the suspension is sufficiently dilute, the system can contain a single layer of surface-associated particles in contact with a practically particle-free solvent.² A single layer can also form as a result of gravitational settling of particles toward a horizontal wall. This scenario is studied in the present work.

Sedimented colloidal particles undergo random Brownian displacements, which results in diffusive broadening of the fluctuating particle layer. The width of the particle height

distribution above the bottom surface is characterized by the sedimentation length l , i.e., the height at which the gravitational energy of a particle equals its thermal energy. The dynamics and height distribution of individual sedimented particles above the bottom surface were studied in Refs. 7–9 using total internal reflection microscopy. Particle monolayers at higher densities were investigated experimentally for a system in which the sedimentation length is much smaller than the particle diameter.³⁷ It was shown that at high area fractions the suspension can assemble into quasi-2D colloidal crystals, but formation of a nonuniform vertical microstructure was not observed, because of the small sedimentation length.

Here, we are interested in the structure and dynamics of a surface-associated layer for which the sedimentation length is comparable to the particle diameter. We focus on the effects of the suspension concentration on the statistical height distribution of particles and their diffusion coefficient. Unlike the quasi-2D suspensions confined between two surfaces or adsorbed at a fluid interface (which restricts particle configurations and motions in two directions), in the present system no constraints are imposed on the distance between the particles and the single wall. Thus, at sufficiently high area fractions, particles form a nontrivial stratified microstructure. This microstructure and its effect on particle dynamics are analyzed in our paper.

The article is organized as follows. Section II describes the experimental methods used to prepare the system, image the particles, and analyze the extracted data. In Sec. III, we describe the theoretical background and numerical methods used to perform the simulations. In Sec. IV, we present the results concerning the equilibrium structure of the quasi-2D suspension observed in planes parallel to the bottom surface (the quasi-2D radial distribution) and in the direction perpendicular to it (the height distribution). Section V addresses the

^{a)}roichman@tau.ac.il

diffusion of particles parallel to the surface, as affected by the surface proximity. We discuss our findings in Sec. VI.

II. EXPERIMENTAL METHODS

A. Quasi-2D system of sedimented Brownian spheres

Quasi-2D colloidal layers are created by placing a suspension of colloidal silica spheres in a glass sample cell $\sim 150 \mu\text{m}$ high. The particles are then allowed to sediment and equilibrate for 30 min at a temperature of approximately 24°C before measurements start (Fig. 1). We use green fluorescent monodisperse, negatively charged silica particles (Kisker Biotech, PSI-G1.5 Lot #GK0090642T) with diameter $d = 1.50 \pm 0.15 \mu\text{m}$ and mass density $\rho_0 = 2.0 \text{ g/cm}^3$. Monolayers of area fraction $0 < \phi \leq 0.62$ are prepared by diluting the original suspension with double distilled water (DDW, 18 M Ω), without and with the addition of salt at a concentration $[\text{KCl}] = 0.01\text{M}$. The sample walls are cleaned and slightly charged by plasma etching to avoid particle attachment to the bottom wall of the cell. We observe that the aqueous medium above the colloidal monolayer is free of colloids. Since the particles are floating right above the bottom wall, we can treat the upper wall as a distant boundary.

B. Imaging techniques

Particle position and motion in the x - y plane, perpendicular to the optical axis, are observed using epifluorescence microscopy (Olympus IX71). Images are captured at a rate of 70 fps by a CMOS camera (Gazelle, Point Grey Research). We use in-line holographic microscopy to image the dynamics of particles in three dimensions in dilute

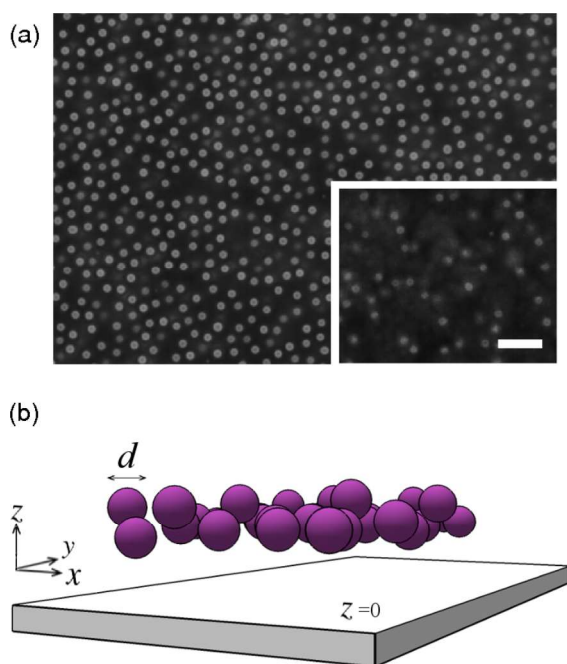


FIG. 1. (a) Images of fluorescent $1.5 \mu\text{m}$ -diameter silica spheres suspended in water, taken after the particles sedimented to create a quasi-2D suspension at area fraction $\phi = 0.49$. Large (small) image corresponds to a typical image of the first (second) layer. Scale bar = $5 \mu\text{m}$. (b) Schematic view of the system and its parameters.

samples.³⁸ This imaging technique uses a collimated coherent light source (DPSS, Coherent, $\lambda = 532 \text{ nm}$) to illuminate a sample mounted on a microscope. The light scattered from the sample interferes with the light passing through it, to form a hologram in the image plane. We reconstruct the light field passing through the sample by Rayleigh-Sommerfeld back-propagation and extract from it the particle location in three dimensions.^{38–40} For holographic imaging measurements we use non-fluorescent silica particles with the same diameter ($d = 1.50 \pm 0.08 \mu\text{m}$, Polysciences, Inc.). Additional details of the setup and measurement methods can be found elsewhere.³⁸

We use confocal imaging to monitor particle positions in a dense layer in three dimensions. Our spinning disc confocal imaging system (Andor, Revolution XD) includes a Yokogawa (CSU-X1) spinning disc, and an Andor (iXon 897) EM-CCD camera. An objective lens (Olympus, $\times 60$, NA = 1.1, water immersion) mounted on a piezoelectric scanner (Physik Instrumente, Pifoc P-721.LLQ) is used to scan the sample in the z axis, with a step size of 100 nm .

C. Height calibration

A suspended tracer particle is subject to electrostatic and gravitational forces in addition to thermal fluctuations, affecting its height distribution.⁸ The particle potential energy can be described as

$$U = mgz + Be^{-(z-d/2)/\lambda}, \quad (1)$$

where z is the vertical position of the tracer, g is the gravitational acceleration,

$$m = \frac{\pi}{6} \Delta \rho_0 d^3 \quad (2)$$

is the buoyant mass of the tracer ($\Delta \rho_0$ is the mass density difference between silica and water), λ is the Debye screening length, and the amplitude B depends on λ and the surface charges of both particle and glass surfaces. The corresponding probability distribution of the particle height z is

$$\rho(z) = Z^{-1} e^{-U(z)/k_B T}, \quad (3)$$

where $k_B T$ is the thermal energy and Z^{-1} is the normalization constant.

The height distribution of a single particle above the sample's bottom was obtained from very dilute suspensions, using in-line holographic imaging^{38–40} (see Fig. 2). Our holographic measurements provide values of relative particle positions, but not the absolute particle heights with respect to the bottom wall. We thus set the peak position to $z = 0$ and focus on the height relative to this reference plane. The exponential decay on the right side of the probability-density peak is governed by a decay length,

$$l = \frac{k_B T}{mg} \quad (4)$$

(the sedimentation length), resulting from the competition between gravity and thermal forces. The exponential-decay length determined from the holographic measurements agrees well with calculated sedimentation length (4), without any fitting parameters, $l/d \cong 0.16$ (see Fig. 2). The electrostatic term of the probability-density, which controls the steep rise

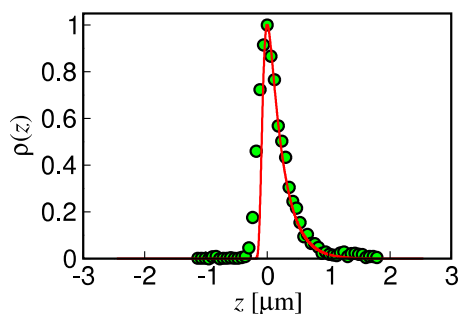


FIG. 2. Holographic imaging. Height probability distribution of a single sphere (in salt-free water) shifted to the maximum value and fitted to Boltzmann probability distribution (3) with particle-wall potential (1).

of the probability, affects mostly the peak position rather than its shape. Since we shifted the peak position to $z = 0$, the fitting of the entire probability-density using Eqs. (1) and (3) was insensitive to the value of B . Reasonable fits were obtained for λ in the range of $\lambda \sim 40\text{--}70$ nm. These low values of λ are commonly found, and are due to elevated ion concentration in the solution. These in turn may be caused by ion leakage from the sample glass walls and from contact with air.⁴¹ Better estimations of B and λ are given in Sec. IV A 1, using mobility measurements.

The applicability of the holographic imaging is limited to low-density suspensions, whereas the confocal imaging can be also used at higher concentrations. On the other hand, confocal

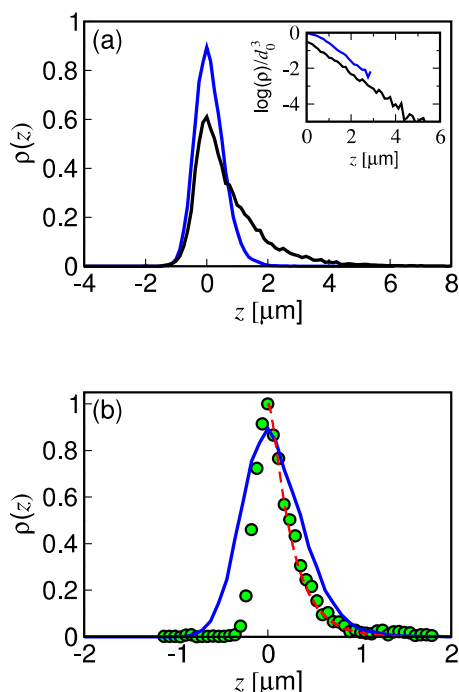


FIG. 3. (a) Confocal imaging. Height probability distribution of silica particles at $\phi < 0.003$ with diameters of $d_0 = 1.5$ μm (blue) and $d_0 = 1.0$ μm (black). Inset: logarithm of the probability distributions scaled by d_0^3 in units of 10^2 μm^{-3} ; as expected, the two curves have approximately the same slope, which is used to calibrate the confocal height measurements. (b) Height probability distribution of silica particles with diameter $d_0 = 1.5$ μm extracted from holographic imaging (green circles, see Fig. 2) and confocal imaging (blue line). The red dashed line corresponds to the expected barometric exponential decay. The suspensions in both figures were with no added salt, $[\text{KCl}] = 0\text{M}$.

height measurements suffer from spherical aberrations due to multiple changes in refractive index in the imaging path. This leads to a systematic error in measuring z , which can be eliminated by proper calibration. We calibrate the confocal measurement of the relative vertical particle positions by requiring the exponential decay of the height distribution to agree with the known, and verified, value of l .

In Fig. 3(a), we show the particle-height distribution $\rho(z)$ at $\phi < 0.003$ for two different particle sizes ($d_0 = 1.0, 1.5$ μm). The distributions are shifted so that the highest probability is located at $z = 0$. Scaling the logarithm of the distributions by d_0^3 [inset of Fig. 3(a)] shows that the normalized decay constants for the two particle sizes have approximately the same value, from which we calibrate the confocal microscope's height measurements. In Fig. 3(b), the height distributions extracted by the two methods (holographic and confocal imaging) are overlaid. This figure emphasizes the higher accuracy of holographic imaging over confocal imaging, especially around $z = 0$, where the increase in distribution should be very steep.^{8,38} The difference between the curves can also be attributed to polydispersity, since the holographic imaging is a single-particle measurement while the confocal imaging is a multiple-particle measurement, and its corresponding curve represents an average over ~ 40 particles.

III. NUMERICAL METHODS

A. The system

1. Particles and their interactions

Silica particles are modeled as Brownian hard spheres with or without electrostatic repulsion (depending on the salt concentration), immersed in a fluid of viscosity η . The bottom wall is treated as an infinite hard planar surface. Creeping-flow conditions and no slip boundary conditions at the particle surfaces and at the wall are assumed.

In a salt solution with $[\text{KCl}] = 0.01\text{M}$, the Debye length is only about 5 nm, and therefore electrostatic interactions are screened out. The particles thus interact only via infinite hard-core particle-particle, and particle-wall potentials, and the gravity potential mgz , and no other potential forces are involved. The strength of the gravity force is described by sedimentation length (4).

In addition to the hard-core repulsion, in DDW with no added salt ($[\text{KCl}] = 0\text{M}$) particles are assumed to also interact via particle-wall and particle-particle Debye-Hückel potentials,

$$V(z) = B e^{-(z-d/2)/\lambda} \quad (5)$$

and

$$V'(r) = B' e^{-(r-d)/\lambda}, \quad (6)$$

where λ is the Debye screening length, B and B' are the potential amplitudes, and r is the distance between the particle centers. The consideration of Debye-Hückel potentials in the salt-free case is based on our experimental measurement $\lambda \sim 60$ nm. A finite Debye screening length in DDW stems from the presence of residual ions in the solution.⁴²

2. Suspension polydispersity

To determine the effects of the suspension polydispersity on the near-wall microstructure and dynamics, we have performed numerical simulations for a hard-sphere (HS) system with a Gaussian distribution of particle diameters,

$$p(d) = \frac{1}{(2\pi\sigma^2)^{1/2}} \exp\left[-\frac{(d-d_0)^2}{2\sigma^2}\right], \quad (7)$$

where d and d_0 are the actual and average particle diameters, and σ is the standard deviation. All the particles have the same mass density ρ_0 ; hence, particles of different sizes have different buoyant masses and different sedimentation lengths (4). The dimensionless sedimentation length based on the average particle diameter d_0 is defined as

$$\frac{l_0}{d_0} = \frac{k_B T}{m_0 g d_0}, \quad (8)$$

where

$$m_0 = \frac{\pi}{6} d_0^3 \Delta \rho_0. \quad (9)$$

The area fraction ϕ based on the average particle diameter d_0 is

$$\phi = \frac{1}{4} \pi n d_0^2, \quad (10)$$

where n is the number of particles per unit area. Since the particles are free to move in the z direction, the area fraction ϕ can exceed 1.

3. System parameters

The simulations were carried out for the following system parameters: For dimensionless sedimentation length (8), we use the value

$$\frac{l_0}{d_0} = 0.158, \quad (11)$$

calculated from the particle size and density. Based on the comparison between the calculated and measured values of the equilibrium average of the lateral self-diffusion coefficient for isolated particles in DDW, we estimate that the Debye length and the amplitude of particle–wall electrostatic repulsion are

$$\lambda/d = 0.03, \quad \frac{B}{k_B T} = 10. \quad (12)$$

These values are used for salt-free suspensions at all suspension concentrations. Assuming that the charge densities of the particle and wall surfaces are similar, we take

$$B' = B/2 \quad (13)$$

for the interparticle-potential amplitude, as follows from the Derjaguin approximation.⁴³

The simulations were performed in the range of area fractions $\phi \leq 1.2$. For polydisperse HS systems, the calculations were carried out for $\sigma/d_0 = 0.10, 0.15, 0.20$, and 0.25 (we estimate that $0.10 < \sigma/d_0 < 0.15$ for the silica particles used in the experiments). For particles interacting via Debye–Hückel potentials (5) and (6), only monodisperse suspensions were considered.

B. Evaluation of the equilibrium distribution

1. Low density limit

For monodisperse suspensions at low particle concentrations, the equilibrium particle distribution $\rho(z)$ is given by normalized Boltzmann factor (3). To determine the particle distribution for a dilute polydisperse suspension, the particle-size-dependent Boltzmann factor for individual particles, $\rho_1(z; d)$, is convoluted with particle-size distribution (7),

$$\rho(z) = \int_0^z dd p(d) \rho_1(z; d). \quad (14)$$

For a HS system,

$$\rho_1(z; d) = l^{-1} e^{-(z-d/2)/l} \theta(z-d/2), \quad (15)$$

according to Equations (1)–(4), where $\theta(x)$ is the Heaviside step function, and the sedimentation length l is particle-size dependent due to the variation of particle mass.

2. Monte Carlo (MC) simulations

To determine the equilibrium microstructure of a sedimented suspension at finite particle area fractions, equilibrium MC simulations were performed for 2D-periodic arrays of spherical particles in 3D space (with periodicity in the horizontal directions x and y and the box size L). The particles interact via infinite hard-core repulsion and the pair-additive potential,

$$U(\mathbf{X}) = \sum_{i=1}^N m_i g z_i + \sum_{i=1}^N V(z_i) + \frac{1}{2} \sum_{i=1}^N \sum_{j \neq i}^N V'(r_{ij}), \quad (16)$$

which includes the gravity term and particle–wall and particle–particle screened electrostatic potentials (5) and (6). Here, $\mathbf{X} = (\mathbf{r}_1, \dots, \mathbf{r}_N)$ is the particle configuration (with \mathbf{r}_i denoting the position of particle i), z_i is the vertical coordinate of particle i , and $r_{ij} = |\mathbf{r}_i - \mathbf{r}_j|$ is the relative particle distance.

A purely HS system with $V = V' = 0$ was modeled for monodisperse particles and for polydisperse particles with Gaussian size distribution (7). For systems with nonzero electrostatic repulsion, only monodisperse particles were considered.

The initial configuration was prepared by placing $N = 400$ particles randomly in a vertical cuboid box with the square base L and the height $10L$. The size L of the 2D-periodic cell was determined to obtain the required area fraction ϕ of the sedimented particle layer. The suspension was allowed to sediment by following the MC random-walk dynamics in the configurational space \mathbf{X}^{44} (as described below). After the equilibrium state was reached, suspension properties were obtained by averaging the quantities of interest over at least 200 independent configurations.

Our adaptive simulation procedure was performed by repeating the MC steps defined as follows.

- (a) A randomly selected particle i is given a small random displacement, $\mathbf{r}_i \rightarrow \mathbf{r}'_i = \mathbf{r}_i + \Delta$, where Δ is chosen from a 3D Gaussian distribution with the standard deviation adaptively adjusted to the current mean gap between particles.

This displacement results in the change of the configuration from X to X' .

- (b) According to the Metropolis detailed balance condition, the new configuration is accepted with the probability

$$\min(1, \exp\{-[U(X') - U(X)]/k_B T\}), \quad (17)$$

provided that there is no particle–particle or particle–wall overlap.

To let the system reach an equilibrium state X_1 , the MC steps (a) and (b) are repeated $10^5 N$ times. The next independent equilibrium configuration X_{n+1} is obtained from the previous configuration X_n by performing $10^4 N$ MC steps. The particle height distribution $\rho(z)$ and other equilibrium quantities are obtained by averaging over 200 independent configurations X_i .

C. Hydrodynamics and self-diffusion

1. Low density limit

In the absence of a wall, the self-diffusion coefficient of an isolated solid sphere with diameter d_0 is given by the Stokes–Einstein expression

$$D_0 = \frac{k_B T}{3\pi\eta d_0}. \quad (18)$$

The self-diffusion coefficient $D(z)$ of a sphere with diameter d at a distance z from the wall differs by a factor

$$\frac{D(z)}{D_0} = \frac{d_0}{d} \mu_{\parallel}(z/d), \quad (19)$$

where the normalized mobility coefficient μ_{\parallel} depends on the dimensionless particle position z/d and no other parameters. Relation (19) refers to the lateral component of the self-diffusion coefficient (parallel to the wall), which was measured in our experiments. However, an analogous expression also holds for the normal component.

For monodisperse particles in the dilute-suspension limit, the effective self-diffusion coefficient D_s averaged across the suspension layer is obtained by integrating (19) with Boltzmann distribution (3),

$$\frac{D_s}{D_0} = \int_{d/2}^{\infty} dz \rho(z) \mu_{\parallel}(z/d). \quad (20)$$

For a polydisperse suspension, an additional average over particle-size distribution (7) is needed,

$$\frac{D_s}{D_0} = \int_0^{\infty} dd p(d) \int_{d/2}^{\infty} dz \rho_1(z; d) \mu_{\parallel}(z/d). \quad (21)$$

The mobility coefficient $\mu_{\parallel}(z/d)$ was evaluated with high accuracy using the HYDROMULTIPOLE algorithm for a particle near a single wall.⁶ The integrals in Eqs. (20) and (21) were performed numerically using the Gauss method, with $\mu_{\parallel}(z/d)$ calculated by a series expansion.

2. Computations for larger densities

The effective self-diffusion coefficient for suspensions at higher concentrations was evaluated using a periodic version⁴⁵

of the Cartesian-representation algorithm for a system of particles in a parallel-wall channel.^{29,46} In our approach, periodic boundary conditions in the lateral directions are incorporated by splitting the flow reflected by the particles into a short-range near-field contribution and a long-range asymptotic Hele–Shaw component. The near-field contribution is summed explicitly over neighboring periodic cells, and the Hele–Shaw component is evaluated using Ewald summation method for a 2D harmonic potential.^{45,47}

The one-wall results were derived from the two-wall calculations using an asymptotic procedure based on the observation that in the particle-free part of the channel the velocity field tends to a combination of a plug flow and a shear flow. All other flow components decay exponentially with the distance from the particle layer. The one-wall results are obtained by eliminating the shear flow and retaining only the plug flow generated by hydrodynamic forces induced on the particles.⁴⁸ The calculations were performed for the distance to the upper virtual wall $H = 10d_0$, which is sufficient to obtain highly accurate one-wall results.

The self-diffusion coefficient is determined by averaging the trace of the lateral translational–translational N -particle mobility, evaluated using HYDROMULTIPOLE codes based on the above algorithm, with the multipole truncation order $L = 2$.⁴⁹ By comparing results for different values of L , we have verified that truncation at $L = 2$ yields accuracy better than 0.5% for the quantities considered in our study. The averaging was performed over equilibrium configurations of $N = 400$ particles in a 2D-periodically replicated simulation cell. Independent equilibrium configurations were constructed using the MC technique described in Sec. III B 2.

IV. STRUCTURE OF THE QUASI-2D SUSPENSIONS

A. Experimental results

A typical image of our quasi-2D colloidal suspension is shown in Fig. 1. For each area fraction ϕ and salt concentration, the suspension can be characterized by the structure in the x – y plane (parallel to the cell floor) and the density profile in the z direction (perpendicular to the floor). In this section, we discuss results of our measurements of the microstructure of a sedimented particle layer.

1. Mean particle height at low area fractions

As mentioned in Sec. II C, our imaging techniques do not yield absolute particle heights. To estimate the mean particle distance z from the bottom wall (the mean height) in a dilute suspension layer, we observe particle dynamics in the horizontal directions, and compare measurement results with theoretical calculations of the effect of the wall on the lateral particle diffusion. Using fluorescence imaging, we determine the projection of particle trajectories onto the x – y plane, $\mathbf{r}_{\parallel}(t)$, and extract the effective self-diffusion coefficient,

$$D_s = \langle \Delta \mathbf{r}_{\parallel}^2(\tau) \rangle / (4\tau), \quad (22)$$

where τ is the time interval. The position-dependent diffusivity $D(z)$ in the x – y plane of a single particle near a planar

wall is given by the following expansion in the particle–wall distance:^{4,5}

$$\frac{D(z)}{D_0} = 1 - \frac{9}{32} \frac{d}{z} + \frac{1}{64} \left(\frac{d}{z}\right)^3 - \frac{45}{4096} \left(\frac{d}{z}\right)^4 - \frac{1}{512} \left(\frac{d}{z}\right)^5, \quad (23)$$

where $z = 0$ is the wall position. Expansion (23) is accurate within 5% to 1% as z increases from $0.51d$ up to $d/2 + 2l$, in the range where sedimented particles spend most of the time in a low-density suspension under equilibrium conditions. Here, $l \approx 0.16d$ is sedimentation length (4).

From expression (23) and D_s extracted according to (22), we can calculate the suspension's mean distance from the wall (where z in (23) is replaced by a mean value $\langle z \rangle$). This calculation holds in the limit $\phi \rightarrow 0$, where there are no particle-particle interactions. We measure D_s from the particle trajectories, $\mathbf{r}_{\parallel}(t)$, in extremely low area fraction solution, $\phi < 0.003$ (in salt-free water), and obtain a mean distance from the wall $\langle z \rangle = 1.1 \pm 0.1 \mu\text{m}$, corresponding to a mean gap $\epsilon = z - d/2$ of $0.3\text{--}0.4 \mu\text{m}$ between the particle surface and the wall. We also extract $\langle z \rangle$ for different salt concentrations by extrapolating D_s (measured at various area fractions) to $\phi = 0$ (see Sec. V A), obtaining $\langle z \rangle = 0.95 \pm 0.05 \mu\text{m}$ for $[\text{KCl}] = 0.01\text{M}$ and $\langle z \rangle = 1.11 \pm 0.05 \mu\text{m}$ for $[\text{KCl}] = 0\text{M}$. The latter matches the average height extracted from the diffusion of tracers in the extremely low density suspension.

For $\lambda = 5 \text{ nm}$ (added salt), the mean height calculated from Boltzmann distribution (3) is dominated by the exponential decay due to gravity and is practically independent of B in particle–wall potential (1). For $B = 0$, using the particle mass as determined from Eq. (2) with no fitting parameters, we get $\langle z \rangle = 0.99 \mu\text{m}$, in agreement with the diffusivity-based measurements of $\langle z \rangle$. This result confirms that in the added-salt case we can neglect the electrostatic repulsion from the wall. For the salt-free case, taking $\lambda = 50 \text{ nm}$, we obtain $\langle z \rangle = 1.11 \mu\text{m}$ for B in the range $5\text{--}15 k_B T$. These values are consistent with those obtained by fitting the measured height distribution to theoretical expression (1) (see Sec. II C).

Since Eq. (23) does not include lubrication correction for small particle–wall gaps ϵ , it overpredicts $D(z)$ for $z < 0.51d$; however, the accuracy of the approximation is sufficient for the purpose of the present estimates. In our calculations discussed in Secs. III and V B, highly accurate HYDROMULTIPOLE results were used instead of far-field approximation (23).

2. Radial distribution in the horizontal plane

To verify that no crystalline or hexatic structures are formed at higher values of the area fraction, we evaluate from the experiment the radial distribution function $g(r)$ and the full 2D pair distribution $g(r, \theta)$ in the x – y plane, for both the salt-free and salt-added suspensions. No dependence on θ was found. The radial distribution $g(r)$ for several values of the area fraction ϕ is shown in Fig. 4(a) for the salt-free system and in Fig. 4(b) for the salt-added system. We observe a fast decay of $g(r)$ in all our experiments and no splitting of the second peak, confirming that the colloidal suspension is in the liquid phase.

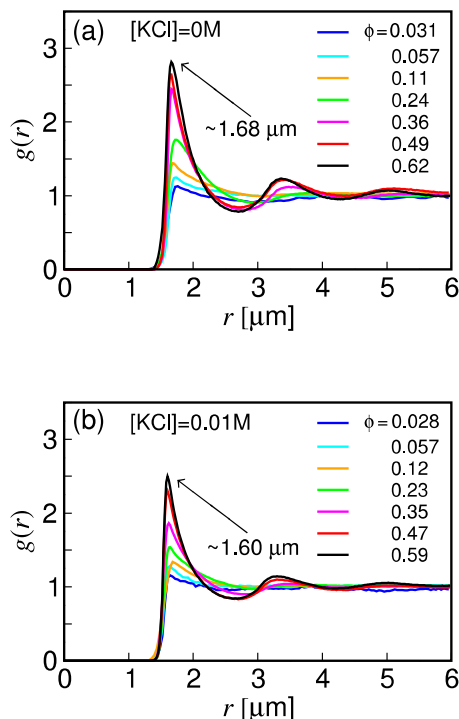


FIG. 4. Radial distribution function $g(r)$ in the x – y plane for experiments in (a) salt-free and (b) salt-added ($[\text{KCl}] = 0.01\text{M}$) water. The distribution $g(r)$ was calculated separately in the first and second layers (see Sec. IV A 4 for the layer definition) and combined with appropriate weights.

For monodisperse hard spheres, the first peak of $g(r)$ should correspond to the diameter of the sphere. Our measurements show that the first peak is at $r = 1.68 \mu\text{m}$ for suspensions without salt and at $r = 1.60 \mu\text{m}$ for suspensions with $[\text{KCl}] = 0.01\text{M}$. The difference between these two numbers implies that the effective shell around the particles in the salt-free samples is around $40\text{--}50 \text{ nm}$, which provides an estimation for the screening length in DDW without the addition of salt. This estimate of λ is consistent with the other two mentioned above.

3. Vertical density profile

The height distributions $\rho(z)$ of the silica particles at different area fractions of the sedimented particle layer were acquired using confocal imaging and conventional image analysis.⁵⁰ These distributions for salt-added suspensions with $[\text{KCl}] = 0.01\text{M}$ are plotted in Fig. 5(a) for several values of the area-fraction ϕ . Since we cannot precisely measure the position of the wall, the distributions are shifted so that their first peak (close to the wall) is located at $z = 0$. These distributions indicate the formation of a second layer of particles for area fractions $\phi \gtrsim 0.26$. The observed center of the second layer is located $\Delta z \approx 0.75 \mu\text{m}$ above the center of the first layer. The layer separation is thus significantly smaller than the expected separation $\Delta z \approx d = 1.5 \mu\text{m}$ (which is similar to the peak separation for the radial distribution). See further discussion in Sec. VI and the Appendix.

To highlight the onset of the formation of the second layer, we look at the subtraction of the height probability distribution at the lowest area fraction from the distribution at all area

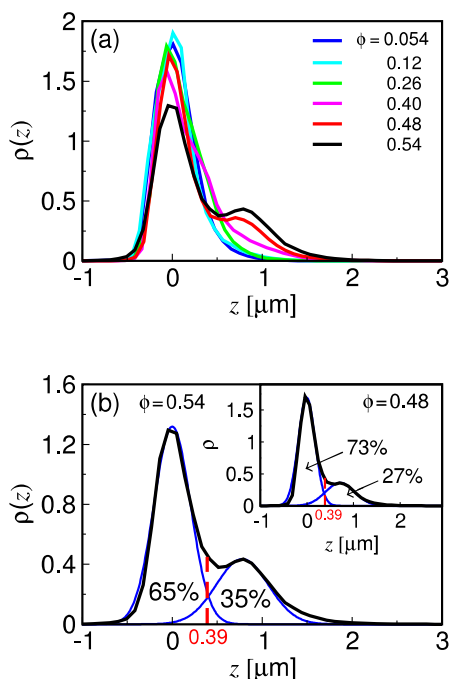


FIG. 5. (a) Height probability distribution of the silica colloids (in $[\text{KCl}] = 0.01\text{M}$) for increasing area fraction reveals the formation of a second layer. Colors correspond to different area fractions (as labeled). (b) For the most dense suspensions [$\phi = 0.54$ and $\phi = 0.48$ (inset)], the height distribution (black solid line) around the two peaks can be fitted to two Gaussian functions (blue lines). The intersection of the two Gaussians defines an effective boundary (red broken line) between the first and second layers; occupation percentages are indicated.

fractions, $\Delta\rho \equiv \rho - \rho_{\phi=0.054}$ [Fig. 6(a)]. Two phenomena are expected when a second layer is formed: (i) negative values at $z = 0 \mu\text{m}$, corresponding to a reduction in the fraction of particles populating the first layer, (ii) positive and increasing

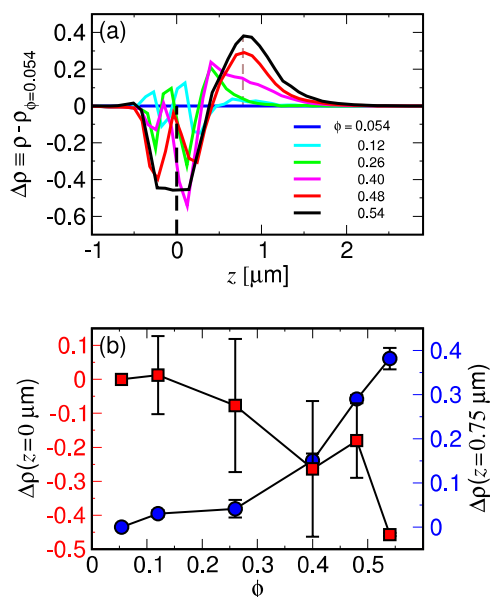


FIG. 6. (a) The difference between the height probability distribution at increasing area fractions and the distribution at the lowest area fraction $\phi = 0.054$, $\Delta\rho \equiv \rho - \rho_{\phi=0.054}$ (in $[\text{KCl}] = 0.01\text{M}$). Colors are as in Fig. 5(a). Gray (black) dashed line corresponds to $z = 0.75 \mu\text{m}$ ($z = 0 \mu\text{m}$). (b) Values of $\Delta\rho$ at $z = 0 \mu\text{m}$ (red squares) and $z = 0.75 \mu\text{m}$ (blue circles) for all area fractions. Both plots exhibit a change in trend at area fraction $\phi \sim 0.3$.

values at $z = 0.75 \mu\text{m}$, corresponding to the formation and increasing population of the second layer. The values of $\Delta\rho$ at $z = 0$ and $0.75 \mu\text{m}$ are plotted in Fig. 6(b). The two expected phenomena are observed at approximately $\phi \sim 0.3$, indicating the area fraction above which a second layer becomes occupied. At area fractions smaller than 0.3, we still obtain negative values of $\Delta\rho$ at $z = 0 \mu\text{m}$, and positive values at $z = 0.75 \mu\text{m}$; however, these values are relatively low and can correspond to the broadening of the exponential distribution due to increase in ϕ .

4. Particle-layer occupation fractions

For the area fractions at which a clear second peak in the particle distribution ρ is seen in Fig. 5(a) (i.e., for $\phi = 0.48$ and 0.54), we fit the area around each peak to a Gaussian function and define the point of intersection between the two Gaussians as the effective boundary between the two layers. Figure 5(b) shows the two distributions with the Gaussian fits and our definition of that boundary, which turns out to be at a distance of $0.39 \pm 0.04 \mu\text{m}$ above the peak of the first layer in both densities.

Using this boundary, we evaluated the occupation fractions $f_i = \phi_i/\phi$ of the bottom ($i = 1$) and top layer ($i = 2$), where ϕ_i is the area fraction of particles in layer i . The results are shown in Fig. 7(a) for a suspension in $[\text{KCl}] = 0.01\text{M}$ solution as a function of the total area fraction ϕ . As expected, the fraction of particles populating the second layer grows as the total area fraction of the suspension is increased.

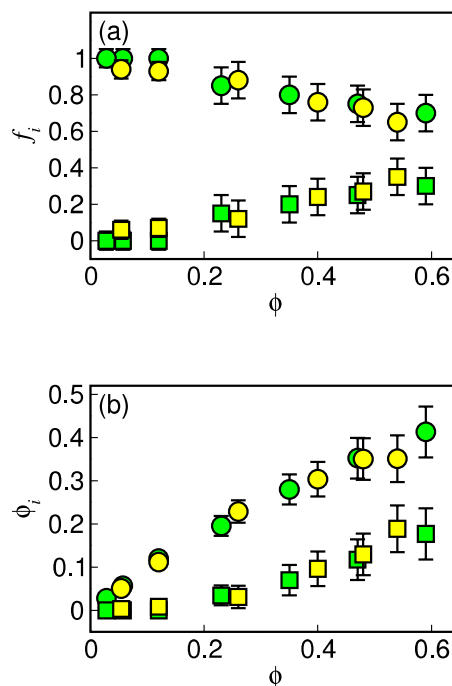


FIG. 7. Occupation fractions f_i and area fractions ϕ_i of suspension layers as a function of the total area fraction ϕ ; circles (squares) correspond to the first (second) layer. (a) Occupation fractions for experiments in $[\text{KCl}] = 0.01\text{M}$ extracted from the confocal height distribution curves (yellow) and from the 2D images (green), showing good agreement between the two methods. (b) The same data replotted for the area fractions ϕ_1 and ϕ_2 of the first and second layers.

An additional independent measurement of the layer occupation fractions is done using epifluorescence microscopy, which enables us to image the different layers separately [see Fig. 1(a)]. The occupation fraction of each layer is determined by counting the number of particles observed therein. The occupation fractions measured using the epifluorescence imaging technique are plotted in Fig. 7(a) along with the results obtained from the confocal microscopy. The two methods yield similar results.

Alternatively, we can represent the layer-occupation results in terms of the area fractions ϕ_1 and ϕ_2 of the first and second layers [see Fig. 7(b)]. Both ϕ_1 and ϕ_2 increase as ϕ is increased.

B. Numerical simulations

Here, we present results of MC simulations of the equilibrium microstructure of a HS suspension in the near wall region. The HS potential corresponds to the system with [KCl] = 0.01M, for which the electrostatic repulsion is negligible. Since the suspension used in the experiments is polydisperse, in what follows we consider both monodisperse and polydisperse systems.

1. Near-wall particle distribution

Figure 8 shows a snapshot of a typical particle configuration for a monodisperse suspension at an area fraction $\phi = 0.49$. The top and the side views are depicted. Particles in different layers are represented by different colors to enable visual assessment of the in-layer particle distribution and correlations between layers. These distributions are

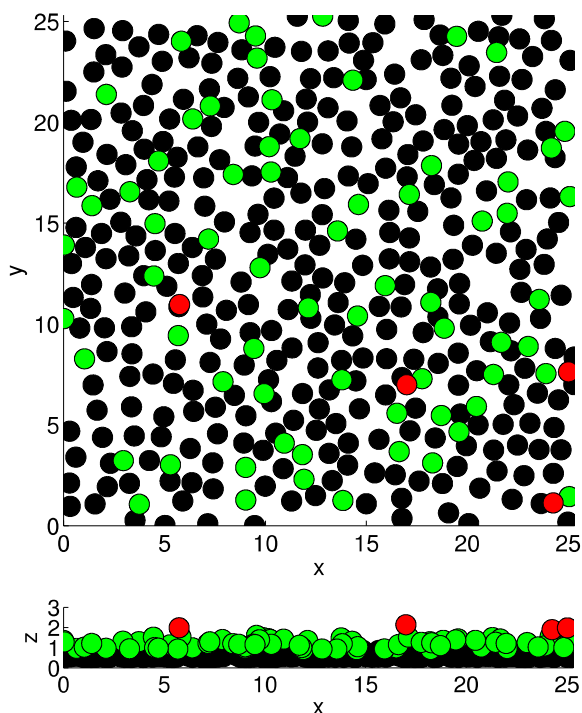


FIG. 8. Top and side views of an equilibrium particle configuration for a monodisperse HS suspension with an area fraction $\phi = 0.49$. Particles in the first layer, $z/d_0 \leq 0.9$ (black), second layer, $0.9 < z/d_0 \leq 1.8$ (green), and third layer, $z/d_0 > 1.8$ (red).

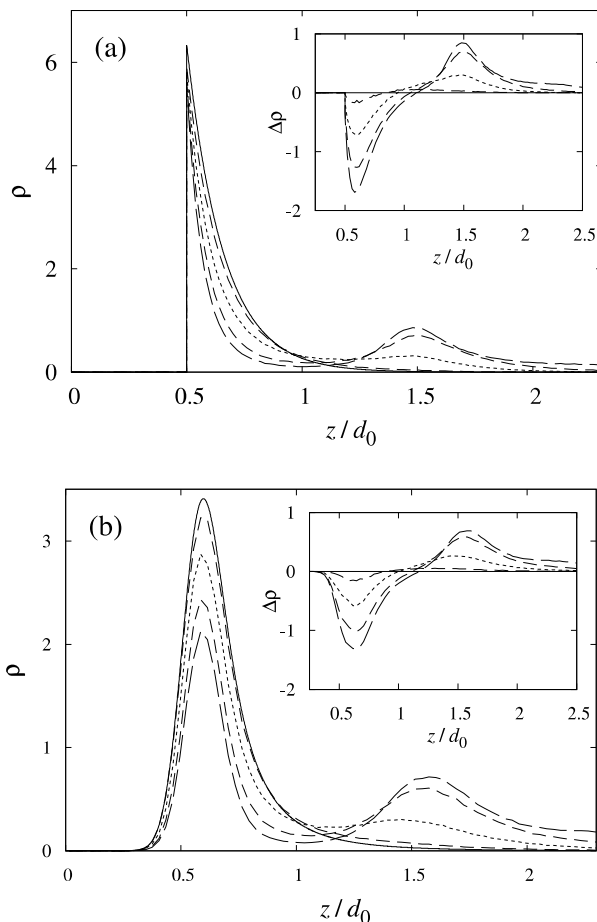


FIG. 9. Particle-wall distribution function for (a) monodisperse suspension; (b) polydisperse suspension with standard deviation of particle diameter $\sigma/d_0 = 0.15$. Simulation results for area fraction $\phi = 0$ (solid line), 0.3 (dashed), 0.6 (dotted), 0.9 (dotted-dashed), 1.2 (long-dashed). The insets show the deviation $\Delta\rho = \rho - \rho_{\phi=0}$ from the low-density distribution.

qualitatively similar to the ones observed in the experimental system [Fig. 1(a)].

The layering phenomenon we observe already at low area fractions is entropically driven, and is governed by the ratio l/d . In our system this ratio is intermediate, i.e., both sedimentation and thermal noise are significant, and hence layering does not require geometrical frustration. Figure 9 presents MC results for the suspension density profile $\rho(z)$ at several area fractions in the range $0 \leq \phi \leq 1.2$ for a monodisperse system [panel (a)] and a polydisperse system with $\sigma/d_0 = 0.15$ [panel (b)].

Similar to the experimental data discussed in Sec. IV A, the simulation results plotted in Fig. 9 indicate that there is a single layer of sedimented particles at low area fractions ϕ , and a two-layer microstructure at higher area fractions. Development of a third layer for $\phi \gtrsim 0.9$ is also noticeable in the region $z/d_0 \gtrsim 2$. Suspension polydispersity results in broadening of the peaks of the particle distribution.

These results indicate that the microstructure of individual layers is similar to the microstructure of a 2D hard-disk fluid, consistent with the experimental results shown in Figs. 1 and 4. Particles of the second layer are typically positioned over holes of the first layer, because such a particle placement minimizes the excluded volume in the configurational space. Otherwise,

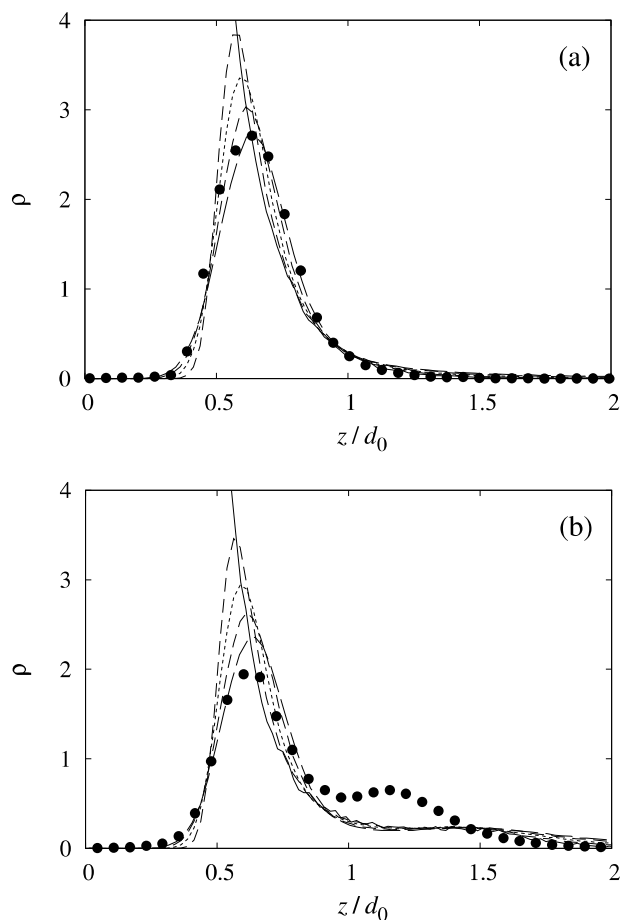


FIG. 10. Particle-wall distribution function for area fractions (a) $\phi = 0.054$ and (b) 0.54. Experimental results (solid circles); simulation results for standard deviation of particle diameter $\sigma/d_0 = 0$ (solid line), 0.1 (dashed), 0.15 (dotted), 0.20 (dashed-dotted), and 0.25 (long-dashed).

we do not observe any significant correlations between particle layers.

A direct comparison between the experimental and simulation results is presented in Fig. 10 for two values of the area fraction ϕ . At low area fractions [Fig. 10(a)], the agreement between the experiments and simulations is good. (The standard deviation of the particle-size distribution for which the simulations match the experimental data, $\sigma/d_0 \approx 0.25$, is larger than the estimated standard deviation $0.1 < \sigma/d_0 < 0.15$ based on the manufacturer's specifications; the additional spread of the experimentally observed peak can be attributed to random errors of the particle height evaluation from the confocal-microscopy images.)

A comparison of the numerical and experimental results at a higher area fraction, as shown in Fig. 10(b) [also see Figs. 5 and 9], reveals that (i) the experimentally observed second maximum of the density distribution develops at lower area fractions than the corresponding maximum in the numerical simulations; (ii) the experimental second peak is narrower, and its position is shifted towards the wall. In contrast, the plots of the excess distribution $\Delta\rho$ with respect to the low-density limit, shown in Fig. 6(a) and the insets of Fig. 9, indicate that the onset of the formation of the second layer occurs at approximately the same area fraction according to

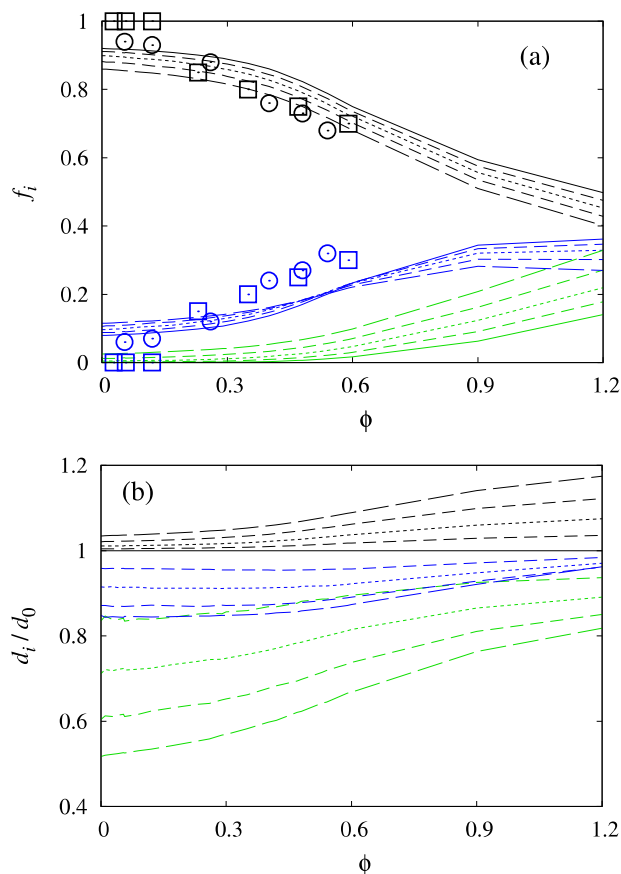


FIG. 11. (a) Occupation fraction f_i and (b) normalized average particle diameter d_i in the first particle layer (black), second layer (blue), and third layer (green), vs the total area fraction ϕ . The results for a monodisperse system (solid lines) and polydisperse systems with standard deviation of particle diameter $\sigma/d_0 = 0.1$ (dashed), 0.15 (dotted), 0.20 (dashed-dotted), and 0.25 (long-dashed). The symbols represent experimental results from confocal imaging (circles) and 2D images (squares) for a suspension with salt concentration $[\text{KCl}] = 0.01\text{M}$. Note that the experimental second layer corresponds to the sum of the second and third layers in the MC simulations. The layer boundaries in the numerical calculations are set at $z_1 = 0.9d_0$, and $z_2 = 1.8d_0$ and in the experiments are obtained from Gaussian fitting (see Fig. 5).

the simulations and experiments. Moreover, the measured and calculated occupation fractions of the layers are similar for all area fractions, as depicted in Fig. 11(a). A possible source of the observed discrepancies between the experimental and numerical results for the particle distribution $\rho(z)$ is described in the Appendix. It also provides a plausible explanation of the fact that the agreement between the experiments and MC simulations for the layer occupation fractions f_i is quite good in spite of the discrepancies for $\rho(z)$.

2. Polydispersity effects

The results in Fig. 11(a) show that the occupation fraction of the first two layers is relatively insensitive to the suspension polydispersity; in contrast, the occupation fraction of the third layer strongly increases with the standard deviation of particle diameter. This increase stems from the presence of smaller (lighter) particles in polydisperse systems: smaller particles tend to migrate into the top layer, as evident from Fig. 11(b).

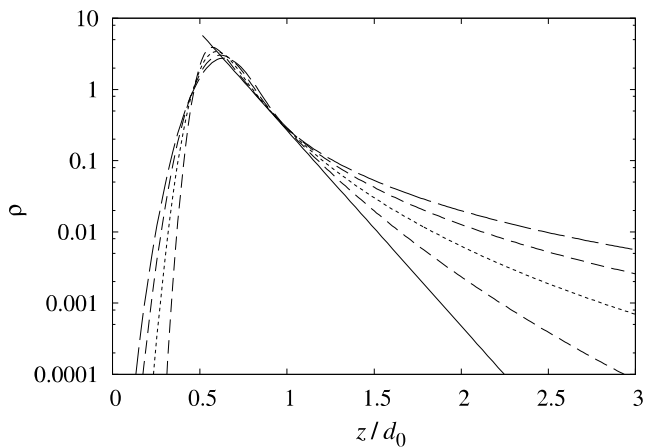


FIG. 12. Low-density limit of the near-wall particle distribution for a monodisperse system (solid line) and polydisperse systems with standard deviation of particle diameter $\sigma/d_0=0.1$ (dashed), 0.15 (dotted) 0.20 (dashed-dotted), and 0.25 (long-dashed).

For dilute suspensions, the particle-size segregation results in variation of the slope of $\log \rho(z)$ with the distance from the wall, as illustrated in Fig. 12. We estimate that this variation causes an approximately 20% uncertainty of the calibration of the confocal height measurements described in Sec. II C.

C. A quasi-2D model of the equilibrium layered microstructure

Here, we present a semi-quantitative theoretical model for evaluating the occupation fractions f_i of the particle layers in a sedimented colloidal suspension. Our theory is based on the assumption that the suspension microstructure can be approximated as a collection of weakly coupled quasi-2D layers in thermodynamic equilibrium with respect to particle exchange.

The equilibrium condition for layers i and $i + 1$ is

$$\mu_i + mgz_i = \mu_{i+1} + mgz_{i+1}, \quad (24)$$

where μ_i is the chemical potential of layer i , and z_i is its position. According to Eq. (24), the next layer forms when the free-energy penalty $\delta F = \mu_i dN$, associated with inserting additional particles into a given layer i , exceeds the extra potential energy needed to place the particles into the new layer $i + 1$ above it. In our model, μ_i is approximated as the chemical potential of a 2D hard-disk fluid of area fraction ϕ_i . All disk diameters are equal to the sphere diameter d , which corresponds to a layer of spheres with the same vertical position z .

In the low area-fraction limit, the chemical potential of a hard-disk fluid is

$$\mu_i = k_B T \ln \phi_i + C(T), \quad (25)$$

where $C(T)$ depends only on the temperature T . According to equilibrium condition (24) and equation of state (25), we thus have

$$\phi_{i+1} = r \phi_i, \quad i = 1, 2, \dots \quad (26)$$

with the ratio r given by the Boltzmann factor

$$r = e^{-\Delta/l}, \quad (27)$$

where l is defined by Eq. (4) and $\Delta = z_{i+1} - z_i$. We assume that the layer separation Δ is independent of i .

For finite area fractions, relation (26) is replaced with

$$\phi_{i+1} = r(\phi_i) \phi_i, \quad i = 1, 2, \dots, \quad (28)$$

where the layer occupation ratio r depends on the area fraction in the adjacent layers. The factor $r(\phi)$ is determined from equilibrium condition (24) with the help of the Gibbs–Duhem relation

$$d\mu = \frac{\pi d^2}{4} \phi^{-1} dp, \quad (29)$$

where p is the lateral 2D pressure within the layer. Combining (24), (28), and (29) yields

$$\frac{dr}{d\phi} = r \left[\frac{p'(\phi)}{p'(r\phi)} - 1 \right], \quad (30)$$

where

$$p' = \left(\frac{\partial p}{\partial \phi} \right)_T. \quad (31)$$

Differential equation (30) is solved for $r = r(\phi)$ with boundary condition (27) at $\phi = 0$. Occupation fractions $f_i = \phi_i / \phi$ are then determined by iteration, applying Eq. (28) and the relation

$$\phi = \sum_{i=1}^{\infty} \phi_i. \quad (32)$$

We have solved Eq. (30) and determined the occupation fractions f_i using the scaled-particle-theory equation of state for hard disks,⁵¹

$$\frac{\pi d^2 p}{4k_B T} = \frac{\phi}{(1 - \phi)^2}. \quad (33)$$

The results of our calculations are presented in Fig. 13 for a HS system with the same value of sedimentation length (11) as in our MC simulations. Based on the separation between the first and second peak of the suspension density profile shown in Fig. 9(a), the calculations were performed for $\Delta/d = 1$.

The theoretical results in Fig. 13 are compared with the MC simulations of a monodisperse HS suspension with the boundaries between the layers set to $z_1 = d$ and $z_2 = 2d$,

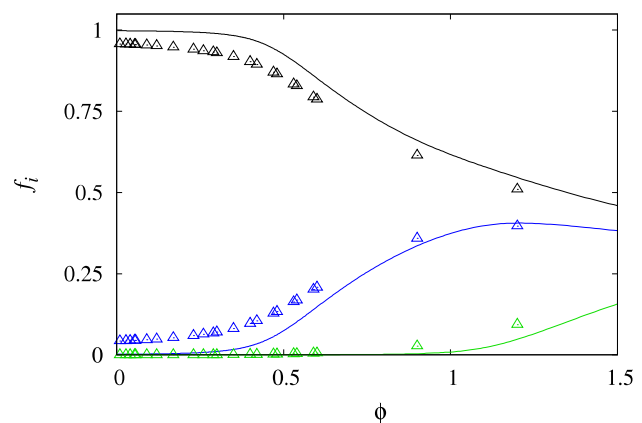


FIG. 13. Occupation fraction f_i for the first (black), second (blue), and third (green) layer vs the total area fraction ϕ for a monodisperse HS suspension. Theoretical results (solid lines), MC simulations (symbols).

consistent with the peak positions. The agreement between our simple theory and simulations is quite good. A similar agreement was obtained for other values of the dimensional parameter l/d (results not shown).

The layer boundaries used in Secs. IV B and V B to compare the MC results with experiments differ from the boundaries used in the above model by approximately 10%. Due to the observed deviation between the measured and simulated particle distributions (see Fig. 10), it is not possible to define the layer boundaries in a unique, equivalent way for the experimental and simulated systems. Therefore, the layer boundaries $z_1 = 0.9d$ and $z_2 = 1.8d$ used in Secs. IV B and V B were chosen based on the comparison between the experimental and numerical results for the occupation fractions and self-diffusivities in particle layers.

V. PARTICLE DYNAMICS

A. Experimental results

The short time self-diffusion coefficient in the x - y plane, D_s , is determined for different total area fractions of the sedimented particles by extracting mean square displacement (22) from 2D epifluorescent images of the first and second particle layer. The mean-square displacement is measured over a time interval τ that is small compared to the structural relaxation time of the suspension, to ensure that the measurements yield the short-time self-diffusion coefficient.

The results are shown in Fig. 14 for suspensions with salt concentration $[\text{KCl}] = 0.01\text{M}$ and salt-free suspensions with $[\text{KCl}] = 0\text{M}$. The self-diffusion coefficient is expected to decrease as the particle concentration increases; indeed, we

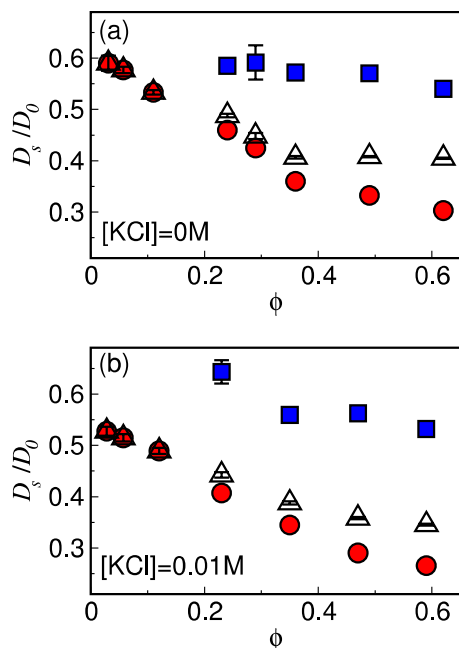


FIG. 14. Short-time self-diffusion coefficient D_s , normalized by the Stokes-Einstein diffusion coefficient D_0 , as a function of the total area fraction ϕ ; circles (squares) correspond to the first (second) layer, and triangles to the effective D_s calculated by the weighted average of the self-diffusion coefficients for the two individual layers. (a) Suspension with no added salt. (b) Suspension with salt concentration $[\text{KCl}] = 0.01\text{M}$.

observe this decrease for both salt concentrations and in both layers, for $\phi < 0.4$. In the case of $[\text{KCl}] = 0.01\text{M}$, corresponding to $\lambda = 5\text{ nm}$, the particles can get much closer to the cell floor, which in turn results in lower values of the self-diffusion coefficient compared to suspensions with $[\text{KCl}] = 0\text{M}$.

Using a linear fit to the values of D_s/D_0 for the low area fractions, where there is no observable second layer, we can extrapolate to $\phi = 0$ and extract the self-diffusivity of a single particle. The extrapolated results agree well with the measurements at very low concentrations $\phi < 0.003$, as discussed in Sec. IV A 1.

From the known occupation fractions f_1 and f_2 for each ϕ , we can weigh the contribution of each layer to the total self-diffusivity, and construct an effective D_s of the whole suspension (Fig. 14). As expected, for $\phi < 0.4$ the effective self-diffusion coefficient D_s decreases as ϕ is increased in both salt concentrations. For larger ϕ we observe a flattening of D_s , which clearly indicates that the second layer becomes dominant in those area fractions. This observation is supported also by the saturation of ϕ_1 at $\phi > 0.45$ [Fig. 7(b)].

B. Numerical simulations

The results of our numerical simulations for the short-time lateral self-diffusion coefficient D_s in a HS system are presented in Fig. 15 for a monodisperse suspension and for polydisperse suspensions with $\sigma/d_0 = 0.1$ and 0.15 . Figure 16 shows the corresponding results for a system of monodisperse hard spheres with particle-wall and particle-particle electrostatic repulsion (5) and (6).

The results depicted in Fig. 15 indicate that for moderately polydisperse suspensions (in the range corresponding to the polydispersity of silica particles used in the experiments), the self-diffusion coefficient is only moderately dependent on σ/d_0 . For larger values of the variance of particle diameters, the normalized self-diffusion coefficient D_s/D_0 significantly

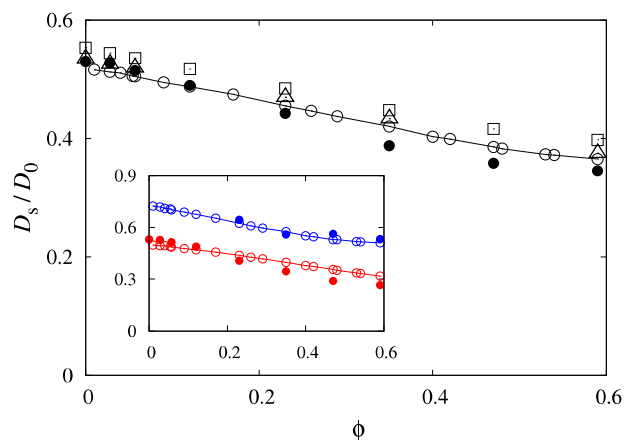


FIG. 15. Normalized short-time self-diffusion coefficient D_s/D_0 , as a function of the area fraction ϕ for a suspension with salt concentration $[\text{KCl}] = 0.01\text{M}$. The main panel shows D_s averaged over the whole system, and the inset shows D_s for the first (bottom, red) and second (top, blue) particle layer. Experimental results (solid circles); simulation results (open symbols) for a monodisperse system (circles) and polydisperse systems with the standard deviation of the particle diameter $\sigma = 0.1d_0$ (triangles) and $0.15d_0$ (squares). Note that at low area fractions the triangles overlap with the solid circles. The lines are a guide for the eye.

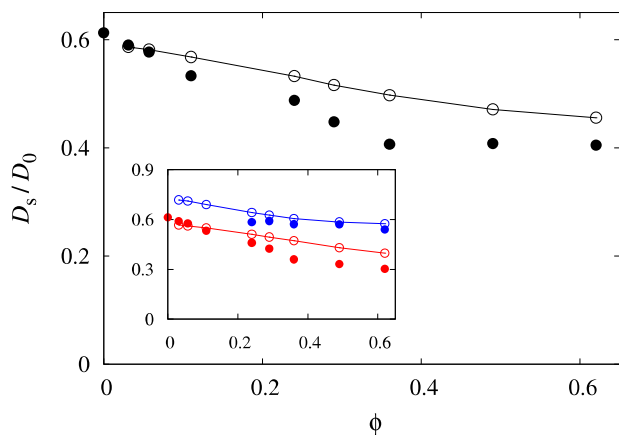


FIG. 16. Normalized short-time self-diffusion coefficient D_s/D_0 , as a function of the area fraction ϕ for a suspension with no salt. Symbols are the same as in Fig. 15. Results are shown only for monodisperse suspensions.

increases with the degree of the polydispersity, because the mobility is dominated by small particles. This increase is illustrated in Fig. 17 for a suspension in the low-area-fraction limit $\phi = 0$.

The results of our hydrodynamic calculations for a HS suspension and for a suspension with screened electrostatic repulsion are compared with experimental results for suspensions with $[KCl] = 0.01M$ (Fig. 15) and $[KCl] = 0M$ (Fig. 16). In the case of $[KCl] = 0.01M$, the numerical and experimental results agree within expected experimental inaccuracies. For the case of $[KCl] = 0M$, the differences between experiment and simulation cannot be explained solely by experimental errors. Such discrepancies can arise from a difference between the layer heights comparing experiment to simulation (see Fig. 10). This in turn might arise from additional unaccounted electrostatic interactions.

Our results show that the particle–wall hydrodynamic interactions significantly hinder particle diffusion. For example, for a monodisperse suspension in the low density regime, the effective self-diffusivity is decreased by approximately 50% due to the wall presence, according to the results depicted in Fig. 17 ($\sigma/d \rightarrow 0$). A numerical estimate of the lateral self-diffusion coefficient in a particle layer in the

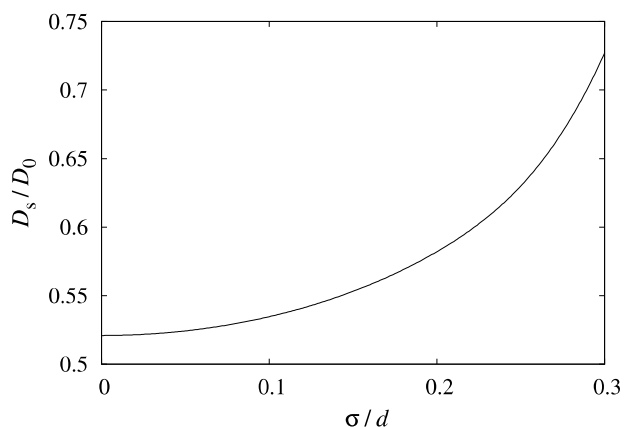


FIG. 17. Normalized short-time self-diffusion coefficient D_s/D_0 in the low-area-fraction limit $\phi = 0$ (for the system with salt) as a function of the suspension polydispersity.

absence and in the presence of the wall indicates that the wall hindrance effect is nearly as strong for the area fraction $\phi = 0.6$ (the largest value considered in our study) as in the low-density limit.

This trend differs from the behavior of semi-infinite suspensions confined by a planar wall, as determined using the evanescent wave dynamic light scattering technique.^{16,19,52} In the evanescent-wave scattering studies, it was observed that at high suspension volume fractions the self-diffusion coefficient averaged over a near-wall layer approaches the bulk value; it was thus concluded that, as the volume fraction increases, the wall effect is dominated by the interparticle hydrodynamic interactions.

It should be noted, however, that the assessment of the effect of the wall on the suspension dynamics was done differently here and in the evanescent-wave studies.^{16,19,52} We compare the self-diffusivity values for the same particle configuration in the presence and absence of the wall, whereas Michailidou *et al.*^{16,19} and Liu *et al.*⁵² compare wall bounded and unconfined bulk systems. There is, thus, no contradiction between our present results for particle diffusion in a sedimented particle layer and the earlier findings for the near-wall dynamics in wall-bounded bulk suspensions.

VI. DISCUSSION

In this paper, we have studied in detail the structure and dynamics of quasi-2D colloidal suspensions near a wall, comparing experiment, numerics, and analytical calculations. This study complements earlier ones on colloids near surfaces in several respects. While previous measurements using total internal reflection microscopy examined the height distribution and diffusion of single particles,^{7–9} our holographic, confocal, and video microscopies have provided the height distributions and dynamics of many-particle layers. An earlier investigation of dense sedimented monolayers was focused on heavy particles, whose size significantly exceeded their sedimentation length,³⁷ whereas our layer is much more thermally excited, allowing for elaborate structure perpendicular to the surface. Experiments using evanescent wave dynamic light scattering provided information on the collective (Fourier-space) diffusion of 3D suspensions near a wall,^{16–19,52} while ours have explored the real-space diffusion in a quasi-2D scenario.

Before discussing the results and their implications, we would like to briefly summarize the three most significant findings. (a) We have identified a distinctive structural feature of sedimented layers, the sequential appearance of second and third sub-layers at relatively low values of area fraction. (b) We have observed a profound effect of the layering on the self-diffusion of particles parallel to the substrate. (c) Polydispersity is found to have a strong effect on the structure and dynamics of colloidal particles sedimented above the wall.

Our central result is a rather sharp formation of a distinct second layer at an area fraction of $\phi \sim 0.3$. This value is much lower than the area fraction required for close-packing or other 2D structural changes such as the formation of hexatic or crystalline order. One important consequence of this result concerns the apparent self-diffusion of the particles in the suspension and its dependence on particle density. Due

to the higher mobility of the particles in the elevated layer, the effective diffusivity is higher and levels off as particle density increases. The experimentally observed behavior could be interpreted incorrectly if one is unaware of the layering (or stratifying) effect.

We find good agreement between experimental and simulation results for the occupation fractions of the first and second layers and for the lateral self-diffusivity (both for the entire suspension and in the individual layers). However, we also find an unexpected discrepancy in the position and the height of the second peak in the near-wall particle distribution. While the source of this discrepancy is unknown, one possibility, related to optical aberrations, is suggested in the [Appendix](#). On the other hand, the difference between theory and experiment might also be a result of an actual physical effect, such as more complicated electrostatic interactions setting in at higher layer densities.

Another new insight put forth in this study is the significant effect that polydispersity has on the occupation and composition of layers close to the bottom wall, even in the case of a relatively small dispersion of particle sizes. The effect of polydispersity is evident already at low densities, since the smaller and larger particles segregate into the upper and lower layers, respectively. We expect the phenomena described here to be quite general and to be manifested in any such system where the sedimentation length l is of the order of the particle diameter. This conclusion is supported by the appearance of the phenomena both in experiments and in Monte Carlo simulations.

An important outcome of this paper is the construction of a very simple theoretical quasi-2D model of the layered microstructure in thermodynamic equilibrium. Such systems have been analyzed earlier using density-functional theory,⁵³ but our theoretical model is much simpler and easier to apply. We have demonstrated that the model approximates well the experimental and numerical results for the system studied in this work.

We conclude with three open issues. Layering phenomena near a wall are well documented in 3D suspensions as well.¹⁻³ An interesting question is whether this perturbation to the 3D pair correlation function could be fundamentally related to the sequential layering reported here. The structural features near the wall should also affect two- and many-particle dynamics in the quasi-2D suspensions, which can be characterized by two-point microrheology. Finally, taking a more detailed account of interparticle forces such as strong electrostatic interactions may hopefully provide deeper understanding of the effects observed in this work.

ACKNOWLEDGMENTS

H.D. wishes to thank the Polish Academy of Sciences for its hospitality. This research has been supported by the Israel Science Foundation (Grant Nos. 8/10 and 164/14) and by the Marie Curie Reintegration Grant (No. PIRG04-GA-2008-239378). A.S.-S acknowledges funding from the Tel-Aviv University Center for Nanoscience and Nanotechnology. M.L.E.-J. and E.W. were supported in part by Narodowe Centrum Nauki (National Science Centre) under Grant No.

2012/05/B/ST8/03010. J.B. would like to acknowledge the financial support from National Science Foundation (NSF) Grant No. CBET 1059745. He would also like to acknowledge the hospitality and financial support from IPPT PAN during his summer visits.

APPENDIX: OPTICAL EFFECTS ON MEASURED PARTICLE DISTRIBUTIONS

We present a simple model to support a hypothesis that the discrepancy between the measured and calculated near-wall particle distributions stems from optical aberration caused by nonuniform optical properties of the suspension in the near-wall region. We assume that such aberration produces a nonlinear rescaling of the coordinate z ,

$$\tilde{z} = \tilde{z}(z), \quad (\text{A1})$$

where z is the actual and \tilde{z} is the measured particle position. The rescaling (A1) results in the corresponding transformation of the particle density

$$\tilde{\rho}(\tilde{z}) = \rho(z) \frac{dz}{d\tilde{z}}. \quad (\text{A2})$$

To demonstrate that a distortion (A1) can produce the observed shift and change of height of the features of the distribution ρ , we consider an *ad hoc* distortion model with the transformation between the measured and actual vertical coordinates given by the equations

$$\frac{d\tilde{z}}{dz} = \begin{cases} 1, & z < z_1, \\ 1 - (1-b) \frac{z-z_1}{z_2-z_1}, & z_1 \leq z \leq z_2, \\ b, & z_2 < z, \end{cases} \quad (\text{A3a})$$

and

$$b = \alpha\phi, \quad (\text{A3b})$$

where z_1 , z_2 , and α are the model parameters. Transformation (A3) describes position-dependent coordinate contraction with the amplitude gradually increasing in the region $z_1 \leq z \leq z_2$ (the region where the second peak occurs according to the experimental data). The overall deviation of the Jacobian (A3) from unity is proportional to the area fraction of the suspension layer.

Figure 18(a) compares distorted distribution (A2) with the corresponding untransformed distribution $\rho(z)$ obtained from MC simulations of a HS suspension at the area fraction $\phi = 0.54$. Figure 18(b) presents the distorted distribution for the set of area fractions for which experimental results are depicted in Fig. 5(a). The parameter values of transformation (A3) are given in the figure caption.

The results show that coordinate transformation (A3a) shifts the position of the second particle layer to the left and produces a corresponding enhancement of the peak of particle distribution, similar to the experimentally observed features of the distributions depicted in Figs. 5(a) and 10(b). Thus, our calculations provide indirect support to our optical-distortion hypothesis. The distortion hypothesis can also explain why the measured and calculated occupation fractions and self-diffusivities of the particles in the top layer agree well (see

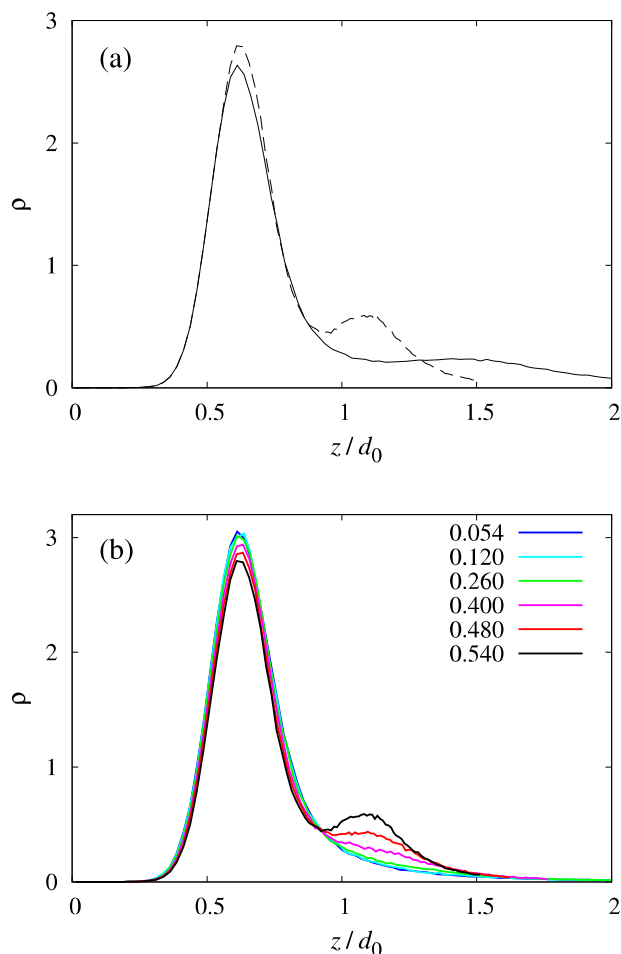


FIG. 18. The effect of model distortion transformation (A3) on the particle distribution $\rho(z)$ in a HS suspension with the standard deviation of the particle distribution $\sigma/d_0 = 0.2$. (a) A comparison of the MC result for $\rho(z)$ (solid line) with transformed distribution (A2) (dashed line) at the area fraction $\phi = 0.54$; (b) the transformed distribution for different area fractions (as labeled). The parameters of transformation (A3) are $z_1/d = 0.55$, $z_2/d = 1.2$, and $\alpha = 2.5$.

Figs. 11 and 15), in spite of the fact that the observed and calculated positions of the layer differ significantly.

It is an open question what the source of distortion (A1) might be. Since the suspension is imaged from above in our confocal-microscopy system, we hypothesize that reflection of laser light from the first (bottom) particle layer results in stray illumination of the second layer, producing distorted particle height measurements. The optical distortion hypothesis can be verified by experiments using refractive-index matched suspensions, but such investigations are beyond the scope of the present study.

¹D. H. Van Winkle and C. A. Murray, *J. Chem. Phys.* **89**, 3885 (1988).

²P. González-Mozuelos, M. Medina-Noyola, B. D'Aguzzo, J. M. Méndez-Alcaraz, and R. Klein, *J. Chem. Phys.* **95**, 2006 (1991).

³M. Zurita-Gotor, J. Bławdziewicz, and E. Wajnryb, *Phys. Rev. Lett.* **108**, 068301 (2012).

⁴J. Happel and H. Brenner, *Low Reynolds Number Hydrodynamics* (Martinus Nijhoff, The Hague, 1983).

⁵G. S. Perkins and R. B. Jones, *Physica A* **189**, 447 (1992).

⁶B. Cichocki and R. B. Jones, *Physica A* **258**, 273 (1998).

⁷J. Y. Walz and L. Suresh, *J. Chem. Phys.* **103**, 10714 (1995).

⁸D. C. Prieve, *Adv. Colloid Interface Sci.* **82**, 93 (1999).

⁹D. S. Sholl, M. K. Fenwick, E. Atman, and D. C. Prieve, *J. Chem. Phys.* **113**, 9268 (2000).

¹⁰M. D. Carbajal-Tinoco, R. Lopez-Fernandez, and J. L. Arauz-Lara, *Phys. Rev. Lett.* **99**, 138303 (2007).

¹¹J. Bławdziewicz, M. L. Ekiel-Jeżewska, and E. Wajnryb, *J. Chem. Phys.* **133**, 114703 (2010).

¹²E. R. Dufresne, T. M. Squires, M. P. Brenner, and D. G. Grier, *Phys. Rev. Lett.* **85**, 3317 (2000).

¹³B. Cichocki, M. L. Ekiel-Jeżewska, and E. Wajnryb, *J. Chem. Phys.* **126**, 184704 (2007).

¹⁴M. Zurita-Gotor, J. Bławdziewicz, and E. Wajnryb, *J. Fluid Mech.* **592**, 447 (2007).

¹⁵S. G. Anekal and M. A. Bevan, *J. Chem. Phys.* **125**, 034906 (2006).

¹⁶V. N. Michailidou, G. Petekidis, J. W. Swan, and J. F. Brady, *Phys. Rev. Lett.* **102**, 068302 (2009).

¹⁷B. Cichocki, E. Wajnryb, J. Bławdziewicz, J. K. G. Dhont, and P. Lang, *J. Chem. Phys.* **132**, 074704 (2010).

¹⁸B. Loppinet, J. K. G. Dhont, and P. Lang, *Eur. Phys. J. E* **35**, 62 (2012).

¹⁹V. N. Michailidou, J. W. Swan, J. F. Brady, and G. Petekidis, *J. Chem. Phys.* **139**, 164905 (2013).

²⁰M. D. Carbajal-Tinoco, F. Castro-Roman, and J. L. Arauz-Lara, *Phys. Rev. E* **53**, 3745 (1996).

²¹M. Schmidt and H. Löwen, *Phys. Rev. E* **55**, 7228 (1997).

²²R. Zangi and S. A. Rice, *Phys. Rev. E* **61**, 660 (2000).

²³D. Frydel and S. A. Rice, *Phys. Rev. E* **68**, 061405 (2003).

²⁴Y. Han, Y. Shokef, A. M. Alsayed, P. Yunker, T. C. Lubensky, and A. G. Yodh, *Nature* **456**, 898 (2008).

²⁵B. H. Lin, J. Yu, and S. A. Rice, *Phys. Rev. E* **62**, 3909 (2000).

²⁶E. R. Dufresne, D. Altman, and D. G. Grier, *Europhys. Lett.* **53**, 264 (2001).

²⁷M. Ekiel-Jeżewska, E. Wajnryb, J. Bławdziewicz, and F. Feuillebois, *J. Chem. Phys.* **129**, 181102 (2008).

²⁸B. Cui, H. Diamant, B. Lin, and S. A. Rice, *Phys. Rev. Lett.* **92**, 258301 (2004).

²⁹S. Bhattacharya, J. Bławdziewicz, and E. Wajnryb, *J. Fluid Mech.* **541**, 263 (2005).

³⁰H. Diamant, B. Cui, B. Lin, and S. A. Rice, *J. Phys.: Condens. Matter* **17**, S4047 (2005).

³¹J. Bławdziewicz and E. Wajnryb, *J. Phys.: Conf. Ser.* **392**, 012008 (2012).

³²M. Baron, J. Bławdziewicz, and E. Wajnryb, *Phys. Rev. Lett.* **100**, 174502 (2008).

³³B. Lin, S. A. Rice, and D. A. Weitz, *Phys. Rev. E* **51**, 423 (1995).

³⁴B. Cichocki, M. L. Ekiel-Jeżewska, G. Nagele, and E. Wajnryb, *J. Chem. Phys.* **121**, 2305 (2004).

³⁵Y. Peng, W. Chen, T. M. Fischer, D. A. Weitz, and P. Tong, *J. Fluid Mech.* **618**, 243 (2009).

³⁶W. Zhang, S. Chen, N. Li, J. Z. Zhang, and W. Chen, *PLoS One* **9**, e85173 (2014).

³⁷T. O. E. Skinner, D. G. A. L. Aarts, and R. P. A. Dullens, *Phys. Rev. Lett.* **105**, 168301 (2010).

³⁸D. Kapfenberger, A. Sonn-Segev, and Y. Roichman, *Opt. Express* **21**, 12228 (2013).

³⁹S.-H. Lee and D. G. Grier, *Opt. Express* **15**, 1505 (2007).

⁴⁰F. C. Cheong, B. J. Krishnatreya, and D. G. Grier, *Opt. Express* **18**, 13563 (2010).

⁴¹M. Polin, D. G. Grier, and Y. Han, *Phys. Rev. E* **76**, 041406 (2007).

⁴²S. H. Behrens and D. G. Grier, *J. Chem. Phys.* **115**, 6716 (2001).

⁴³J. N. Israelachvili, *Intermolecular and Surface Forces* (Academic Press, London, 1992).

⁴⁴D. Frenkel and B. Smit, *Understanding Molecular Simulation. From Algorithms to Simulations* (Academic Press, New York, 2002).

⁴⁵J. Bławdziewicz and E. Wajnryb, *Phys. Fluids* **20**, 093303 (2008).

⁴⁶S. Bhattacharya, J. Bławdziewicz, and E. Wajnryb, *Physica A* **356**, 294 (2005).

⁴⁷B. Cichocki and B. U. Felderhof, *Physica A* **159**, 19 (1989).

⁴⁸K. Sadlej, E. Wajnryb, J. Bławdziewicz, M. Ekiel-Jeżewska, and Z. Adamczyk, *J. Chem. Phys.* **130**, 144706 (2009).

⁴⁹G. Abade, B. Cichocki, M. L. Ekiel-Jeżewska, G. Nagele, and E. Wajnryb, *J. Chem. Phys.* **132**, 014503 (2010).

⁵⁰J. C. Crocker and D. G. Grier, *J. Colloid Interface Sci.* **179**, 298 (1996).

⁵¹E. Helfand, H. L. Frisch, and J. L. Lebowitz, *J. Chem. Phys.* **34**, 1037 (1961).

⁵²Y. Liu, J. Bławdziewicz, B. Cichocki, J. K. G. Dhont, M. Lisicki, E. Wajnryb, Y.-N. Young, and P. R. Lang, "Near-wall dynamics of concentrated hard-sphere suspensions: comparison of evanescent wave DLS experiments, virial approximation and simulations," *Soft Matter* (to be published).

⁵³H. Chen and H. Ma, *J. Chem. Phys.* **125**, 024510 (2006).

Viscoelastic Response of a Complex Fluid at Intermediate Distances

Adar Sonn-Segev,¹ Anne Bernheim-Groswasser,² Haim Diamant,¹ and Yael Roichman^{1,*}

¹*Raymond and Beverly Sackler School of Chemistry, Tel Aviv University, Tel Aviv 6997801, Israel*

²*Department of Chemical Engineering, Ilse Katz Institute for Nanoscale Science and Technology, Ben Gurion University of the Negev, Beer-Sheva 84105, Israel*

(Received 16 July 2013; revised manuscript received 3 October 2013; published 25 February 2014)

The viscoelastic response of complex fluids is length- and time-scale dependent, encoding information on intrinsic dynamic correlations and mesoscopic structure. We study the length scale above which bulk viscoelasticity sets in, and the material response that precedes it at shorter distances. We show that the crossover between these two regimes may appear at a surprisingly large distance. We generalize the framework of microrheology to include both regimes and apply it to F-actin networks, thereby extracting their dynamic correlation length from their bulk and local viscoelastic properties.

DOI: 10.1103/PhysRevLett.112.088301

PACS numbers: 47.57.Qk, 87.16.dm, 87.16.dj, 87.16.Ln

Most fluids in nature and industry are complex, or structured [1], in the sense that they include mesoscopic elements in between the molecular and macroscopic scales. For example, in suspensions, micron-scale solid particles are dispersed in a molecular fluid, and in polymer gels the polymer chains form a network embedded within a molecular solvent. Consequently, the response of complex fluids to stress is characterized by intermediate length and time scales.

The bulk viscoelastic response of such materials is commonly measured using macrorheology [2]. Similar information, for a wider frequency range and smaller material quantity, can be extracted from microrheology by following the motions of embedded tracer particles [3–8]. In one-point (1P) microrheology [3–5] the thermal fluctuations of a single particle are used to infer the viscoelastic properties of the medium via a generalized Stokes-Einstein relation (GSER). It has been found that this measurement is affected by the local environment of the tracer particle [9,10], and thus, may fail to reproduce the material's bulk response. Two-point (2P) microrheology [6] overcomes this obstacle by tracking the correlated motions of particle pairs as a function of their separation. 2P measurements have focused on asymptotically large separations, where the pair correlation has a universal form due to momentum conservation.

The current Letter addresses two questions: (i) Beyond what length scale does the bulk viscoelastic behavior emerge? (ii) What is the material response at smaller length scales? We find that the leading correction to the asymptotic behavior at large distances, referred to, hereafter, as the subdominant response, may be unexpectedly large, causing the bulk response to set in at surprisingly large distances. The physical origin of the subdominant response, which is unique to complex fluids, is different from that of the asymptotic one. It is related as well to a conservation law (of fluid mass rather than momentum), resulting in a

generic system-independent form. The study of this distinctive regime leads to a more complete description of the complex-fluid response.

We first derive the generic form of the subdominant response and, subsequently, confirm the general predictions in a specific theoretical example, the two-fluid model of polymer gels [8,11,12]. Extending the framework of microrheology to include the subdominant term, we validate its significant effect in a model experimental system, entangled F-actin networks of various concentrations.

We set the stage by recalling the classical Stokes problem of a rigid sphere of radius a , driven by a steady force \mathbf{F} through an incompressible fluid of viscosity η [13]. The fluid velocity at position \mathbf{r} away from the sphere's center is given by $\mathbf{v}(\mathbf{r}) = \mathbf{v}_1 + \mathbf{v}_2$, with $v_{1\alpha} = (8\pi\eta r)^{-1}(\delta_{\alpha\beta} + \hat{\mathbf{r}}_\alpha \hat{\mathbf{r}}_\beta)F_\beta$ and $v_{2\alpha} = a^2(24\pi\eta r^3)^{-1}(\delta_{\alpha\beta} - 3\hat{\mathbf{r}}_\alpha \hat{\mathbf{r}}_\beta)F_\beta$, where Greek indices denote the coordinates (x, y, z) , and repeated indices are summed over. The dominant term at large distances, \mathbf{v}_1 , is the flow due to a force monopole \mathbf{F} . Its r^{-1} decay is dictated by momentum conservation, ensuring that the integrated momentum flux (proportional to $\nabla \mathbf{v}_1 \sim r^{-2}$) through any closed surface around the sphere remain fixed. This dominant response can be decomposed into longitudinal and transverse components (force and velocity parallel and perpendicular to \mathbf{r} , respectively), $v_{1\parallel} = (4\pi\eta r)^{-1}F_{\parallel}$, $v_{1\perp} = (8\pi\eta r)^{-1}F_{\perp}$, both of which are positive. Turning to the subdominant \mathbf{v}_2 , we point out the largely overlooked fact that it is actually made of two contributions, having the same spatial form but opposite signs and different physical origins, $\mathbf{v}_2 = \mathbf{v}_{2f} + \mathbf{v}_{2m}$. The first, $\mathbf{v}_{2f} = 3\mathbf{v}_2$, is the flow due to a force quadrupole $Q_{\gamma\alpha\beta} = \frac{1}{2}a^2\delta_{\gamma\alpha}F_\beta$. We focus our attention on the opposite contribution, $\mathbf{v}_{2m} = -2\mathbf{v}_2$. It is the flow due to a mass dipole $\mathbf{m} = -[a^2/(3\eta)]\mathbf{F} = -2\pi a^3\mathbf{U}$, created opposite to the direction of the sphere's displacement, where $\mathbf{U} = (6\pi\eta a)^{-1}\mathbf{F}$ is the sphere's velocity. The net subdominant term introduces a negative correction to the

longitudinal response, $v_{2\parallel} = -a^2(12\pi\eta r^3)^{-1}F_{\parallel}$, and a positive correction to the transverse one, $v_{2\perp} = a^2(24\pi\eta r^3)^{-1}F_{\perp}$. Since the simple fluid has no intrinsic length scale, these corrections vanish as $a \rightarrow 0$.

Now, contrast the above with the case of an isotropic viscoelastic medium [14], having a frequency-dependent complex shear modulus $G(\omega) = G'(\omega) + iG''(\omega)$ [i.e., bulk shear viscosity $\eta_b(\omega) = G(\omega)/(-i\omega)$]. Dynamic correlations in the medium (as measured, e.g., by dynamic scattering) decay with a characteristic correlation length ξ_d , which in polymer solutions is believed to coincide with the static mesh size ξ_s [11]. Consider a sphere of radius a , driven through the medium by an oscillatory force $\mathbf{F}e^{-i\omega t}$. At sufficiently large distances the medium velocity must be dominated by the monopolar $v_{1\alpha} = (8\pi\eta_b r)^{-1}(\delta_{\alpha\beta} + \hat{\mathbf{r}}_{\alpha}\hat{\mathbf{r}}_{\beta})F_{\beta}$, for the same momentum-conservation reasons given above. This is the basis of present 2P microrheology [6–8]. The two subdominant r^{-3} contributions, however, become separated. Consider first the limit $a/\xi_d \rightarrow 0$, for which the separation is largest. (Because of the intrinsic length scale ξ_d , v_2 does not vanish in this case.) The force quadrupole, $Q \sim \xi_d^2 F$, creates a flow $v_{2f} \sim \xi_d^2(\eta_b r^3)^{-1}F$, dependent (like the monopolar v_1) on bulk viscosity. By contrast, the mass dipole in this limit arises from fluid displacement at scales smaller than ξ_d , where the relevant viscosity is the solvent's, η ; hence, $m \sim -(\xi_d^2/\eta)F$, creating a flow $v_{2m} \sim -\xi_d^2(\eta r^3)^{-1}F$. Thus, v_{2m} is enhanced relative to v_{2f} by a factor of η_b/η , which is typically very large. In such a case of a large contrast between local and bulk response, the mass-dipole term takes over the subdominant response and changes its sign, $v_{2\alpha} \approx v_{2m,\alpha} \sim -\xi_d^2(\eta r^3)^{-1}(\delta_{\alpha\beta} - 3\hat{\mathbf{r}}_{\alpha}\hat{\mathbf{r}}_{\beta})F_{\beta}$. This has two distinctive consequences: (a) The corrections to the longitudinal and transverse responses flip signs, $v_{2\parallel} = \xi_d^2(\eta r^3)^{-1}F_{\parallel}$, $v_{2\perp} \sim -\xi_d^2(\eta r^3)^{-1}F_{\perp}$. (b) The crossover to the asymptotic r^{-1} term is pushed further to a distance $r_c \sim (\eta_b/\eta)^{1/2}\xi_d \gg \xi_d$. In the opposite limit of an arbitrarily large sphere, $a/\xi_d \rightarrow \infty$, only bulk properties matter, and we have $Q \sim a^2 F$, $m \sim -(a^2/\eta_b)F$, making v_{2f} and v_{2m} comparable again. To interpolate between the two limits, we define a local viscosity at the scale of the probe, $\eta_{\ell} \equiv F/(6\pi a U)$, as determined from the sphere's velocity [15]. Additionally, dimensionless scale functions may be introduced, satisfying $Q = a^2 f(\xi_d/a)F$ and $m = -(a^2/\eta_{\ell})g(\xi_d/a)F$, such that both $f(x)$ and $g(x)$ interpolate between values ~ 1 for $x \ll 1$ and $\sim x^2$ for $x \gg 1$.

We demonstrate the validity of these predictions in the two-fluid model of a dilute polymer gel [8,11,12]. In this model, an incompressible viscous fluid with velocity field $\mathbf{v}(\mathbf{r}, t)$, pressure field $p(\mathbf{r}, t)$, and viscosity η , is coupled to a dilute elastic (or viscoelastic) network with displacement field $\mathbf{u}(\mathbf{r}, t)$ and Lamé coefficients μ and λ via a mutual friction coefficient Γ [16]. For a point force acting on the fluid component, one obtains for the fluid-velocity response in Fourier space $[(\mathbf{r}, t) \rightarrow (\mathbf{q}, \omega)]$ [8]

$$v_{\alpha}(\mathbf{q}, \omega) = \frac{1 + (\eta_b/\eta)\xi_d^2 q^2}{\eta_b q^2 (1 + \xi_d^2 q^2)} (\delta_{\alpha\beta} - \hat{\mathbf{q}}_{\alpha}\hat{\mathbf{q}}_{\beta}) F_{\beta}, \quad (1)$$

with $\eta_b = \eta - \mu/(i\omega)$ and $\xi_d^2 = \eta\mu/[\Gamma(\mu - i\omega\eta)]$. Inverting back from \mathbf{q} to \mathbf{r} while assuming $\eta_b \gg \eta$, we get at large distances the two predicted terms, $\mathbf{v} \approx \mathbf{v}_1 + \mathbf{v}_2$, where

$$v_{1\alpha} = \frac{\delta_{\alpha\beta} + \hat{\mathbf{r}}_{\alpha}\hat{\mathbf{r}}_{\beta}}{8\pi\eta_b r} F_{\beta}, \quad v_{2\alpha} = -\frac{\xi_d^2(\delta_{\alpha\beta} - 3\hat{\mathbf{r}}_{\alpha}\hat{\mathbf{r}}_{\beta})}{4\pi\eta r^3} F_{\beta}. \quad (2)$$

These results are for the limit $a/\xi_d \rightarrow 0$, where $\eta_{\ell} \rightarrow \eta$. We have calculated also the fluid-velocity response of this model to a forced rigid sphere of finite radius a . The ξ_d^2 coefficient in Eq. (2) is then modified to $a^2 g(\xi_d/a)$ with $g(x)$ given below [17]. The dominant response becomes equal to the subdominant one at the distance

$$r_c = a[2(\eta_b/\eta_{\ell})g(\xi_d/a)]^{1/2}, \quad g(x) = x^2 + x + 1/3. \quad (3)$$

These expressions were obtained assuming $\eta_b/\eta_{\ell} \gg 1$ and an incompressible network ($\lambda \rightarrow \infty$ or Poisson ratio $\sigma = 1/2$). A large η_b/η_{ℓ} ratio is expected, e.g., for small probes in stiff polymer networks [18]. Effects of compressibility [19] are found not to change Eq. (3) appreciably for σ as low as 0.4 [17].

Let us summarize the three main characteristics of the subdominant response, expected in a complex fluid with a large η_b/η_{ℓ} contrast: (a) a positive r^{-3} decay of the longitudinal response; (b) a negative transverse response; (c) a crossover to the asymptotic response at a distance much larger than the correlation length [20].

We use thermally equilibrated, homogeneous samples of entangled F-actin networks, whose rheology has been thoroughly characterized in recent years [6,21–24]. It is well established that 1P microrheology underestimates the bulk viscoelastic moduli of these networks, whereas a more accurate measurement is obtained by 2P microrheology [6,22–24]. The large contrast between the bulk and local moduli makes these networks a good model system for checking the aforementioned predictions. F-actin networks have the additional benefit of an easy control over the network's mesh size, $\xi_s = 0.3/\sqrt{c_A}$, determined by the monomer concentration c_A (c_A in mg/ml and ξ_s in μm) [25].

Entangled F-actin networks were polymerized from purified monomer G-actin in the presence of passivated polystyrene colloidal particles of radii $a = 0.245$ and $0.55 \mu\text{m}$ (Invitrogen) [26]. We set the average filament length to be $\approx 13 \mu\text{m}$ by addition of capping protein. The actin concentrations were $c_A = 0.46$ – 2 mg/ml, corresponding to $\xi_s = 0.44$ – $0.21 \mu\text{m}$, respectively. Immediately after polymerization the sample was loaded into a glass cell, previously coated with methoxy-terminated polyethylene glycol to prevent binding of the network to the glass [26]. After equilibration for 30 min at room temperature, samples were fluorescently imaged at $\lambda = 605$ nm. Tracer particle

motion from approximately 8×10^5 frames per sample was recorded at a frame rate of 70 Hz and tracked with accuracy of at least 13 nm [27].

We start by characterizing the viscoelastic properties of the F-actin networks using conventional 1P and 2P microrheology. In 1P microrheology, one measures the ensemble-averaged mean-squared displacement (MSD) of individual tracer particles along any axis x as a function of lag time τ , $\text{MSD}^{1\text{P}}(\tau) \equiv \langle \Delta x^2(\tau) \rangle$, and extracts from it the viscoelastic moduli, $G'(\omega)$ and $G''(\omega)$, using the GSER [3,7,28]. In 2P microrheology, one measures the ensemble-averaged longitudinal (parallel to \mathbf{r}) and transverse (perpendicular to \mathbf{r}) displacement correlations of particle pairs as functions of interparticle distance r and lag time τ , $D_{\parallel}(r, \tau)$, $D_{\perp}(r, \tau)$ [6]. At sufficiently large distances, both correlations decay as r^{-1} , $D_{\parallel} \approx A(\tau)/r$ and $D_{\perp} \approx A(\tau)/(2r)$. The common practice is to use this asymptote to define a ‘‘two-point mean-squared displacement,’’ $\text{MSD}^{2\text{P}}(\tau) \equiv 2A(\tau)/(3a)$ [29], and extract from it the viscoelastic moduli using again the GSER [6]. Figures 1(a) and 1(b) show the 1P and 2P MSD’s measured in an actin network and the moduli extracted from them. The measurements demonstrate the much softer local environment probed by the 1P technique, compared to the bulk response probed by the 2P one. These results are in quantitative agreement with previous studies on F-actin networks [6,22,23].

A closer look at the 2P longitudinal correlation reveals a positive r^{-3} decay preceding the asymptotic r^{-1} one [Fig. 1(c)]. The crossover between the two regimes appears

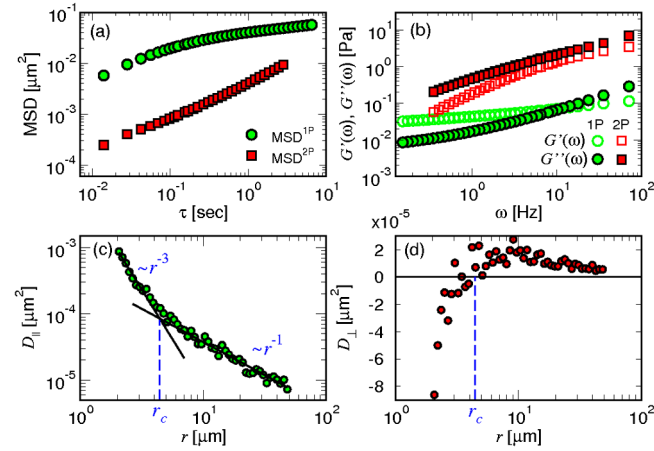


FIG. 1 (color online). Microrheology of entangled F-actin networks. (a) $\text{MSD}^{1\text{P}}$ (green) and $\text{MSD}^{2\text{P}}$ (red) as a function of lag time, for $\xi_s = 0.3 \mu\text{m}$ and $a = 0.245 \mu\text{m}$. (b) The storage modulus $G'(\omega)$ (open symbols) and loss modulus $G''(\omega)$ (filled symbols), extracted from the $\text{MSD}^{1\text{P}}$ (green) and $\text{MSD}^{2\text{P}}$ (red) curves of panel (a). (c) Longitudinal and (d) transverse displacement correlations as a function of particle separation at lag time $\tau = 0.014$ s for $\xi_s = 0.44 \mu\text{m}$ and $a = 0.55 \mu\text{m}$. The crossover distance r_c (blue dashed line) is defined at the intersection of the fitted dominant (r^{-1}) and subdominant (r^{-3}) power-law decays of D_{\parallel} .

at a distance $r_c = 4.4 \mu\text{m}$, an order of magnitude larger than the network mesh size ξ_s . For $r < r_c$ the transverse correlation is found to be negative [Fig. 1(d)]. Thus, the three qualitative features mentioned above for the intermediate response are verified.

Now, we extend the formalism of microrheology to include the response at intermediate distances. This has two goals: (a) to validate in more detail the theoretical predictions; (b) to provide a quantitative analysis to be used in future studies of other complex fluids. We focus on the longitudinal displacement correlation, $D_{\parallel}(r, \tau)$, which is stronger than the transverse one, and apply it in the time (rather than frequency) domain to minimize data manipulation.

The correlation can be well fitted over both large and intermediate distances by

$$D_{\parallel}(r, \tau) = A(\tau)/r + B(\tau)/r^3. \quad (4)$$

There are three directly measured quantities: $\text{MSD}^{1\text{P}}(\tau)$; $A(\tau)$ or, equivalently, $\text{MSD}^{2\text{P}}(\tau)$; and $B(\tau)$. We need to relate them to the frequency-dependent coefficients appearing in Eq. (2). At sufficiently large distances, $r \gg a$, the 2P coupling mobility coincides with the fluid velocity response at a distance \mathbf{r} away from an applied unit force. Using Eq. (2), we get, for the longitudinal part of that mobility, $M_{\parallel}(r, \omega) = (4\pi\eta_b r)^{-1} + a^2 g(\xi_d/a)(2\pi\eta_\ell r^3)^{-1}$. From the fluctuation-dissipation theorem $D_{\parallel}(r, \omega) = -(2k_B T/\omega^2)M_{\parallel}(r, \omega)$, where $k_B T$ is the thermal energy. Comparing this with Eq. (4), we identify

$$A(\tau) = [k_B T/(2\pi)]\mathcal{F}^{-1}\{(-\omega^2\eta_b)^{-1}\}, \quad (5)$$

$$B(\tau) = (k_B T/\pi)a^2 g(\xi_d/a)\mathcal{F}^{-1}\{(-\omega^2\eta_\ell)^{-1}\}, \quad (6)$$

where \mathcal{F}^{-1} denotes the inverse Fourier transform.

Equation (5) merely restates the basic relation used in standard 2P microrheology to measure the bulk viscoelastic moduli. Equation (6) represents our extension. Its left-hand side is a directly measurable coefficient, $B(\tau)$, while its right-hand side depends on two dynamic characteristics of the fluid, η_ℓ and ξ_d . The local response is obtainable from the 1P measurement. According to the GSER, $\text{MSD}^{1\text{P}}(\tau) = [k_B T/(3\pi a)]\mathcal{F}^{-1}\{(-\omega^2\eta_\ell)^{-1}\}$ [29]. Substitution in Eq. (6) yields a relation separating the time-dependent observables $\text{MSD}^{1\text{P}}(\tau)$ and $B(\tau)$ from the structural features to be characterized, $B(\tau)/\text{MSD}^{1\text{P}}(\tau) = 3a^3 g(\xi_d/a)$. Equivalently, we may examine the crossover distance

$$r_c(\tau) = [B(\tau)/A(\tau)]^{1/2} = a[2g(\xi_d/a)]^{1/2}[H(\tau)]^{1/2}, \quad (7)$$

$$H(\tau) \equiv \text{MSD}^{1\text{P}}(\tau)/\text{MSD}^{2\text{P}}(\tau),$$

where the structural part is again decoupled from a measurable time-dependent function, $H(\tau)$, characterizing the ratio between the bulk and local responses. In Fig. 2(a), the experimentally measured r_c is plotted as a function of lag

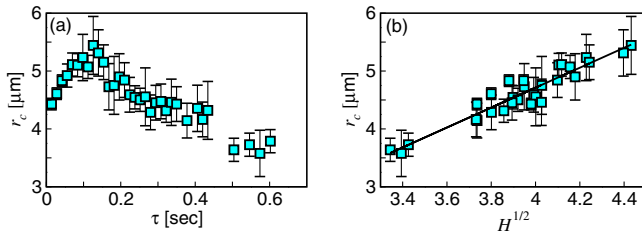


FIG. 2 (color online). Crossover distance as a function of (a) lag time, and (b) square root of $H(\tau)$, the experimental function characterizing the bulk to local viscosity ratio. Parameter values are $a = 0.55 \mu\text{m}$, $\xi_s = 0.44 \mu\text{m}$.

time, exhibiting a nonmonotonic dependence. Yet, by replotting r_c against $[H(\tau)]^{1/2}$, Fig. 2(b), the linear dependence predicted by Eq. (7) is verified. We repeated the analysis for a set of actin networks of different concentrations (i.e., different mesh sizes) and for two different bead sizes. Since the static and dynamic correlation lengths, ξ_s and ξ_d , should be comparable [11], and ξ_s and a are comparable in our experiment, the results should be sensitive to the interpolation function $g(\xi_d/a)$ defined in Eq. (3). In Fig. 3(a), r_c for all the experiments is plotted as a function of $H^{1/2}$. All curves are linear, as predicted, and fall into two clusters (open and filled symbols) corresponding to the two particle sizes. Differentiation of Eq. (3) shows that r_c should increase with either ξ_s or a at constant H , which is confirmed in Fig. 3(a). For a more quantitative validation, we rescale all the measurements according to the scheme suggested by Eq. (7) and obtain convincing data collapse [Fig. 3(b)]. Furthermore, the resulting master curve fits well the theoretical scale function of Eq. (3) using a single free parameter—a constant ratio of order unity between the static and dynamic lengths, $\xi_d = b\xi_s$, with $b \approx 1.2$ – 1.3 .

One of the new insights in the current Letter is that the local viscoelastic properties of the medium affect its response over length scales much larger than the correlation length and probe size. Moreover, there are scenarios in

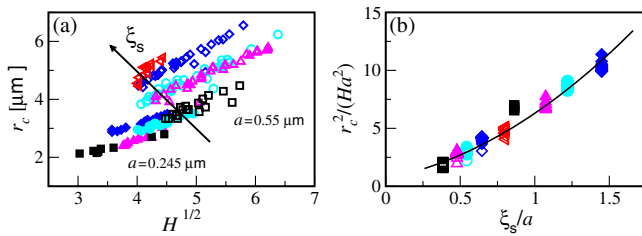


FIG. 3 (color online). Crossover distance for all experiments. (a) For all conditions, r_c is linear with $H^{1/2}$ and increases with either ξ_s or a . (b) All experimental results fall on a master curve once r_c^2 is normalized by Ha^2 and presented as a function of ξ_s/a . The solid line is a fit to Eq. (7) with the scale function given by Eq. (3) and $\xi_d = 1.25\xi_s$. Open (filled) symbols correspond to $a = 0.55(0.245) \mu\text{m}$. Each color and symbol corresponds to a different mesh size: $\xi_s = 0.21$ (black squares), 0.26 (magenta triangles), 0.3 (cyan circles), 0.35 (blue diamonds), and $0.44 \mu\text{m}$ (red left triangles).

which the dominant momentum term in the complex-fluid response is suppressed, leaving the subdominant mass term as the sole correlation mechanism at large distances. We mention three examples. (a) For a very stiff matrix, as in the case of a fluid embedded in a solid porous medium, the crossover to the asymptotic term will be pushed to arbitrarily large distances. (b) In a thin film of gel supported on a rigid substrate, the momentum term will be suppressed at distances larger than the film thickness, whereas the mass term will be enhanced by such confinement. This qualitatively accounts for the dipolar shape of the 2P response previously reported for such a system [30]. (c) At sufficiently short time (high frequency), the diffusive momentum term is cut off beyond a certain distance (viscous penetration depth), whereas the mass disturbance, propagating via much faster compression modes, is not. All three scenarios obviously require further quantitative investigation.

Another intrinsic length scale affecting the dynamics of actin networks is the filament length [23]. Its value in the current Letter ($13 \mu\text{m}$) is much larger than ξ_s and a . For shorter filament lengths, there are subtle effects related to the local environment of the probe [17,23]. Additional length scales, not present in the current system, can arise from sample heterogeneity [31].

Extracting spatiotemporal characteristics such as the dynamic correlation length can be achieved, for example, by various dynamic scattering techniques [2]. The intermediate response itself, however, despite its significant effect demonstrated here, is averaged out in such scattering measurements by virtue of the spatial symmetry of the corresponding dipolar term.

The analysis presented here, clearly, is not restricted to actin networks. It is applicable to any complex fluid with a sufficiently large η_b/η_ℓ contrast [18]. (As “local” refers to the scale of the probe, the contrast can be enhanced by reducing the probe size down to $a \ll \xi_d$, whereupon the local response becomes that of the molecular solvent.) In particular, our findings show that bulk viscoelasticity inadequately describes micron scale stiff biopolymer gels such as the cellular cortical network.

We thank Rony Granek, Fred MacKintosh, and Tom Witten for helpful discussions. This research has been supported by the Israel Science Foundation (Grants No. 1271/08 and No. 8/10) and the Marie Curie Reintegration Grant (No. PIRG04-GA-2008-239378). A. S.-S. acknowledges funding from the Tel-Aviv University Center for Nanoscience and Nanotechnology.

* roichman@tau.ac.il

- [1] T. A. Witten, *Structured Fluids* (Oxford University Press, New York, 2004).
- [2] R. G. Larson, *The Structure and Rheology of Complex Fluids* (Oxford University Press, New York, 1999).
- [3] T. G. Mason and D. A. Weitz, *Phys. Rev. Lett.* **74**, 1250 (1995).

- [4] T. G. Mason, K. Ganesan, J. H. van Zanten, D. Wirtz, and S. C. Kuo, *Phys. Rev. Lett.* **79**, 3282 (1997).
- [5] F. Gittes, B. Schnurr, P. D. Olmsted, F. C. MacKintosh, and C. F. Schmidt, *Phys. Rev. Lett.* **79**, 3286 (1997); *Macromolecules* **30**, 7781 (1997).
- [6] J. C. Crocker, M. T. Valentine, E. R. Weeks, T. Gisler, P. D. Kaplan, A. G. Yodh, and D. A. Weitz, *Phys. Rev. Lett.* **85**, 888 (2000).
- [7] T. M. Squires and T. G. Mason, *Annu. Rev. Fluid Mech.* **42**, 413, (2010).
- [8] A. J. Levine and T. C. Lubensky, *Phys. Rev. Lett.* **85**, 1774 (2000); *Phys. Rev. E* **63**, 041510 (2001).
- [9] D. T. Chen, E. R. Weeks, J. C. Crocker, M. F. Islam, R. Verma, J. Gruber, A. J. Levine, T. C. Lubensky, and A. G. Yodh, *Phys. Rev. Lett.* **90**, 108301 (2003).
- [10] L. Starrs and P. Bartlett, *Faraday Discuss.* **123**, 323 (2003).
- [11] P.-G. de Gennes, *Macromolecules* **9**, 587 (1976); **9**, 594 (1976).
- [12] S. T. Milner, *Phys. Rev. E* **48**, 3674 (1993).
- [13] J. Happel and H. Brenner, *Low Reynolds Number Hydrodynamics* (Martinus Nijhoff, The Hague, 1983).
- [14] We generalize an argument first presented in H. Diamant, *Isr. J. Chem.* **47**, 225 (2007).
- [15] The local viscosity is a function of ξ_d/a , with $\eta_\ell(\xi_d/a \rightarrow \infty) \rightarrow \eta$ and $\eta_\ell(\xi_d/a \rightarrow 0) \rightarrow \eta_b$. Here we bypass this dependence by extracting η_ℓ from 1P measurements.
- [16] For simplicity, we neglect inertial effects, which set in at high frequency and can be readily added if needed [8].
- [17] Details will be given elsewhere; see also Supplemental Material [26] for a commented Mathematica© file.
- [18] V. Pelletier, N. Gal, P. Fournier, and M. L. Kilfoil, *Phys. Rev. Lett.* **102**, 188303 (2009).
- [19] F. C. MacKintosh and A. J. Levine, *Phys. Rev. Lett.* **100**, 018104 (2008); F. C. MacKintosh and A. J. Levine, *J. Phys. Chem. B* **113**, 3820 (2009).
- [20] Properties (a) and (c) have been qualitatively reported for microtubule networks [18].
- [21] A. Palmer, T. G. Mason, J. Y. Xu, S. C. Kuo, and D. Wirtz, *Biophys. J.* **76**, 1063 (1999).
- [22] M. L. Gardel, M. T. Valentine, J. C. Crocker, A. R. Bausch, and D. A. Weitz, *Phys. Rev. Lett.* **91**, 158302 (2003); J. H. Shin, M. L. Gardel, L. Mahadevan, P. Matsudaira, and D. A. Weitz, *Proc. Natl. Acad. Sci. U. S. A.* **101**, 9636 (2004).
- [23] J. Liu, M. L. Gardel, K. Kroy, E. Frey, B. D. Hoffman, J. C. Crocker, A. R. Bausch, and D. A. Weitz, *Phys. Rev. Lett.* **96**, 118104 (2006).
- [24] M. Atakhorrami, G. H. Koenderink, J. F. Paliarne, F. C. MacKintosh, and C. F. Schmidt, arXiv:1210.8404 [*Phys. Rev. Lett.* (in preparation)].
- [25] C. F. Schmidt, M. Barmann, G. Isenberg, and E. Sackmann, *Macromolecules* **22**, 3638 (1989).
- [26] See Supplemental Material at <http://link.aps.org/supplemental/10.1103/PhysRevLett.112.088301> for sample preparation details.
- [27] J. C. Crocker and D. G. Grier, *J. Colloid Interface Sci.* **179**, 298 (1996).
- [28] J. C. Crocker and B. D. Hoffman, *Methods Cell Biol.* **83**, 141 (2007).
- [29] We use the one-dimensional forms of the MSD's.
- [30] G. Ladam, L. Vonna, and E. Sackmann, *J. Phys. Chem. B* **107**, 8965 (2003).
- [31] S. Jabbari-Farouji, M. Atakhorrami, D. Mizuno, E. Eiser, G. H. Wegdam, F. C. MacKintosh, D. Bonn, and C. F. Schmidt, *Phys. Rev. E* **78**, 061402 (2008).

Material preparation

G-actin was purified from rabbit skeletal muscle acetone powder [1], with a gel filtration step, stored on ice in G-buffer (5 mM Tris HCl, 0.1 mM CaCl₂, 0.2 mM ATP, 1 mM DTT, 0.01% NaN₃, pH 7.8) and used within two weeks. The concentration of the G-actin was determined by absorbance, using a UV/Visible spectrophotometer (Ultraspec 2100 pro, Pharmacia) in a cuvette with a 1 cm path length and extinction coefficient of $\epsilon_{290} = 26,460 \text{ M}^{-1}\text{cm}^{-1}$. Polystyrene colloids with radii of $a = 0.245, 0.55 \mu\text{m}$ (Invitrogen, lots #1173396 and #742530, respectively) were pre-incubated with a 10 mg/ml BSA (bovine serum albumin, Sigma) solution to prevent nonspecific binding of protein to the bead surface [2]. We controlled the average filament length by addition of capping protein to obtain an estimated average length of 13 μm . Actin polymerization was initiated by adding G-actin in various concentrations, capping protein, and colloidal particles to F-buffer solution (5 mM Tris HCl, 1 mM MgCl₂, 0.05 M KCl, 200 μM EGTA,

1 mM Mg-ATP) and mixing gently for 10 s. The actin concentrations were $c_A = 0.46\text{--}2 \text{ mg/ml}$, corresponding to $\xi_s = 0.44\text{--}0.21 \mu\text{m}$, respectively.

Sample preparation

Glass samples were prepared from glass coverslips (diameter, 40mm) coated with methoxy-terminated PEG (Polyethylene glycol, $M_w=5000 \text{ g/mol}$, Nanocs) to prevent F-actin filaments from sticking to the chamber walls. Immediately after polymerization the sample was loaded into a glass cell and left to equilibrate for 30 min at room temperature.

-
- [1] J. A. Spudich and S. Watt, J. Biol. Chem. **246**, 4866 (1971).
 [2] M. T. Valentine, Z. E. Perlman, M. L. Gardel, J. H. Shin, P. Matsudaira, T. J. Mitchison, and D. A. Weitz, Biophys. J. **86**, 4004 (2004).

Cite this: *Soft Matter*, 2014, 10, 8324

Extracting the dynamic correlation length of actin networks from microrheology experiments

Adar Sonn-Segev,^a Anne Bernheim-Groswasser^b and Yael Roichman^{*a}

The mechanical properties of polymer gels based on cytoskeleton proteins (e.g. actin) have been studied extensively due to their significant role in biological cell motility and in maintaining the cell's structural integrity. Microrheology is the natural method of choice for such studies due to its economy in sample volume, its wide frequency range, and its spatial sensitivity. In microrheology, the thermal motion of tracer particles embedded in a complex fluid is used to extract the fluid's viscoelastic properties. Comparing the motion of a single particle to the correlated motion of particle pairs, it is possible to extract viscoelastic properties at different length scales. In a recent study, a crossover between intermediate and bulk response of complex fluids was discovered in microrheology measurements of reconstituted actin networks. This crossover length was related to structural and mechanical properties of the networks, such as their mesh size and dynamic correlation length. Here we capitalize on this result giving a detailed description of our analysis scheme, and demonstrating how this relation can be used to extract the dynamic correlation length of a polymer network. We further study the relation between the dynamic correlation length and the structure of the network, by introducing a new length scale, the average filament length, without altering the network's mesh size. Contrary to the prevailing assumption, that the dynamic correlation length is equivalent to the mesh size of the network, we find that the dynamic correlation length increases once the filament length is reduced below the crossover distance.

Received 13th July 2014
Accepted 26th August 2014

DOI: 10.1039/c4sm01538j

www.rsc.org/softmatter

1. Introduction

Complex fluids are intriguing materials, both from the structural and the mechanical point of view. Comprised of at least two components, these fluids contain mesoscopic structural features on the scale of nanometers to millimeters.¹ As a result their mechanical response to perturbations is both elastic-like and fluid-like in nature. Conventionally, complex fluids are characterized mechanically by bulk rheology.² Complex fluids of biological origin, which are not readily available in large quantities, are usually characterized using a more material economic technique, microrheology, which uses the motion of embedded tracer particles observed by optical microscopy to extract the material properties.^{3–9} Another advantage of microrheology is its ability to characterize the viscoelastic properties of these fluids on different length scales.^{10–12} Utilizing this trait of microrheology, we recently showed that the mechanical properties of an example complex fluid (actin networks) change from bulk to intermediate behavior below a characteristic crossover length (r_c).¹³ This new length scale depends both on

structural features of the material as well as on its local and bulk viscoelastic properties. The crossover length, r_c , can be related to the dynamical correlation length, ξ_d , of the complex fluid. For polymer networks, ξ_d , which is the length scale over which dynamical correlations decay in the network, is considered to be related to the mesh size,^{14,15} and is commonly measured by dynamic light scattering, requiring large sample volumes. Measuring ξ_d with microrheology offers a means to connect mechanical properties of a polymer networks to their structure using microscopic quantities.

Polymer networks made of cytoskeleton proteins have been thoroughly studied in an effort to understand their biological role in the cell.^{16–24} The most researched of which is actin, which is the focus of this paper. We study the spatial dependence of the viscoelastic properties of thermally equilibrated F-actin networks, and their relation to the networks' structure. We start by outlining our generalized analysis scheme of microrheology experiments and its application to reconstituted actin networks of different mesh size. We then demonstrate how to extract the viscoelastic and structural properties of the networks, regardless of tracer particle size (*i.e.*, its size relative to the mesh size). We proceed to explore the dynamical correlation length's relation to the networks' mesh size, and investigate how ξ_d is affected by the introduction of another relevant length scale, the average filament length $\langle l \rangle$. Finally, we examine the relation

^aRaymond & Beverly Sackler School of Chemistry, Tel Aviv University, Tel Aviv 6997801, Israel. E-mail: roichman@tau.ac.il

^bDepartment of Chemical Engineering, Ilse Kats Institute for Nanoscale Science and Technology, Ben Gurion University of the Negev, Beer-Sheva 84105, Israel

between the viscoelastic plateau modulus and the dynamic correlation length of the gels.

2. Experimental

We use entangled F-actin networks as a model viscoelastic fluid. The rheological properties of this system have been studied extensively both experimentally and theoretically.^{7,9,12,25–28} F-actin gels are well described as networks of semiflexible polymers, and their mesh size, $\xi_s = 0.3/\sqrt{c_A}$, is easily controlled through monomer concentration c_A (c_A in mg ml^{-1} and ξ_s in μm (ref. 29)).

G-actin is purified from rabbit skeletal muscle acetone powder,³⁰ with a gel filtration step, stored on ice in G-buffer (5 mM Tris HCl, 0.1 mM CaCl_2 , 0.2 mM ATP, 1 mM DTT, 0.01% NaN_3 , pH 7.8) and used within two weeks. The concentration of the G-actin is determined by absorbance measured using UV/visible spectrophotometer (Ultraspec 2100 pro, Pharmacia) in a cuvette with a 1 cm path length and extinction coefficient $\epsilon_{290} = 26\,460\text{ M}^{-1}\text{ cm}^{-1}$. Polystyrene colloids with diameters of $a = 0.245, 0.55\ \mu\text{m}$ (Invitrogen Lots #1173396 and #742530 respectively) are pre-incubated with a $10\ \text{mg ml}^{-1}$ BSA solution to prevent non specific binding of protein to the bead surface.³¹ The average filament length, $\langle l \rangle$, is controlled by addition of capping protein (CP). Actin polymerization is initiated by adding G-actin in various concentrations, CP and beads to F-buffer solution (5 mM Tris HCl, 2 mM MgCl_2 , 0.05 M KCl, 200 μM EGTA, 1 mM ATP) and mixing gently for 10 s. Mesh size is varied by changing G-actin concentration between $c_A = 0.46\text{--}2\ \text{mg ml}^{-1}$, corresponding to $\xi_s = 0.44\text{--}0.21\ \mu\text{m}$ (at fixed $\langle l \rangle = 13\ \mu\text{m}$). The average filament length is varied, at constant actin concentration ($\xi_s = 0.3\ \mu\text{m}$), by changing the concentration ratio of actin–CP. Filament length distribution is roughly exponential.³² We estimate $\langle l \rangle = 2\text{--}13\ \mu\text{m}$ assuming CP determines the number of actin nucleation sites.^{12,32,33}

Immediately after polymerization the samples were loaded into a glass cell, 150 μm high, and sealed with grease. The glass surfaces were coated with methoxy-terminated PEG to prevent binding of the network to the glass. After equilibrating for 30 min at room temperature, samples were imaged at a plane distanced from the cell walls with an epi-fluorescence microscope (Olympus IX71), at $\lambda = 605\ \text{nm}$, with $60\times$ oil, and $40\times$ air objectives for $a = 0.245\ \mu\text{m}$ and $a = 0.55\ \mu\text{m}$, respectively. We recorded the motion of approximately 100 particles in the field of view using a CMOS video camera (Gazelle, Point Gray) at a frame rate of 70 Hz with an exposure time of 0.003 s. To insure high signal to noise ratio of two-particle displacement correlation measurements, we used data from approximately 8×10^5 frames per experiment. Particle tracking was done using conventional algorithms with accuracy of at least 13 nm.³⁴

3. Generalized microrheology and the dynamic correlation length

3.1 Microrheology at intermediate length scales

Conventional microrheology is concerned with characterizing the mechanical properties of a complex fluid by analyzing the

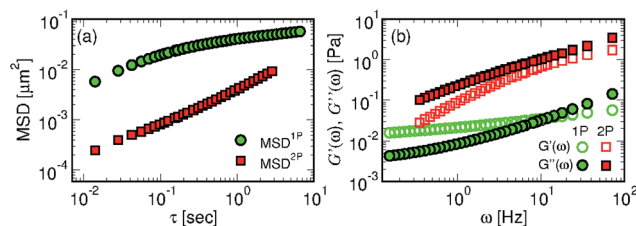


Fig. 1 Microrheology of entangled F-actin networks. (a) $\text{MSD}^{1\text{P}}$ (green) and $\text{MSD}^{2\text{P}}$ (red) as a function of lag time, for $\xi_s = 0.3\ \mu\text{m}$, $a = 0.245\ \mu\text{m}$ and $\langle l \rangle = 13\ \mu\text{m}$. (b) The storage modulus, $G'(\omega)$ (open symbols), and loss modulus, $G''(\omega)$ (filled symbols), extracted from the $\text{MSD}^{1\text{P}}$ (green) and $\text{MSD}^{2\text{P}}$ (red) curves of panel (a).

diffusion of tracer particles embedded in it.^{3–9} We concentrate on the passive variants of the technique⁸ relating the thermal fluctuations of the tracer particles to the viscoelastic properties of the characterized fluid, using both one point (1P) and two point (2P) microrheology. In 1P microrheology the generalized Stokes Einstein relation (GSER) is used to connect the ensemble averaged mean-squared displacement of tracer particles, $\text{MSD}^{1\text{P}} \equiv \langle \Delta x^2(\tau) \rangle$ (Fig. 1(a)) to the viscoelastic moduli, $G'(\omega)$ and $G''(\omega)$ (Fig. 1(b)).^{3,8,35}

This technique probes only the local environment of the tracer particle, which is the microscopic volume explored by the particle within the experimental time scale. Consequently, it is well established that 1P microrheology of actin networks underestimates the bulk viscoelastic moduli.^{7,12,26–28} 2P microrheology was developed to address this issue, by looking at the average correlated diffusion of two distanced particles. Specifically, one measures the ensemble-averaged longitudinal and transverse displacement correlations of particle pairs as a function of inter-particle distance r and lag time τ :⁷

$$\begin{aligned} D_{\parallel}(r, \tau) &= \langle \Delta r_{\parallel}^i(t, \tau) \Delta r_{\parallel}^j(t, \tau) \delta(r - R^j(t)) \rangle \\ D_{\perp}(r, \tau) &= \langle \Delta r_{\perp}^i(t, \tau) \Delta r_{\perp}^j(t, \tau) \delta(r - R^j(t)) \rangle, \end{aligned} \quad (1)$$

where $\Delta r_{\parallel}^i(t, \tau)$ ($\Delta r_{\perp}^i(t, \tau)$) is the displacement of particle i during the time between t and $t + \tau$, projected parallel (perpendicular) to the line connecting the pair, and $R^j(t)$ is the pair separation at time t . At sufficiently large distances both correlations decay as r^{-1} , $D_{\parallel} \approx A(\tau)/r$ and $D_{\perp} \approx A(\tau)/(2r)$. The common practice is to use this asymptote to define a ‘two-point mean-squared displacement’, $\text{MSD}^{2\text{P}}(\tau) \equiv 2A(\tau)/(3a)$,[†] and extract from it the viscoelastic moduli using again the GSER.⁷

Fig. 1(a) and (b) show the 1P and 2P MSD’s measured in an actin network ($\xi_s = 0.3\ \mu\text{m}$), and the moduli extracted from them. The viscoelastic properties obtained from the two approaches are significantly different, demonstrating the much softer local environment probed by the 1P technique, as compared to the bulk response probed by the 2P one. These results are in accord, both qualitatively and quantitatively, with previous studies on F-actin networks.^{7,12,26}

We have recently shown¹³ that the inter-particle distance at which the bulk response sets in is much larger than would

[†] We use the one-dimensional forms of the MSD’s.

intuitively be expected. For example, in our experiments (Fig. 2(a) and (b)) a crossover to an intermediate regime is observed at $r_c = 3.5 \mu\text{m}$, which is an order of magnitude larger than the network mesh size, $\xi_s = 0.3 \mu\text{m}$, and the tracer particle's radius, $a = 0.245 \mu\text{m}$. The detailed theoretical description of the viscoelastic behavior of complex fluids at intermediate length scales, below r_c , is given elsewhere.^{13,36} Simply stated, a particle moving within a fluid disturbs it in two ways: it generates a momentum perturbation that spreads in the bulk, and displaces mass locally.³⁷ These two contributions can be expanded in terms of inter-particle distance and depend on the bulk and local viscosity respectively. For complex fluids in which the local environment is much softer than the bulk, the leading terms in the mobility expansion are:^{13,36}

$$M_{\parallel}(r, \omega) = \frac{1}{4\pi\eta_b r} + \frac{a^2 g(\xi_d/a)}{2\pi\eta_l r^3} \quad (2)$$

$$M_{\perp}(r, \omega) = \frac{1}{8\pi\eta_b r} - \frac{a^2 g(\xi_d/a)}{4\pi\eta_l r^3}, \quad (3)$$

where η_b (η_l) corresponds to the bulk (local) viscosity and the function $g(\xi_d/a)$ arises from calculating the fluid response to a forced rigid sphere of finite radius a . The first term, the dominant response, arises from momentum conservation, while the second term, the sub-dominant response, describes mass transfer. At intermediate distances ($r \leq r_c$) the viscoelastic properties of a complex fluid are governed by the subdominant term.^{13,36} Eqn (2) and (3) imply that the intermediate response should decay as $1/r^3$ in the longitudinal direction, and exhibit negative correlation in the transverse one. As a result the crossover between the asymptotic, dominant response in the longitudinal direction to the intermediate, subdominant one should appear at a distance:

$$r_c = a[2(\eta_b/\eta_l)g(\xi_d/a)]^{1/2} \quad (4)$$

where $g(x)$ is a material specific function that satisfies the asymptotic conditions:^{13,36} $g(x \rightarrow \infty) = x^2$, and $g(x \rightarrow 0) = 1$.

The displacement correlation, D_{\parallel} , can be related to the mobility M_{\parallel} , using the fluctuation–dissipation theorem:

$$D_{\parallel}(r, \omega) = -(2k_B T/\omega^2)M_{\parallel}(r, \omega) \quad (5)$$

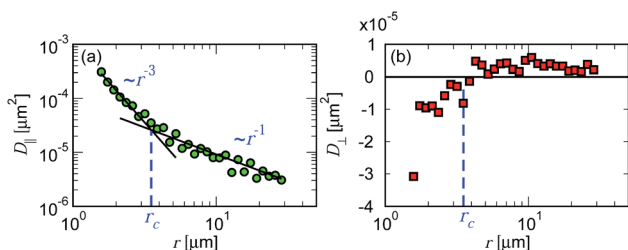


Fig. 2 (a) Longitudinal and (b) transverse displacement correlations as a function of particle separation, r , at lag time $\tau = 0.014 \text{ s}$ for $\xi_s = 0.3 \mu\text{m}$, $a = 0.245 \mu\text{m}$ and $\langle l \rangle = 13 \mu\text{m}$. The crossover distance r_c (blue dashed line) is defined at the intersection of the fitted dominant (r^{-1}) and subdominant (r^{-3}) power-law decays of D_{\parallel} .

where $k_B T$ is the thermal energy. To minimize data manipulation the analysis is applied on the time (rather than frequency) domain and thus the expected expression for $D_{\parallel}(r, \tau)$ is:

$$D_{\parallel}(r, \tau) = \frac{A(\tau)}{r} + \frac{B(\tau)}{r^3} \quad (6)$$

where

$$A(\tau) = \frac{k_B T}{2\pi} \mathcal{F}^{-1} \left\{ \frac{1}{-\omega^2 \eta_b} \right\} \quad (7)$$

$$B(\tau) = \frac{k_B T}{\pi} a^2 g(\xi_d/a) \mathcal{F}^{-1} \left\{ \frac{1}{-\omega^2 \eta_l} \right\} \quad (8)$$

where \mathcal{F}^{-1} denotes the inverse Fourier transform. The crossover distance in the time domain is then given by:

$$r_c(\tau) = [B(\tau)/A(\tau)]^{1/2}. \quad (9)$$

3.2 Dynamic correlation length measurement

One outcome of the preceding theory is that the dynamic correlation length of a complex fluid can be extracted from microrheology experiments, provided that: (1) the functional form of $g(x)$ is known, (2) the crossover distance (eqn (9)) is experimentally observed, and (3) the bulk and local viscosity are measured. We start our analysis by expressing $A(\tau)$ and $B(\tau)$ in terms of MSD^{2P} and MSD^{1P} respectively.

$$\begin{aligned} A(\tau) &= 3a\text{MSD}^{2P}/2 \\ B(\tau) &= 3a^3 g(\xi_d/a)\text{MSD}^{1P}. \end{aligned} \quad (10)$$

To this end we assume that the local viscosity is a function of time and is related to the MSD^{1P} by the fluctuation–dissipation theorem $\text{MSD}^{1P}(\tau) = [k_B T/(3\pi a)] \mathcal{F}^{-1}\{(-\omega^2 \eta_l)^{-1}\}$. The bulk viscosity is related to the MSD^{2P} in a similar manner, and is given by $A(\tau)$ (eqn (7)).

Substituting these expressions into eqn (9) we have,

$$r_c = \left[2a^2 g\left(\frac{\xi_d}{a}\right) \frac{\text{MSD}^{1P}}{\text{MSD}^{2P}} \right]^{1/2} = \left[2a^2 g\left(\frac{\xi_d}{a}\right) H(\tau) \right]^{1/2} \quad (11)$$

where we define:

$$H(\tau) \equiv \frac{\text{MSD}^{1P}}{\text{MSD}^{2P}} \quad (12)$$

as the time dependent observable, and $g(\xi_d/a)$ the structural element to be characterized. The functional form of $g(x)$ for actin networks was derived using the two-fluid model of polymer gels,^{9,14,15,38–40} and reads;^{13,36}

$$g(x) = x^2 + x + 1/3. \quad (13)$$

Recasting $r_c(\tau)$ as a function of $\sqrt{H(\tau)}$ reveals their linear dependence (Fig. 3(b)), as predicted theoretically in eqn (11). This linear dependence holds for all our experiments, independent of tracer particle size and network mesh size (see Fig. 4(a)). Rescaling r_c^2 by Ha^2 and presenting it as a function of ξ_s/a results in a collapse of our data on a single master curve

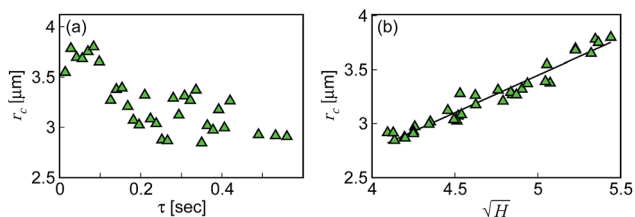


Fig. 3 Crossover distance as a function of (a) lag time, and (b) square root of $H(\tau)$, the experimental function characterizing the bulk to local viscosity ratio. Parameter values are the same as in Fig. 1; $a = 0.245 \mu\text{m}$, $\xi_s = 0.3 \mu\text{m}$ and $\langle l \rangle = 13 \mu\text{m}$.

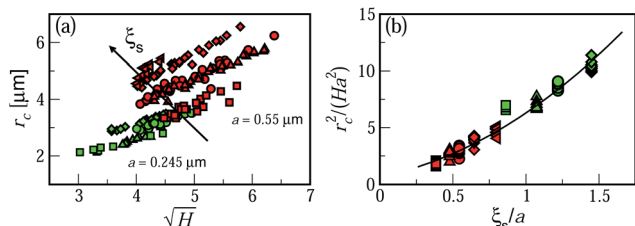


Fig. 4 Crossover distance for all experiments. (a) For all conditions r_c is linear with \sqrt{H} and increases with either ξ_s or a . (b) All experimental results fall on a master curve once r_c^2 is normalized by Ha^2 and presented as a function of scale function given by eqn (13) and $\xi_d = 1.25\xi_s$. Red (green) symbols correspond to $a = 0.55$ (0.245) μm . Each symbol corresponds to a different mesh size: $\xi_s = 0.21$ (squares), 0.26 (triangles), 0.3 (circles), 0.35 (diamonds), and $0.44 \mu\text{m}$ (left triangles). The average filament length for all experiments was $\langle l \rangle = 13 \mu\text{m}$.

shaped according to eqn (13) (see Fig. 4(b)).¹³ The only fitting parameter used to fit our data to eqn (13), was the ratio $b \equiv \xi_d/\xi_s = 1.25$. This result provides an experimental verification of the scaling function $g(\xi_d/a)$ derived using the two-fluid model for actin networks. Therefore providing a means to extract the dynamic correlation length from microrheology experiments.

In Fig. 5 the measured dynamic correlation length is plotted versus the networks' mesh size for two different sizes of tracer particles. Both ξ_d and ξ_s are material properties and should not

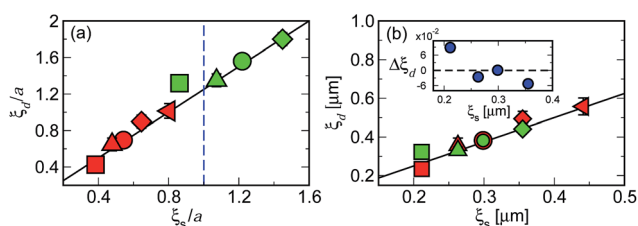


Fig. 5 Dynamic correlation length, ξ_d , extracted from r_c and H for networks with different mesh and particle sizes (see text for details). (a) ξ_d scaled by a , particle radius, as a function of the scaled mesh size ξ_s/a . (b) ξ_d as a function of ξ_s . Black line, in both figures, corresponds to $\xi_d = b\xi_s$, where $b = 1.25$ is our fitting parameter. Both $\xi_s/a > 1$ and $\xi_s/a < 1$ fall on the same line. Inset: difference between ξ_d s extracted from the two particle sizes ($\Delta\xi_d$) as a function of ξ_s . Red (green) symbols correspond to $a = 0.55$ (0.245) μm . Each symbol corresponds to a different mesh size: $\xi_s = 0.21$ (squares), 0.26 (triangles), 0.3 (circles), 0.35 (diamonds), and $\xi_s = 0.44 \mu\text{m}$ (left triangles).

depend on the tracer particle size. The difference in the dynamic correlation length measured with the two different particle sizes is used to gauge its experimental error (see Fig. 5(b)), which is of the order of $\langle \Delta\xi_d \rangle \approx 50 \text{ nm}$. The fact that the relation between ξ_d and ξ_s is linear suggests that ξ_d scales as the square root of actin concentration, as expected for semi-dilute polymer solution.

4. Effect of filament length

So far we have shown that the viscoelastic response of actin networks depends on the new emerging length scale r_c , rather than directly on the network mesh size or tracer particle size. In this section we introduce a new relevant length scale to the system, the average actin filament length, $\langle l \rangle$, which is controlled experimentally by introducing capping protein. We show that $\langle l \rangle$ affects the viscoelastic response of the networks if sufficiently decreased. We study several networks made with the same actin monomer concentration but different average filament length, $\langle l \rangle = 2, 5, 8, 10, 13 \mu\text{m}$. All of these systems create mechanically stable networks with a mesh size of $\xi_s = 0.3 \mu\text{m}$, much smaller than the average filament length. While the mesh size is conserved in these systems it is not clear if their dynamic correlation length or their mechanical properties vary.¹² Since the mesh size is the same in all of these gels and the average filament length is much larger than the mesh size, we would naively expect the crossover length in these networks to be the same as well. In Fig. 6 the crossover length scale of the different networks is examined. Surprisingly, even though the length scale depends linearly on the viscosities ratio (Fig. 6(b)) for each $\langle l \rangle$, it depends also on filament length (Fig. 6(a)).

A closer inspection of the data in Fig. 6(b) reveals that curves of different networks do not coincide, implying that the networks vary in dynamical properties. Since the functional form of $g(x)$ was calculated from the two-fluid model using a general, unspecified correlation length ξ_d , without any explicit reference to filament length, we can use it to extract ξ_d of these networks. In Fig. 7 ξ_d is plotted as a function of $\langle l \rangle$; for long filament length $\langle l \rangle > 5 \mu\text{m}$ ξ_d does not depend on filament length, as expected. However, for shorter filaments, $\langle l \rangle = 2, 5 \mu\text{m}$, ξ_d decreases with filament length. Note that the length scale below which ξ_d is affected by filament length is of the

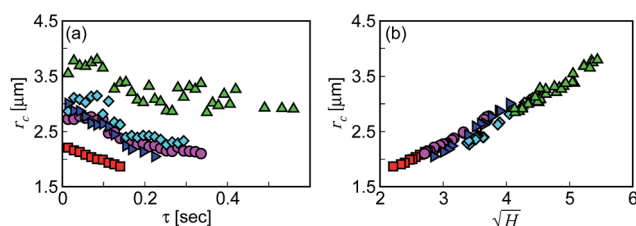


Fig. 6 Crossover distance, r_c , as a function of (a) lag time, and (b) square root of $H(\tau)$ for networks with different average filament length: $\langle l \rangle = 2$ (red squares), 5 (magenta circles), 8 (blue right triangles), 10 (cyan diamonds), and $\langle l \rangle = 13 \mu\text{m}$ (green triangles). All networks were polymerized at the same concentration ($c_A = 1 \text{ mg ml}^{-1}$ corresponding to $\xi_s = 0.3 \mu\text{m}$).

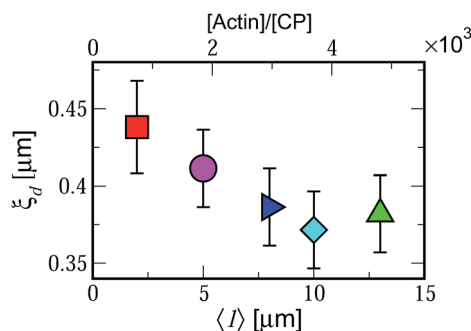


Fig. 7 Dynamic correlation length, ξ_d , as a function of the average filament length, $\langle l \rangle$ (bottom) and actin-CP concentration ratio (top). Actin concentration was held at 1 mg ml^{-1} , resulting in a $\xi_s = 0.3 \text{ } \mu\text{m}$, and $a = 0.245 \text{ } \mu\text{m}$.

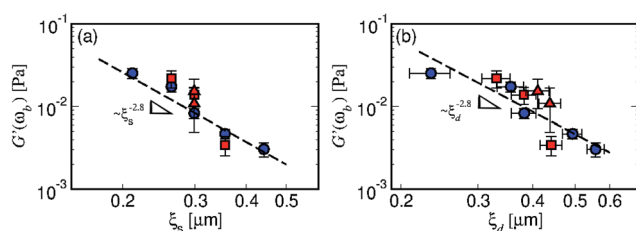


Fig. 8 The plateau elastic modulus, $G'(\omega_b)$, of all actin networks studied here, as a function of: (a) ξ_s estimated from monomer concentration, and (b) ξ_d extracted from measurements. Blue (red) symbols correspond to $a = 0.55(0.245) \text{ } \mu\text{m}$. Red squares correspond to $\langle l \rangle = 13 \text{ } \mu\text{m}$, and red triangles correspond to $\langle l \rangle = 2, 5 \text{ } \mu\text{m}$.

order of r_c and one order of magnitude larger than either ξ_s and a . These results further the notion that r_c is the length scale which is most relevant in determining explicitly the viscoelastic response of a complex fluid. The results also suggest that ξ_d can be affected by other structural features of a polymer network, in addition to ξ_s , such as its dependence on $\langle l \rangle$ demonstrated here.

We characterize the viscoelastic properties of our networks in terms of the plateau modulus, $G'(\omega_b)$, with the lowest experimentally available frequency $\omega_b = 0.14 \text{ Hz}$, following Liu *et al.*¹². In Fig. 8(a) the plateau modulus, $G'(\omega_b)$, is plotted as a function of the actin network mesh size. As expected,^{12,41} results from the various experiments fall on a single line showing a power law decay, $G'(\omega_b) \propto \xi_s^\alpha$, with a power $\alpha \approx -2.8$. However, the mesh size in these experiments is determined indirectly from the concentration of actin monomers used for gel preparation. We represent the results of Fig. 8(a) in terms of the directly measured correlation length ξ_d (Fig. 8(b)). Here too all experiments fall on the same line with $\alpha \approx -2.8$, even for networks with small filament length for which $\xi_d \neq b\xi_s$.

5. Conclusions

In this paper we have presented a new method to extract the dynamic correlation length of complex fluids from microrheology measurements, and demonstrated it on a model system of entangled F-actin networks. This new technique is

based on the observation of a crossover between the bulk and intermediate viscoelastic response of complex fluids in two point displacement correlations (D_{\parallel} , D_{\perp}). Using a generalized framework of analysis of microrheology, we show that the measured dynamic correlation length is related, but not identical, to the network mesh size. Specifically, when a third length scale is introduced into the problem, as demonstrated here with short filament lengths, ξ_d depends on it as well as on ξ_s (Fig. 7). This latter result raises several questions: how is the dynamic correlation length related to the structure of a complex fluid, and consequently, how is it related to its viscoelastic properties. More detailed experiments are required to address these issues. The technique provided here presents a platform with which to characterize in more detail the dynamics of active complex fluids, such as biologically active actomyosin networks and chemically active self healing gels.⁴²

Acknowledgements

The authors are grateful to Haim Diamant for numerous illuminating discussions. This research was supported by the Marie Curie Reintegration Grant (PIRG04-GA-2008-239378), the Israel Science Foundation grant 1271/08, and by the US-Israel Binational Science Foundation grant 2008483. A. S.-S. acknowledges funding from the Tel-Aviv University Center for Nanoscience and Nanotechnology. A. B.-G. acknowledges funding from the Israel Science Foundation (grant 1534/10).

References

- 1 T. A. Witten, *Structured Fluids*, Oxford University Press, 2004.
- 2 R. G. Larson, *The Structure and Rheology of Complex Fluids*, Oxford University Press, 1999.
- 3 T. G. Mason and D. A. Weitz, *Phys. Rev. Lett.*, 1995, **74**, 1250–1253.
- 4 T. G. Mason, K. Ganesan, J. H. van Zanten, D. Wirtz and S. C. Kuo, *Phys. Rev. Lett.*, 1997, **79**, 3282–3285.
- 5 F. Gittes, B. Schnurr, P. D. Olmsted, F. C. MacKintosh and C. F. Schmidt, *Phys. Rev. Lett.*, 1997, **79**, 3286–3289.
- 6 B. Schnurr, F. Gittes, F. C. MacKintosh and C. F. Schmidt, *Macromolecules*, 1997, **30**, 7781–7792.
- 7 J. C. Crocker, M. T. Valentine, E. R. Weeks, T. Gisler, P. D. Kaplan, A. G. Yodh and D. A. Weitz, *Phys. Rev. Lett.*, 2000, **85**, 888–891.
- 8 T. M. Squires and T. G. Mason, *Annu. Rev. Fluid Mech.*, 2010, **42**, 413–438.
- 9 A. J. Levine and T. C. Lubensky, *Phys. Rev. Lett.*, 2000, **85**, 1774–1777.
- 10 D. T. Chen, E. R. Weeks, J. C. Crocker, M. F. Islam, R. Verma, J. Gruber, A. J. Levine, T. C. Lubensky and A. G. Yodh, *Phys. Rev. Lett.*, 2003, **90**, 108301.
- 11 L. Starrs and P. Bartlett, *Faraday Discuss.*, 2003, **123**, 323–334.
- 12 J. Liu, M. L. Gardel, K. Kroy, E. Frey, B. D. Hoffman, J. C. Crocker, A. R. Bausch and D. A. Weitz, *Phys. Rev. Lett.*, 2006, **96**, 118104.
- 13 A. Sonn-Segev, A. Bernheim-Groswasser, H. Diamant and Y. Roichman, *Phys. Rev. Lett.*, 2014, **112**, 088301.

- 14 P. G. De Gennes, *Macromolecules*, 1976, **9**, 587–593.
- 15 P. G. De Gennes, *Macromolecules*, 1976, **9**, 594–598.
- 16 K. E. Kasza, A. C. Rowat, J. Liu, T. E. Angelini, C. P. Brangwynne, G. H. Koenderink and D. A. Weitz, *Curr. Opin. Cell Biol.*, 2007, **19**, 101–107.
- 17 M. L. Gardel, K. E. Kasza, C. P. Brangwynne, J. Liu and D. A. Weitz, *Methods Cell Biol.*, 2008, **89**, 487–519.
- 18 M. R. Mofrad, *Annu. Rev. Fluid Mech.*, 2009, **41**, 433–453.
- 19 J. Stricker, T. Falzone and M. L. Gardel, *J. Biomech.*, 2010, **43**, 9–14.
- 20 D. A. Fletcher and P. L. Geissler, *Annu. Rev. Phys. Chem.*, 2009, **60**, 469–486.
- 21 D. T. Chen, Q. Wen, P. A. Janmey, J. C. Crocker and A. G. Yodh, *Annu. Rev. Condens. Matter Phys.*, 2010, **1**, 301–322.
- 22 F. C. MacKintosh and C. F. Schmidt, *Curr. Opin. Cell Biol.*, 2010, **22**, 29–35.
- 23 A.-S. Smith, *Nat. Phys.*, 2010, **6**, 726–729.
- 24 Q. Wen and P. A. Janmey, *Curr. Opin. Solid State Mater. Sci.*, 2011, **15**, 177–182.
- 25 A. Palmer, T. G. Mason, J. Y. Xu, S. C. Kuo and D. Wirtz, *Biophys. J.*, 1999, **76**, 1063–1071.
- 26 M. L. Gardel, M. T. Valentine, J. C. Crocker, A. R. Bausch and D. A. Weitz, *Phys. Rev. Lett.*, 2003, **91**, 158302.
- 27 J. H. Shin, M. L. Gardel, L. Mahadevan, P. Matsudaira and D. A. Weitz, *Proc. Natl. Acad. Sci.*, 2004, **101**, 9636–9641.
- 28 M. Atakhorrami, G. H. Koenderink, J. F. Palierne, F. MacKintosh and C. F. Schmidt, *Phys. Rev. Lett.*, 2014, **112**, 088101.
- 29 C. F. Schmidt, M. Barmann, G. Isenberg and E. Sackmann, *Macromolecules*, 1989, **22**, 3638–3649.
- 30 J. A. Spudich and S. Watt, *J. Biol. Chem.*, 1971, **246**, 4866–4871.
- 31 M. T. Valentine, Z. E. Perlman, M. L. Gardel, J. H. Shin, P. Matsudaira, T. J. Mitchison and D. A. Weitz, *Biophys. J.*, 2004, **86**, 4004–4014.
- 32 J. Xu, J. Casella and T. Pollard, *Cell Motil. Cytoskeleton*, 1999, **42**, 73–81.
- 33 P. Janmey, J. Peetermans, K. Zaner, T. P. Stossel and T. Tanaka, *J. Biol. Chem.*, 1986, **261**, 8357–8362.
- 34 J. C. Crocker and D. G. Grier, *J. Colloid Interface Sci.*, 1996, **179**, 298–310.
- 35 J. C. Crocker and B. D. Hoffman, *Multiple-Particle Tracking and Two-point Microrheology in Cells*, 2007, vol. 83, pp. 141–178.
- 36 H. Diamant, in preparation.
- 37 H. Diamant, *Isr. J. Chem.*, 2007, **47**, 225–231.
- 38 S. T. Milner, *Phys. Rev. E: Stat. Phys., Plasmas, Fluids, Relat. Interdiscip. Top.*, 1993, **48**, 3674–3691.
- 39 A. J. Levine and T. C. Lubensky, *Phys. Rev. E: Stat., Nonlinear, Soft Matter Phys.*, 2001, **63**, 041510.
- 40 H. C. Fu, V. B. Shenoy and T. R. Powers, *Phys. Rev. E: Stat., Nonlinear, Soft Matter Phys.*, 2008, **78**, 061503.
- 41 H. Isambert and A. C. Maggs, *Macromolecules*, 1996, **29**, 1036–1040.
- 42 P. Cordier, F. Tournilhac, C. Soulié-Ziakovic and L. Leibler, *Nature*, 2008, **451**, 977–980.

Chapter 4

Statistics of discrete motor-driven events in reorganizing active networks

4.1 Introduction

Many living systems exhibit coordinated motion of individual entities which are capable of harnessing energy from their environment to induce motion. Examples for such processes range from flocking of fish to cell division by the reorganization of the cell's skeleton proteins. These phenomena have inspired the study of biological as well as synthetic active matter. Due to their energy consumption, active materials are intrinsically out of thermal equilibrium. Consequently, their internal fluctuations need not be distributed according to Gaussian statistics. In fact, although Gaussian distributions of tracer particle motion have been observed in bacterial suspensions [87], this is not the general case. A Gaussian distribution superimposed with fat exponential tails seems more prevalent, and has been observed in many active systems including active granular materials [88], active DNA gels [89], suspensions of eukaryotic microorganisms [90], within living cells [91], and in re-

constituted cytoskeleton networks [77, 78]. In these systems it is believed that the central Gaussian distribution is a combination of fluctuations due to thermal energy and the contribution of many distant sources of active motion. The fat exponential tails are usually attributed to a few local internal sources of active force [77, 89, 90]. The origin of the exponential statistics of the tails of the distribution is thought to be related to the randomness and time-independence of events responsible for the large displacements contributing to these tails [77], which follow Poisson statistics.

The statistics of a single active event has been studied in a bottom-up approach, looking, for example, at the dynamics of a single motor molecule stepping along a filament [92, 93], or at the detachment dynamics of a single motor protein from its substrate filament [94]. These measurements are highly informative and provide insights into the operation mechanism of single motors. However, in order to attest to the coordinated activity of motors in the highly correlated systems mentioned above, one should study these active events by looking at their dynamics *in-situ*.

In this chapter we study experimentally the dynamics of discrete active events *in-situ*. To do so we chose a model system of *in-vitro* reconstituted active gels based on cytoskeleton proteins made of the structural protein actin and its molecular motor counterpart myosin II. Both actin and myosin II are key components in cell motility and muscle contraction. Myosin motor domains (heads) generate active motion by hydrolysis of chemical fuel in the form of adenosine triphosphate (ATP). The hydrolysis process promotes a configuration change in the myosin's domains structure, which results in a stepwise walking along the actin filament. One important and unique feature of myosin II is its ability to form multimeric bipolar structures (termed mini-filaments) containing tens to hundreds of myosin molecules [83, 95]. The number of myosin heads within such a mini-filament can be tuned by the salt concentration in the self-assembly buffer [83]. This structure allows the myosin mini-filaments to connect different actin filaments and move them relative to each other, thereby generating contractile forces inside the network. The detachment rate of myosin heads from actin filaments is governed by ATP concentration due to its ATP consumption. In the absence of ATP, myosin heads bind the filaments con-

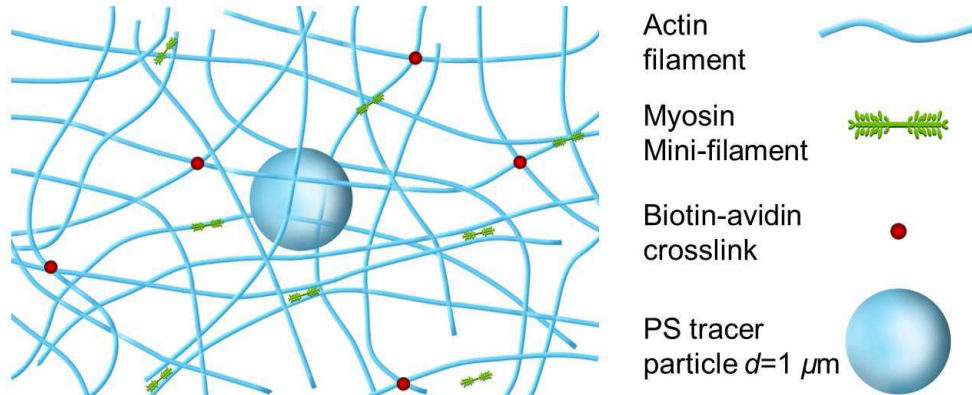


Figure 4.1: Schematic illustration of the active gel and its components. Myosin mini-filaments are embedded within a network of actin filaments, cross-linked by biotin-avidin connection. The fluctuations of the network are probed by the tracer particle (1 μm diameter) motion.

stantly, and the mini-filaments act as static cross-linkers between actin chains. In the presence of ATP, the motor clusters generate pinching forces determined by the size of the motor cluster [83]. These pinching forces can result in actin aggregation (known as superprecipitation) [96] or in disassembly of the actin network [82, 97], unless the network is stabilized by static cross-linkers.

In our experimental system, the actin-myosin network is kept mechanically stable by the addition of passive, chemical cross-linkers (via biotin-avidin bonds). Our purpose is to achieve active gels with varying degree of activity maintaining steady-state dynamics for long durations, in order to collect sufficient statistics on motor activity. To this end we keep the network features fine, refraining from bundling the actin filaments by the choice of a suitable cross-linker [81]. In our system we use small mini-filaments of motor proteins containing only tens (19 or 32) of two-headed myosin molecules, and provide a low but constant concentration of ATP. In this ATP concentration the motor clusters have higher probability to act as biological cross-linkers, i.e., they stay connected to the actin filaments for longer durations. In addition, the pinching forces applied by these small motor clusters have a limited range of motion due to the relatively small number of heads

in each cluster and the shortage in ATP. This limitation ensures that, while the motors generate active forces in the network, there is no large-scale reorganization or deformations of the network, i.e., keeping the steady state dynamics. These conditions allow us to decouple the effect of motor activity on fluctuations from its effect on structural evolution. To follow the active fluctuations in our gels we use embedded tracer particles, with size on the order of or larger than the network mesh size, so that their motion will reflect the fluctuations of the network. By design the actin network's mesh size is $0.3 \mu\text{m}$, the average distance between the static chemical cross-links in our system is on the order of $3 \mu\text{m}$, the tracer particle size is $1 \mu\text{m}$ in diameter, and the average distance between myosin mini-filaments ranges from $50 \mu\text{m}$ to $1.3 \mu\text{m}$. A schematic illustration of our experimental model system is shown in Fig. 4.1.

4.2 Material and sample preparation

Active actin-myosin networks were reconstituted *in vitro* by polymerizing G-actin in the presence of biotin-avidin crosslinkers and myosin II mini-filaments. G-actin was purified from rabbit skeletal muscle acetone powder [98], with a gel filtration step, stored on ice in G-buffer (5 mM Tris HCl, 0.1 mM CaCl_2 , 0.2 mM ATP, 1 mM DTT, 0.01% NaN_3 , pH 7.8) and used within two weeks. Purification of myosin II skeletal muscle was done according to standard protocols [99]. The concentration of the G-actin and myosin II was determined by absorbance measured using UV/Visible spectrophotometer (Ultraspec 2100 pro, Pharmacia) in a cuvette with a 1 cm path length and the extinction coefficients: G-actin - $\epsilon_{290} = 26,460 \text{ M}^{-1}\text{cm}^{-1}$ and two-headed myosin II - $\epsilon_{280} = 268,800 \text{ M}^{-1}\text{cm}^{-1}$. Myosin II dimers were stored at -80°C in high salt buffer (0.5 KCl) that preserves them in a monomeric form. Biotinylated actin (Cytoskeleton, Inc.) and neutravidin (Invirogen, used as a cross-linker) were premixed with unlabeled actin and left over at least one hour on ice. The ratios were unlabeled: biotinylated: neutravidin = 5000:5:2 giving a total actin concentration of $24 \mu\text{M}$ and an average distance between cross-linkers of $\approx 3 \mu\text{m}$. To initiate the

formation of processive myosin II minifilaments, the myosin solution was diluted with G-buffer to the desired KCl concentration, 0.13 M or 0.1 M, corresponding to motor clusters, each composed of $N_{myo} \approx 19$ or 32 myosin domains, respectively [83]. Polystyrene colloids with radius of $0.55 \mu\text{m}$ (Invitrogen, Lot #742530) were pre-incubated with a 10 mg/ml BSA solution to prevent non specific binding of protein to the bead surface [16]. We set the average filament length to be $\approx 13 \mu\text{m}$ by addition of capping protein.

Active network formation was initiated by adding the actin solution, myosin minifilaments in various concentrations, capping protein and beads to motility buffer (10 mM HEPES, 1 mM MgCl_2 , 0.1 mM MgATP, 0.5 mg/mL creatine kinase, 5 mM creatine phosphate, 0.2 mM EGTA, and 0.1 or 0.13 M KCl). Creatine kinase and phosphate were used as an ATP regenerating system. Immediately after polymerization the sample was infused into a glass cell, $150 \mu\text{m}$ high, and sealed with grease. The glass surfaces were coated with methoxy-terminated polyethylene glycol to prevent binding of the proteins to the glass. Shortly after cell loading, samples were fluorescently imaged at $\lambda = 605 \text{ nm}$ with $40\times$ air objective. Each sample is monitored for approximately 160 min, in which short movies are taken every fifteen minutes, starting from ~ 5 min after polymerization. The initial gelation process of the samples takes place in the first few minutes of the experiment. To avoid wall effects imaging was done at a plane distanced at least $80 \mu\text{m}$ from the cell walls. Particle motion was recorded using a CMOS video camera (Gazelle, Point Gray) at a frame rate of 70 Hz and was tracked with accuracy of at least 13 nm using conventional algorithms [100].

4.3 Results and discussion

The statistics of active events should depend on the amount of activity in the system. To examine this we performed two series of experiments, one with myosin mini-filaments containing 19 heads per cluster and the other with myosin mini-filaments containing 32 heads per cluster. In each series of experiments we varied the

myosin concentration from $[\text{Myosin}]/[\text{Actin}]=0$ to $[\text{Myosin}]/[\text{Actin}]=0.02$ ($N_{myo} = 19$) and $[\text{Myosin}]/[\text{Actin}]=0.01$ ($N_{myo} = 32$), corresponding to a ratio of myosin mini-filaments to actin filaments $0 < F_{myo}/F_{actin} < 4$ and $0 < F_{myo}/F_{actin} < 1.5$, respectively (F_{actin} is calculated by considering that there are 370 actin subunits in a $1 \mu\text{m}$ long filament). These series of experiments allow us to explore the change in tracer particles motion once activity is added to the system, as well as the effect of increasing activity (in the form of both concentration and size of motors).

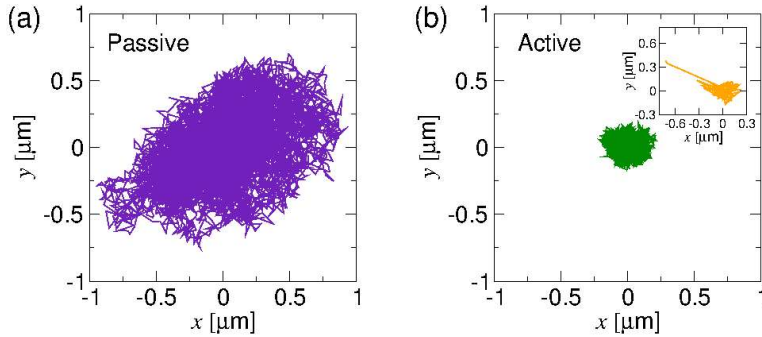


Figure 4.2: Typical trajectory of a $1 \mu\text{m}$ polystyrene particle in the cross-linked actin network. (a) passive network, $[\text{Myosin}]/[\text{Actin}]=0$ and (b) active network, $[\text{Myosin}]/[\text{Actin}]=0.02$. Motor mini-filaments are constructed with $N_{myo} = 19$ myosin heads. The two trajectories were taken at 70 Hz for about 140 s. An example of a trajectory of particle that experiences large steps is plotted in the inset of (b).

Representative trajectories of tracer particles are presented in Fig. 4.2, where a trajectory of a tracer particle (140 s long) in an actin gel containing no myosin motors (passive gel - Fig. 4.2(a)), is compared to a trajectory of a tracer in an active gel ($[\text{Myosin}]/[\text{Actin}]=0.02$, Fig. 4.2(b)) of the same duration. Both trajectories show that the tracer particle undergoes diffusive-like motion, where the particle embedded in the active gel seems more confined. This observation is counter-intuitive, since we expect motor activity to enhance the gel's fluctuations and as a result the tracer particles motion. However, motor proteins are also known to stiffen actin gel due to two effects: they act as additional cross-linkers, and they apply tension on the actin filaments. Both processes reduce the entropy of the network causing it to stiffen. This stiffening effect is present in all our experiments and increases as motor

concentration increases (see below). Therefore, we assume that the added active fluctuations from the motor's activity have a weaker effect on the range of motion of tracer particles than the increase in stiffness they induce. Some of the particles in the active gels are experiencing relatively large displacements that usually do not persist in the same direction (see inset of Fig. 4.2(b)).

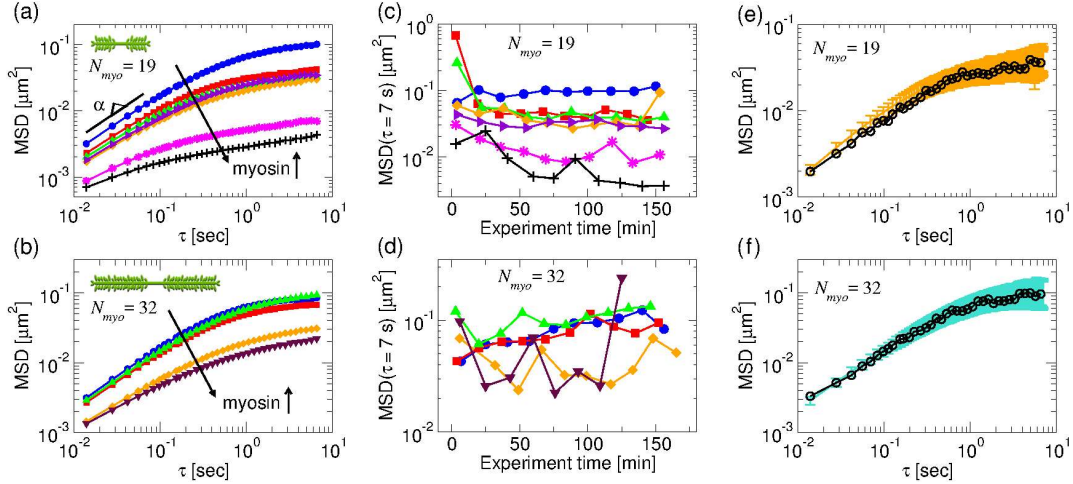


Figure 4.3: Mean squared displacement (MSD) of particles in networks with different [myosin]/[actin] at two mini-filaments sizes. (a) and (b) time and ensemble-averaged MSD of probe particles as a function of lag-time τ approximately 100 mins after polymerization. Mini-filaments are constructed by $N_{myo} = 19$ (a) or $N_{myo} = 32$ (b) myosins heads. (c) and (d) MSD at $\tau = 7$ s along the experiment time. Sizes of mini-filaments are $N_{myo} = 19$ (c) and $N_{myo} = 32$ (d). Colors and symbols correspond to different [Myosin]/[Actin] ratios: 0 (blue circles), 0.0017 (red squares), 0.0025 (green triangles), 0.005 (orange diamonds), 0.0083 (violet right triangles), 0.01 (maroon down triangles) 0.012 (magenta stars) and 0.02 (black pluses). (e) and (f) Comparison between time-averaged and ensemble-averaged MSD for networks with [Myosin]/[Actin]=0.0025 approximately 100 min after polymerization. Sizes of mini-filaments are $N_{myo} = 19$ (e) and $N_{myo} = 32$ (f).

To quantify the tracer particles' motion we calculate their time- and ensemble-average mean squared displacement (MSD) from their trajectories. In Fig. 4.3(a) and (b) the MSD as a function of lag-time τ is plotted for all our networks, with the small and larger motor clusters respectively. The MSD in the passive networks has

the characteristic, expected behavior of a weakly cross-linked network [78,79]. As the motor concentration increases we observe a decrease in the values of the MSDs, while the shape of their curves is qualitatively preserved. The stiffening effect, which the motor proteins have on the network, is observed here as well, from the decreases of the MSD with the increase in the myosin concentration. Repeating this measurement as the gels mature allows us to detect the network evolution. For comparison we plot in Fig. 4.3(c) and (d) the MSD of the tracers at a lag time of $\tau = 7$ s. For the smaller mini-filaments experiments ($N_{myo} = 19$) it is easy to see that after approximately 50 min most of the networks reach steady-state conditions (Fig. 4.3(c)). The two networks with the highest concentrations of myosin ($[\text{Myosin}]/[\text{Actin}] = 0.0125, 0.02$) do not show a clear steady state but rather exhibit slow evolution throughout the entire experiment time. The networks with larger mini-filaments behave in a similar if less obvious manner (Fig. 4.3(d)). Here, the two networks with the highest myosin concentrations ($[\text{Myosin}]/[\text{Actin}] = 0.005, 0.01$) are much noisier; however, they still exhibit steady-state dynamics. We further verify the steady-state properties of the gels with low myosin concentrations by comparing the ensemble-averaged MSD to the time-average MSD and find that they coincide (Fig. 4.3(e) and (f)). These comparisons were conducted for networks with $[\text{Myosin}]/[\text{Actin}] = 0.0025$ for both motor sizes, and the same trend was observed in all networks which exhibit steady-state dynamics in the MSD plots of Fig 4.3(c) and (d).

The MSD alone is not informative enough for characterization of the non-equilibrium effect of motor proteins. We thus look, in addition, at the probability distribution of probe particle displacements as a function of lag time τ , $P(\Delta x, \tau)$, known as the van Hove correlation function (Fig. 4.4). By looking at these distributions, the statistics of particle fluctuations can be resolved, and should provide insight into the active events influencing the particle motion. As expected in passive gels, the van Hove correlations are Gaussian-like, since the fluctuations of particles are purely thermal with only small deviations due to the network's heterogeneous cross-linking structure. At low myosin concentrations the displacement distributions are Gaussian-like, with widths that decrease gradually with the increase in myosin concentration, in accord with the stiffening effect discussed above. How-

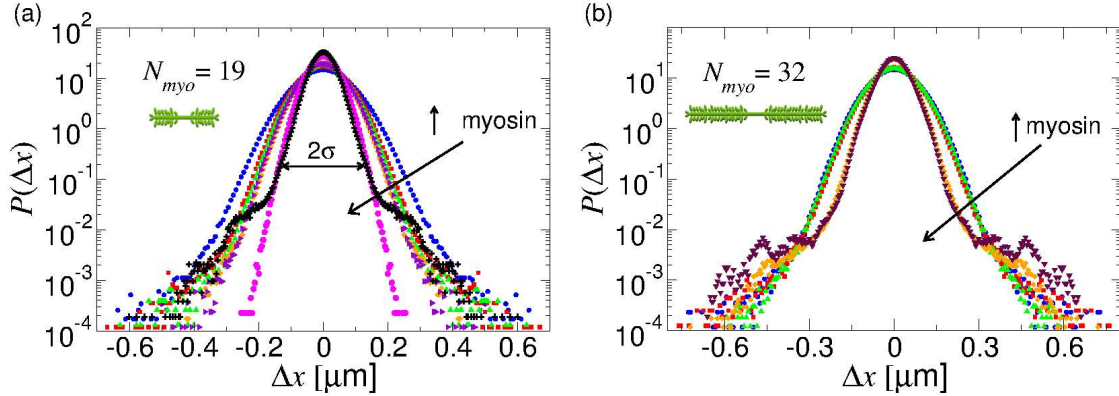


Figure 4.4: Ensemble-averaged van Hove correlation functions of probe particles at lag time $\tau = 0.014$ s for networks with increasing myosin concentrations at two different mini-filament sizes; (a) $N_{myo} = 19$ and (b) $N_{myo} = 32$. Colors and symbols correspond to different $[\text{Myosin}]/[\text{Actin}]$ ratios: 0 (blue circles), 0.0017 (red squares), 0.0025 (green triangles), 0.005 (orange diamonds), 0.0083 (violet right triangles), 0.01 (maroon down triangles), 0.012 (magenta stars) and 0.02 (black pluses). Distributions were taken approximately 100 min after polymerization.

ever, above a certain motor concentration threshold we observe the appearance of shoulders ($N_{myo} = 19$, Fig 4.4(a)) and peaks ($N_{myo} = 32$, Fig 4.4(b)) in the displacement distribution. This threshold concentration is $[\text{Myosin}]/[\text{Actin}] = 0.015$ for the small clusters and $[\text{Myosin}]/[\text{Actin}] = 0.004$ for the large clusters. This result is in contrast with similar measurements performed on active networks [77–79, 89], in which an exponential fat tail was observed. The distinct shoulders and peaks in such a distribution was observed previously in an experimental system of rod-like viruses hopping between smectic layers, where the size of these jumps had a characteristic length-scale related to the rod length [101]. In our system we relate the peaks/shoulders to discrete events with a cutoff on the displacement that they induce in the system (see below).

To characterize the effect of motors activity on the networks we measure multiple parameters of the non-equilibrium activity, as suggested in Ref. [78]. The first parameter is the diffusion (MSD) exponent, α , where α is measured for lag-times

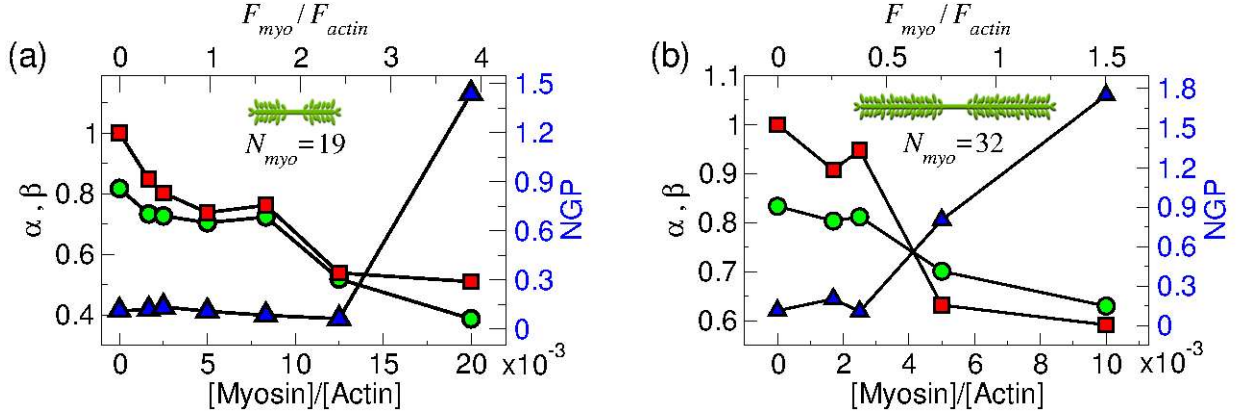


Figure 4.5: Multiple parameters of non-equilibrium activity. Diffusive exponent α (green circles), the Gaussian standard deviation ratio β (red squares) and the non-Gaussian parameter, NGP (blue triangles). The parameters were measured in networks with increasing $[Myosin]/[Actin]$ (or equivalently F_{myo}/F_{actin}) ratios at two different sizes of mini-filaments $N_{myo} = 19$ (a) and $N_{myo} = 32$ (b). Parameters were measured approximately 100 min after polymerization.

between ~ 0.01 - 0.1 s (see Fig. 4.3(a) for clarity). In these lag-times we observe the new features (shoulders and peaks) in $P(\Delta x)$. In weakly cross-linked semi-flexible networks α usually takes values of $\sim 0.75 - 0.85$ [102]. A decrease in its value implies that the tracer experiences a more stiffened or confined environment. The second parameter is the standard deviation of the Gaussian part of the van Hove correlation, σ , scaled by the standard deviation of the Gaussian in the passive gel, $\beta = \sigma_{active}/\sigma_{passive}$ (see Fig. 4.4(a) for clarity). This ratio gives information on the non-equilibrium activity in the Gaussian part of the correlation. A stiffening or confinement effect in the environment of the particles should correspond to values of $\beta < 1$, while an activity induced broadening should result in $\beta > 1$. The third parameter is the non-Gaussian parameter (NGP),

$$NGP = \frac{\langle \Delta x(\tau)^4 \rangle}{3\langle \Delta x(\tau)^2 \rangle^2} - 1, \quad (4.1)$$

which quantifies the non-equilibrium effect on the non-Gaussian part of the van Hove distribution. For a Gaussian distribution the NGP is zero, whereas values

larger than zero indicate an increased probability to perform large displacements and deviation from Gaussian statistics. In Fig. 4.5(a) and (b) the three parameters are plotted as a function of the concentration ratios of myosin to actin, showing a motor concentration threshold above which a significant change in the network characteristics occurs, $[\text{Myosin}]/[\text{Actin}]_{\text{thresh}} = 0.015$ for small mini-filaments and $[\text{Myosin}]/[\text{Actin}]_{\text{thresh}} = 0.004$ for large mini-filaments. In terms of $F_{\text{myo}}/F_{\text{actin}}$, the threshold appears at a ratio of ~ 3 myosin filaments per actin filament for the small motors, while in the larger motor the threshold ratio is less than 1 myosin filament per actin filament. For the small motors the cross-over coincides with a transition from steady-state to evolving gels as observe in Fig. 4.3(c) and (d). While both α and β decrease when more motors are added, confirming the stiffening of the gels, the stiffness increases dramatically above the threshold motor concentration. The NGP is constant and approximately zero below the transition, indicating Gaussian-like statistics of particle motion as observed in the van-Hove distribution (Fig. 4.4). However above the threshold concentration the NGP starts to increase significantly. Importantly, the threshold concentrations observed here in the three parameters coincide with the threshold concentration above which the shoulders or peaks appear in the displacement distributions discussed above. It is obvious that the onset of the increase in NGP coincides with appearance of shoulders or peaks in the displacement distribution, as NGP measures deviation from Gaussianity. However, the agreement between the threshold concentration above which a dramatic stiffing is observed is not straightforward.

To investigate the temporal dependence of the active events we looked at the distributions of particle displacements in the networks with the highest myosin concentration ($[\text{Myosin}]/[\text{Actin}]=0.02$, $N_{\text{myo}} = 19$ and $[\text{Myosin}]/[\text{Actin}]=0.01$, $N_{\text{myo}} = 32$) at different lag-times (note that Fig. 4.4 was calculated for the shortest lag-time, $\tau = 0.014$ s). In Fig. 4.6(a) and (b) the distributions are plotted for lag-times between $\tau = 0.014 - 0.14$ s. These plots reveal that (i) the locations and heights of the peaks/shoulders do not change as the lag-time increases, and (ii) as lag-time increases the central Gaussian broadens and masks the shoulders/peaks, resulting in a Gaussian like shape of the distributions. This is further verified when looking

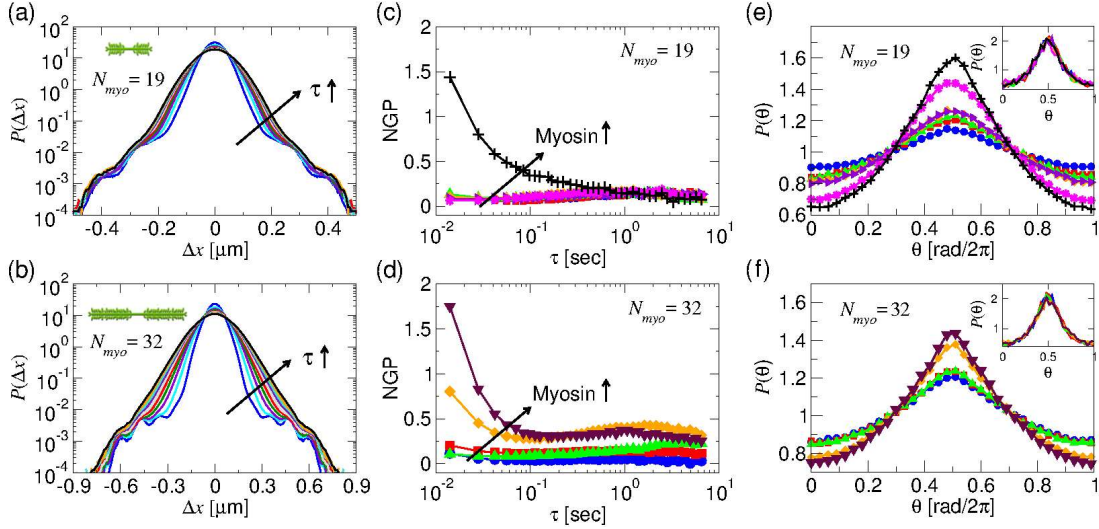


Figure 4.6: Ensemble-averaged van Hove correlation functions for different lag times for networks with (a) $[\text{Myosin}]/[\text{Actin}] = 0.02$, $N_{myo} = 19$ and (b) $[\text{Myosin}]/[\text{Actin}] = 0.01$, $N_{myo} = 32$. Colors correspond to different lag times: $\tau = 0.014$ (blue), 0.028 (cyan), 0.042 (violet), 0.056 (green), 0.07 (red), 0.084 (grey), 0.098 (indigo), 0.112 (turquoise), 0.126 (orange) and 0.14 s (black). (c) and (d) NGP as a function of τ , for networks with increasing myosin concentrations. Mini-filament sizes are (c) $N_{myo} = 19$ and (d) $N_{myo} = 32$. (e) and (f) relative angle distributions for networks with increasing myosin concentrations at $\tau = 0.014$ s. Mini-filament sizes are (e) $N_{myo} = 19$ and (f) $N_{myo} = 32$. Insets of (e) and (f) are the angle distributions of the same network at $\tau = 2$ s. Colors and symbols are the same as in Fig. 4.3 and Fig. 4.4.

at the NGP for increasing lag-times (Fig. 4.6(c) and (d)). For networks exhibiting the active features in their distributions, the initial value of NGP is larger than 0.8 and drops to values smaller than 0.4 after $\tau \approx 0.2$. For networks that do not exhibit these features (motor concentrations below the threshold) the NGP is almost constant and close to zero at all observed lag-times. These observations imply that the duration of active events taking place in the network are shorter than 0.014 s (the shortest lag-time), and therefore do not produce directed motion for long durations as was reported previously [77–79]. This assumption is further verified by looking at the distribution of relative angles between successive time intervals of random walk

trajectories, rather than distributions of step sizes, following the approach of Burov et al. [103]. In this analysis the angle between successive steps is measured, $\theta(t, \tau)$, which is defined as

$$\cos \theta(t, \tau) = \frac{\Delta \vec{X}(t, \tau) \cdot \Delta \vec{X}(t + \tau, \tau)}{\left| \Delta \vec{X}(t, \tau) \right| \cdot \left| \Delta \vec{X}(t + \tau, \tau) \right|}, \quad (4.2)$$

where $\Delta \vec{X}(t, \tau) = \vec{X}(t + \tau) - \vec{X}(t)$, and $\vec{X}(t)$ is the particle trajectory. In confined environments the particles are experiencing a large restoring force which should result in higher probabilities of $\theta = \pi$. In systems where there is an active motion, which results in higher probabilities for large displacements, if the event of active motion lasts for several frames in the movie, then there should be elevated probabilities for $\theta = 0$ or 2π . Figure 4.6(e) and (f) show $P(\theta)$ at the shortest lag time ($\tau = 0.014$ s) for all our experiments. It can be seen clearly that at high motor concentrations, above the threshold, there is elevated probability for $\theta = \pi$, confirming that the duration of active events is shorter than this lag-time. The absence of directed motion for several lag-times can be associated with the relatively small size of motors clusters containing only 19 or 32 heads, compared to previous studies that reported directed motion caused by motor clusters composed of hundreds of myosin heads. The insets in Fig. 4.6(e) and (f) correspond to $P(\theta)$ at a much larger lag-time of $\tau = 2$ s, and show that at this lag-time all angle distributions of gels with different myosin concentrations coincide. This suggests that the tracer particles undergo similar statistical processes, and supports the observations discussed above.

As suggested above, we attribute the appearance of shoulders and peaks in the displacement distributions to a cut-off in the displacement of a particle resulting from a single active event. To support this suggestion we conducted a series of simulations of particle motion in one dimension. In each simulation 100000 particles undergo thermal and active motion, where their thermal displacements are randomly drawn from Gaussian distributions with standard deviation of $\sigma = 0.1$ and zero mean. The active events displacements are randomly drawn from one of three different distributions: (1) an exponential distribution with decay parameter of 1 [$P(\Delta x) \propto$

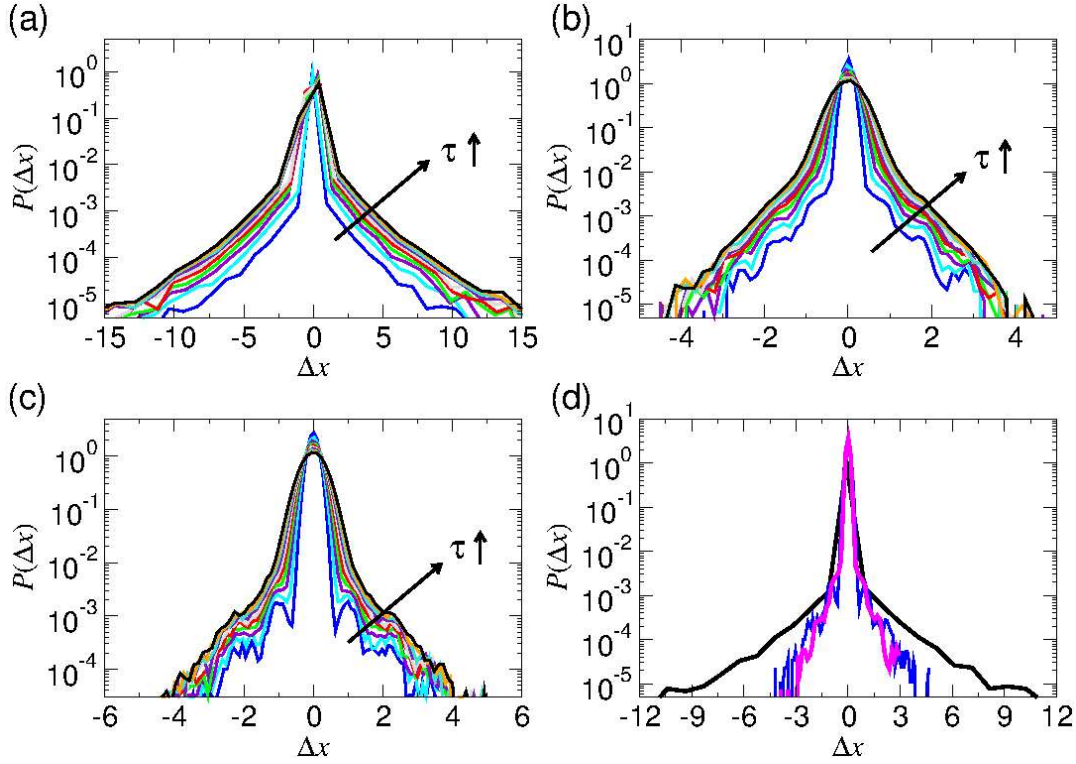


Figure 4.7: Simulated particle motion. Displacements were randomly drawn from Gaussian distributions ($\sigma = 0.1$) and (a) Exponential distribution with parameter $\mu = 1$. (b) Exponential ($\mu = 1$) with a cutoff at $|\Delta x| = 1$ for displacements and Poisson distributions for events occurrence ($\lambda = 0.5$). (c) Uniform distribution at $|\Delta x| = 1 \pm 0.25$ for particle displacements, and Poisson distributions for events occurrence ($\lambda = 0.5$). Plots (a)–(c) present the overall displacement distribution of 100000 particles for 10 successive lag times. (d) Distributions at the first lag-time for the three distributions of (a)–(c). Colors correspond to the different distributions: exponential (black), exponential with cut-off distance (magenta) and uniform distribution (blue).

$\exp(-|\Delta x|)$], (2) the same exponential decay as in (1) with a cut-off at distances larger than 1 [$P(|\Delta x| > 1) = 0$], and (3) a uniform distribution between $0.75 < |\Delta x| < 1.25$ [i.e., $P(0.75 < |\Delta x| < 1.25) = 1$, and $P(|\Delta x| < 0.75 \text{ or } |\Delta x| > 1.25) = 0$]. On top of the active displacements, we assumed that the probability to have an active event in the first place follows Poisson statistics with parameter of $\mu = 0.5$.

The overall displacement of the particles is the sum of thermal and active motion. The distribution of step sizes from all three simulations are plotted in Fig. 4.7(a)–(c), for increasing lag-time (similar to Fig. 4.6(a)–(b)). In the active events without cut-off we recover the fat exponential tail superimposed on the central Gaussian distribution as was observed previously in active actin gels [77–79]. Once a cutoff is introduced to the active events’ displacement distributions, we notice the appearance of peaks and shoulders. Interestingly, the locations of the peaks does not change as lag-time increases, and eventually they are masked out by the broadening of the central Gaussian, exactly as was observed in our experiments (Fig. 4.6(a) and (b)).

The origin of the cutoff in the active displacements distributions can be understood from the small size of our motors. Since our motors are constructed from 19 or 32 myosin heads, the motors are able to produce a processive movement of only a few (1-3) steps before the cluster is detached from the filament and the build-up tension is released. The reason for this is the low duty ratio of a myosin head, which is approximately 0.1, meaning that only 10% of the time the myosin head is attached to the actin filaments [83]. In order to produce processive motion along a filament a second head must connect to the filament before the first head is detached. In large mini-filaments which contain hundreds of heads, there is relatively high probability for such process to occur, and the cluster can produce tens and hundreds of steps before detaching completely from the filament. In our small motor filaments, due to the short processive motions, there should be a cutoff in the amount of force the motors can exert on the network, which translates to a cutoff in the active events’ displacement. This implies that actually the peaks/shoulders in the distributions correspond to discrete motor events of 1-3 steps. In the following we further support this assumption by looking at the forces which are related to such displacements.

Looking again at the displacement distributions exhibiting the peaks or shoulders for the two cluster sizes (Fig. 4.8(a)) reveals that (i) the larger motors produce larger active displacements, and (ii) different concentrations of the same cluster size produce similar displacements (brown oval in Fig. 4.8(a)). These two observations support our assumption that the peaks correspond to discrete motor events and their extent is determined mainly by motor size. We further support this by pro-

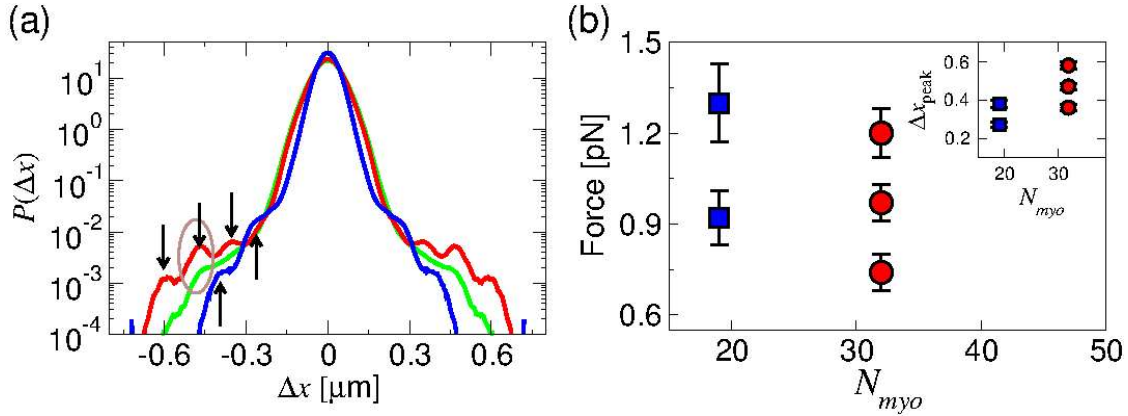


Figure 4.8: (a) Ensemble-averaged van Hove correlation functions at $\tau = 0.014$ s showing peaks or shoulders at large displacements. Different colors correspond to different networks; $[\text{Myosin}]/[\text{Actin}] = 0.02$, $N_{myo} = 19$ (blue), $[\text{Myosin}]/[\text{Actin}] = 0.005$, $N_{myo} = 32$ (green) and $[\text{Myosin}]/[\text{Actin}] = 0.01$, $N_{myo} = 32$ (red). Arrows point to displacements of higher probability (Δx_{peak}), i.e., the appearance of peaks/shoulders. The brown oval highlights that at the same N_{myo} , some of the peaks appear at the same displacement. (b) Using the values of Δx_{peak} extracted from (a) (see inset) the force applied by the motors at a single active event is estimated (see text for explanation).

viding rough estimations of the forces required to produce such displacements. For that purpose we assume that the network can be considered as an elastic medium, and therefore the force is equal to $F = k\Delta x_{peak}$, with Δx_{peak} the characteristic displacements of the peaks/shoulders, and k is related to the stiffness of the elastic network. An exact value of k can be extracted only from macrorheology or active microrheology, which were not performed here; however, an estimated value can be extracted from the displacement distributions. In our experiments the central Gaussian of the displacement distribution is indeed sensitive to network elasticity. In addition it is also sensitive to active (distant) events taking place in the network. Therefore, a lower bound of k can be estimated from the central Gaussian of the distribution with $k_B T = k\sigma^2$. The forces applied in a single active event, calculated by this approach, were between 0.7-1.4 pN (Fig. 4.8(b)). These estimations are on the order of the force produced by a single motor head during one hydrolysis cycle

(approximately 1.4 pN [104]), and correspond to only few processive steps of heads before the motor cluster is detached from the network, in agreement with the short duration of active events discussed above.

Motor concentration determines the average distance between motors, which in turn affects the probability that a motor cluster will be close enough to the tracer to induce such large displacements. One interesting question is what is the distance above which the motor is considered distant and its activity will influence the central Gaussian, or below which the motor is close enough and can induce the peak formation in the particle displacement distribution. This distance defines the transition between the bulk (distant) environment and the local (close) environment with respect to the tracer particle position (see Fig. 4.9(a)), and can be used to estimate the number of motor mini-filaments that strongly affect the tracer's fluctuation. In order to understand and estimate what this distance is, we should look at how a mechanical perturbation is decaying in the active gels.

Active events produce mechanical perturbations in the networks, which decay with distance in a manner related to the network response. A natural method to measure this spatial decay is 2P microrheology described in Sec. 2.1.5 [26, 105], which uses the 2P displacement correlations at different inter-particle separations to characterize this decay. The 2P displacement correlations are calculated as:

$$\begin{aligned} D_{\parallel}(r, \tau) &= \langle \Delta X_{\parallel}^i(t, \tau) \Delta X_{\parallel}^j(t, \tau) \delta(r - R^{ij}(t)) \rangle \\ D_{\perp}(r, \tau) &= \langle \Delta X_{\perp}^i(t, \tau) \Delta X_{\perp}^j(t, \tau) \delta(r - R^{ij}(t)) \rangle, \end{aligned} \quad (4.3)$$

where $\Delta X_{\parallel}^i(t, \tau)$ ($\Delta X_{\perp}^i(t, \tau)$) is the displacement of particle i during the time between t and $t + \tau$, projected parallel (perpendicular) to the line connecting the pair, and $R^{ij}(t)$ is the pair separation at time t . In our previous work, described in sec. 3.2, we showed that in actin networks the mechanical perturbations, over an intermediate range of distances, decay much faster with distance than is usually expected, due to the features in the network structure at the mesoscopic length-scales [105, 106]. Fig. 4.9(b) and (c) show typical plots of the 2P displacement correlation in our active networks. As in passive actin networks (Sec. 3.2), the correlated diffusion in the longitudinal direction decays fast $D_{\parallel} \sim r^{-3}$ at short distances and slowly

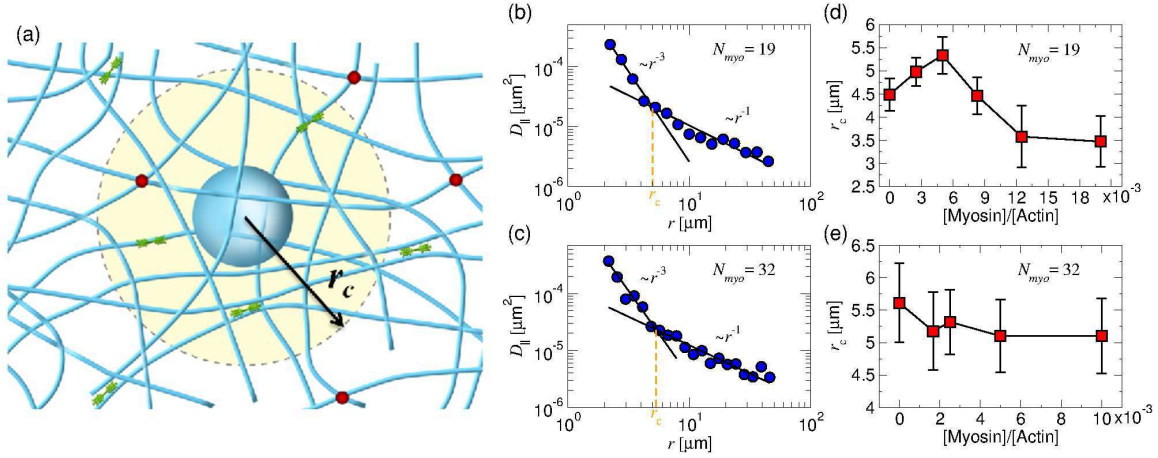


Figure 4.9: (a) Illustration of the volume around the particle where motors strongly affect the tracer’s fluctuations. (b) and (c) Longitudinal displacement correlations as a function of particle separation at lag time $\tau = 0.014$ s. Network parameters were $[\text{Myosin}]/[\text{Actin}] = 0.0025$ with $N_{\text{myo}} = 19$ (b) and $N_{\text{myo}} = 32$ (c). The cross-over distance (orange dashed line) is defined at the intersection of the fitted bulk (r^{-1}) and intermediate (r^{-3}) power-law decays of D_{\parallel} . (d) and (e) the cross-over distance in networks with increasing myosin concentration, for small (d) and large (e) mini-filaments motors.

$D_{\parallel} \sim r^{-1}$ at large distances. The cross-over distance between the two regimes of elastic response, r_c , gives an estimate for the range from which the particle will be most susceptible to motor action. r_c ranges in our active systems between $4.5 - 3.5 \mu\text{m}$ and $5.5 - 5.0 \mu\text{m}$ for $N_{\text{myo}} = 19$ and 32 respectively (Fig. 4.9(d) and(e)). In addition, we estimate the distance between myosin mini-filaments assuming they are dispersed isotropically and are all attached to the network to be in the range of $15.4 - 1.3 \mu\text{m}$ and $26 - 4.3 \mu\text{m}$ for the small and big motors respectively. This means that at the highest myosin concentrations there are an order of 1-10 mini-filaments in the vicinity of the particle, depending on the mini-filaments sizes. However, it is important to note that the probability that all these clusters will generate active events simultaneously is practically zero, at our experimental condition (low ATP, relatively small-size cluster). There is a larger probability that a few (1-3) events will occur in the duration of the shortest lag-time ($\tau = 0.014$ s), since a myosin

head produces its power stroke in ~ 5 ms [107]. Therefore, the occurrence of a few events during this lag-time should lead to a few peaks/shoulders in the distributions. The contribution from larger distances decays slower and thus averages over a much larger number of motors, contributing to the central Gaussian of the distribution, as expected from the central limit theorem.

To the best of our knowledge, the displacement distributions with shoulders and peaks of Fig. 4.4 were not observed previously in an experimental system based on active motion of motors. A recent theoretical study, aimed at modeling the fluctuations of a tracer particle in an active gel, suggested a particle displacement distribution with similar features to our experimentally measured distributions [108]. In this theoretical study the tracer’s motion is calculated while modeling the elastic gel as a Gaussian trap and having motor-induced active fluctuations in addition to thermal fluctuations. The active force in this model arises from the independent and random action of motors in the gel with a given finite displacement. At short time scales of the order of the interval between single motor kicks, and at low motor densities, discrete active event statistics are observed in the van Hove correlation function. However, as the motor density and the displacement measurement lag time τ increase, the distribution is shown to converge to a Gaussian distribution [108]. This model seems to capture the source of the fluctuation spectrum observed in our experiments, and supports our interpretation of a cut-off in the step size of a tracer particle in the active gels.

4.4 Conclusion

We have studied the non-equilibrium fluctuations of tracer particles in active actin-myosin networks. To decouple the structural evolution of the networks from their fluctuations, we chose an experimental model system containing fine network features and relatively small motor mini-filaments that are able to produce only small processive motions. Our experiments reveal that the stiffening effect of motor proteins dominates over the active fluctuations resulting in a narrowing of the displace-

ment distributions, while preserving their Gaussian-like shape as motor concentration increases. At sufficiently large motor concentrations, where on average there is at least one motor in the proximity of the tracers, the active fluctuations of the close motors strongly affect the tracer particle fluctuations, which results in higher probabilities for large displacements of the tracer. Our central result is that these higher probabilities are found at specific, discrete distances, and appear as peaks or shoulders in the displacement distributions. This is in contrast with the more common exponential tails found previously in other active systems. These active events, with their discrete features, are a result of active processes which have a cut-off distance, or a characteristic length-scale. Using a simplified simulation, with either a cut-off or characteristic length of these events, we have reproduced the shoulders and peaks in the distributions, supporting our arguments. To estimate the number of motors that strongly influence the tracer particles, i.e., which are in close proximity to them, we suggested that the definition of "close enough" is related to the cross-over distance between intermediate to bulk response of the network. The cross-over distance can be measured using 2P microrheology and is on the order of a few microns (3-5 μm), depending on the motor cluster size and concentration. This implies that inside this close volume there are only a few active motor filaments (1-10).

The precise nature of these motor-driven events is not clear; it could be any number of processes such as recoil due to the release of a motor mini-filament from the actin network, or the tearing/buckling of an actin filament. In any case, the build-up tension, as a result of the motor sliding along two actin filaments, is released and creates the large fluctuations in the tracer particles' motion. We showed that estimates of the forces creating these large displacements are on the order of the force applied by one single head stroke.

Chapter 5

Summary and future directions

In this thesis I have described a detailed investigation of structural, dynamical and rheological properties of three systems, by the use and further extension of the tools of microrheology. In the following sections I will emphasize our main results from these studies and discuss possible future directions for the research.

5.1 Colloidal suspension near a rigid wall

Our central result from the study on sedimented colloidal suspensions above a rigid wall is a rather sharp transition from one-layer to two-layer structure at area fractions of ~ 0.3 . This value is much lower than the area fraction required for close-packing or other 2D structural changes such as the formation of hexatic or crystalline order. This transition has consequences for the diffusivity of the suspension and its density dependence, and therefore on the correct interpretation of its rheological properties. We also demonstrated that polydispersity has a strong effect on the structure and dynamics of colloidal particles sedimented above the wall, because of particle size segregation due to gravity.

There are many future directions to this work, and here I mention two. The experimental studies described in the first article of Sec. 3.3 analyzed the dynamics of

the colloids only in terms of self-diffusion. A natural continuation of the project will be to measure the correlated diffusion of such quasi-2D suspensions as the particle density increases. In contrast to quasi-2D suspensions confined between two parallel walls, where there is no effect of density on the correlated long-range diffusion [109], there is a theoretical prediction for an increase in the correlated long-range diffusion near a single wall as density increases [110]. This prediction is very surprising, as it suggests that the viscosity of the suspension decreases as particle density increases, and it will be very interesting to verify or disprove it. From an experimental point of view, there are several challenges in measuring these correlations. The long-range correlated diffusion in a quasi-2D suspension near a single wall is $D_{\parallel} \sim h^2/r^3$, which applies for distances $r \gg h$, larger than the distance of the monolayer from the wall, h . However, since the correlation decays fast ($\sim r^{-3}$), experimentally it is hard to extract a meaningful signal at these distances. In addition, as we showed in our work, at relatively low area fraction the monolayer transforms into a double-layer structure, and measurements of the correlations become even more challenging.

A biology-inspired problem is the dynamics of particles near a fluctuating surface, which can be related to diffusion in blood vessels and near cell membranes. A natural future direction for our research on particle dynamics near a single wall is to replace the no-slip hard wall with a soft elastic surface. In this scenario, the dynamics of the particles can be studied in passive conditions, where the soft wall undergoes only thermal (equilibrium) fluctuations, and in active conditions, where external forces create non-equilibrium fluctuations in the wall. The self as well as the correlated diffusion of particles suspended adjacent to such a wall are highly interesting, and are expected to show a viscoelastic character although the particles are suspended inside a purely viscous fluid. In this experimental system several questions can be addressed relating to the structure and dynamics of the particles as density increases, or as the strength of non-equilibrium forces are increased.

5.2 Actin networks

Passive entangled networks - the intermediate response

Our study on the microrheology of entangled actin networks resulted in several important outcomes; The first is the discovery of the intermediate response of complex fluids. The second is the development of a new characterization tool for complex fluids, based on a new analysis scheme for microrheology experiments. This new tool offers an extended rheological characterization of complex fluids as well as a measurement tool for their dynamic correlation length. Thirdly, the differentiation between dynamic and static correlation lengths in actin networks. This was achieved by introducing a third length-scale to the system, the filament length. Contrary to the prevailing view, according to de Gennes, that the dynamic correlation length is equivalent to the structural mesh size of the network, we found that the dynamic correlation length depends also on the third length scale once it enters the newly discovered intermediate regime (i.e., when it is still much larger than the mesh size). This finding emphasizes how the response at intermediate distance can influence the dynamical properties of the material, or vice versa.

A future continuation of our research is to study the nature of the relations between the viscoelastic properties of a complex fluid, its dynamic correlation length and its structure. This direction requires the detailed investigations of several conditions in which two independent length scale (e.g., mesh size and filament length) are changes systematically.

Since the micron-scale intermediate response should have an important role in cellular viscoelasticity, a natural continuation of the research is to apply the new characterization tool to investigate cellular-like environments, such as *in-vitro* reconstituted networks based on the cytoskeletal proteins. The advantage of studying *in-vitro* networks is the ability to control the ingredients of the systems, which allows a detailed and precise study of the network properties as a function of the addition or change in concentration of each component.

During our work on active actin-myosin networks discussed on Chapter 4,

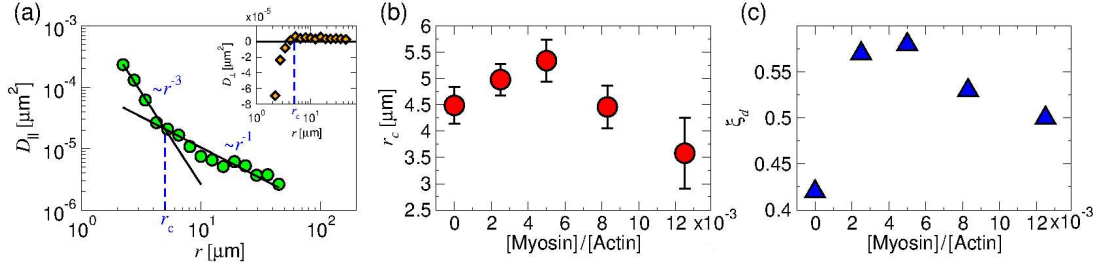


Figure 5.1: Application of Our new characterization tool to active actin-myosin networks. (a) Longitudinal displacement correlation as a function of particle separation at a lag-time $\tau = 0.014$ s. Inset: transverse correlation at the same lag-time. Blue dashed lines correspond to cross-over distance between intermediate and bulk regimes. Network parameters: $[\text{Myosin}]/[\text{Actin}] = 0.0025$, $a = 0.55 \mu\text{m}$. (b) cross-over distance, r_c for networks with increasing myosin concentrations ($N_{myo} = 19$). (c) Dynamic correlation length measured using our new analysis tool for networks with increasing myosin concentrations.

we have identified the three characteristics of the intermediate response in these network; (i) $D_{\parallel} \sim r^{-3}$, (ii) negative D_{\perp} , and (iii) cross-over distance $r_c \gg \xi_s$ much larger than the network mesh size (Fig. 5.1(a)). We have applied our new tool and extracted the dynamic correlation length on these active networks as a function of increasing myosin concentrations (Fig. 5.1(b) and (c)). This analysis suggests that the addition of myosin motors to the networks results in a reorganization of the structure that creates larger network mesh sizes. This result is an intuitive one, as myosin motors are known to reorganized actin networks, however, to confirm it, the validity of the GSER must be considered (as microrheology is based on its validity). It was shown by other groups that the GSER may be valid in active systems [34]. The future work should concentrate on this direction, in one of two relevant approaches; to confirm that the GSER works in these active systems, by for example a combination of active and passive microrheology measurements (as was done in [34]), or to bypass the validity issue and characterize the structure of the network independently and compare the trends.

Fluctuation in active networks

We investigated the fluctuations of particles in active actin-myosin networks as discussed in chapter 4. Contrary to the commonly found distribution of step sizes, which features Gaussian or exponential distributions, we observed a sequence of distinct shoulders and peaks in the distribution, indicating discrete events of motor activity. Our interpretation for these features was that motors induce active events with a cut-off in their distance, and we supported it by simplified simulations. We used these observations further to estimate the force that a single motor exerts on the network.

Our research on the fluctuations in active networks is missing the information regarding the mechanical properties of the gels. This may be measured independently by active microrheology. This important future experimental extension will provide the knowledge regarding the true stiffening of the network and will enable better understanding of how the motors affect the network's fluctuations and rheology.

Another future direction is to study the dynamics of actin networks near a substrate. This scenario is very relevant to several biological systems, such as the actin cortex. In this future direction there are many possibilities, such as using a rigid or a soft wall as the substrate, and using passive cross-linked network or active networks with myosin motors.

Bibliography

- [1] N. J. Wagner and J. F. Brady, *Phys. Today* **62**, 27 (2009).
- [2] R. G. Larson, *The Structure and Rheology of Complex fluids* (Oxford University Press, New York, 1999).
- [3] T. G. Mason and D. A. Weitz, *Phys. Rev. Lett.* **74**, 1250 (1995).
- [4] T. M. Squires and T. G. Mason, *Annu. Rev. Fluid Mech.* **42**, 413 (2010).
- [5] T. A. Waigh, *Rep. Prog. Phys.* **68**, 685 (2005).
- [6] M. L. Gardel, M. T. Valentine, and D. A. Weitz, in *Microrheology*, edited by K. S. Breuer (Springer, Berlin, 2005), p. 150.
- [7] G. G Stokes, *Trans. Camb. Phil. Soc.* **9**, 8 (1851).
- [8] Ke Xu, M. Gregory Forest, and Isaac Klapper, *Journal of Non-Newtonian Fluid Mechanics* **145**, 150 (2007), m32.
- [9] A. J. Levine and T. C. Lubensky, *Phys. Rev. Lett.* **85**, 1774 (2000).
- [10] J. C. Crocker and B. D. Hoffman, *Cell Mechanics*, Vol. 83 of *Methods in Cell Biology* (Elsevier Academic Press Inc, ADDRESS, 2007), pp. 141–178.
- [11] T. G. Mason, *Rheol. Acta* **39**, 371 (2000).
- [12] B. R. Dasgupta, S. Tee, J. C. Crocker, B. J. Frisken, and D. A. Weitz, *Phys. Rev. E* **65**, 051505 (2002).

- [13] T. B. Liverpool and F. C. MacKintosh, *Phys. Rev. Lett.* **95**, 208303 (2005).
- [14] T. Li, S. Kheifets, D. Medellin, and M. G. Raizen, *Science* **328**, 1673 (2010).
- [15] R. Huang, I. Chavez, K. M. Taute, B. Lukic, S. Jeney, M. G. Raizen, and E.-L. Florin, *Nat. Phys.* **7**, 576 (2011).
- [16] M. T. Valentine, P. D. Kaplan, D. Thota, J. C. Crocker, T. Gisler, R. K. Prud'homme, M. Beck, and D. A. Weitz, *Phys. Rev. E* **64**, 061506 (2001).
- [17] I. Y. Wong, M. L. Gardel, D. R. Reichman, E. R. Weeks, M. T. Valentine, A. R. Bausch, and D. A. Weitz, *Phys. Rev. Lett.* **92**, 178101 (2004).
- [18] J. Liu, M. L. Gardel, K. Kroy, E. Frey, B. D. Hoffman, J. C. Crocker, A. R. Bausch, and D. A. Weitz, *Phys. Rev. Lett.* **96**, 118104 (2006).
- [19] B. R. Dasgupta and D. A. Weitz, *Phys. Rev. E* **71**, 021504 (2005).
- [20] D. C. Morse, *Macromolecules* **31**, 7030 (1998).
- [21] R. Verma, J. C. Crocker, T. C. Lubensky, and A. G. Yodh, *Phys. Rev. Lett.* **81**, 4004 (1998).
- [22] R. Verma, J. C. Crocker, T. C. Lubensky, , and A. G. Yodh, *Macromolecules* **33**, 177 (2000).
- [23] A. J. Levine and T. C. Lubensky, *Phys. Rev. E* **63**, 041510 (2001).
- [24] J. L. McGrath, J. H. Hartwig, and S. C. Kuo, *Biophys. J.* **79**, 3258 (2000).
- [25] M. T. Valentine, Z. E. Perlman, M. L. Gardel, J. H. Shin, P. Matsudaira, T. J. Mitchison, and D. A. Weitz, *Biophys. J.* **86**, 4004 (2004).
- [26] J. C. Crocker, M. T. Valentine, E. R. Weeks, T. Gisler, P. D. Kaplan, A. G. Yodh, and D. A. Weitz, *Phys. Rev. Lett.* **85**, 888 (2000).
- [27] L. D. Landau and E. M. Lifshitz, *Theory of Elasticity*, 3rd ed. (Pergamon Press, Oxford, 1986).

- [28] Jens-Christian Meiners and Stephen R. Quake, *Phys. Rev. Lett.* **82**, 2211 (1999).
- [29] *Colloidal Dispersion*, edited by W. Russel, D. Saville, and W. Schowalter (Cambridge University Press, Cambridge, UK, 1989).
- [30] G. K. Batchelor, *J. Fluid Mech.* **74**, 1 (1976).
- [31] J. H. Shin, M. L. Gardel, L. Mahadevan, P. Matsudaira, and D. A. Weitz, *Proc. Natl. Acad. Sci. U.S.A* **101**, 9636 (2004).
- [32] T. M. Squires, *Langmuir* **24**, 1147 (2008).
- [33] T. M. Squires and J. F. Brady, *Phys. Fluids* **17**, (2005).
- [34] D. Mizuno, C. Tardin, C. F. Schmidt, and F. C. MacKintosh, *Science* **315**, 370 (2007).
- [35] D. T. Chen, E. R. Weeks, J. C. Crocker, M. F. Islam, R. Verma, J. Gruber, A. J. Levine, T. C. Lubensky, and A. G. Yodh, *Phys. Rev. Lett.* **90**, 108301 (2003).
- [36] I. A. Hasnain and A. M. Donald, *Phys. Rev. E* **73**, 031901 (2006).
- [37] Jacob N. Israelachvili, *Intermolecular and Surface Forces* (Academic Press, London, 1992).
- [38] B. Derjaguin and L. Landau, *Acta Physicochim URSS* **14**, 633 (1941).
- [39] E. J. W. Verwey and J. T. G. Overbeek, *Theory of the Stability of Lyophobic Colloids* (Elsevier Publishing Company, Inc., Amsterdam, 1948).
- [40] P.G. de Gennes, *Advances in Colloid and Interface Science* **27**, 189 (1987).
- [41] F. Th. Hesslink, *The Journal of Physical Chemistry* **75**, 65 (1971).
- [42] A. Vrij, *Pure Appl. Chwm.* **48**, 471 (1976).

- [43] S. T. Milner, T. A. Witten, and M. E. Cates, *Macromolecules* **21**, 2610 (1988).
- [44] A. Einstein, *Investigations on the Theory of Brownian Movement* (Dover:, New York, 1956).
- [45] J. Happel and H. Brenner, *Low Reynolds Number Hydrodynamics* (Martinus Nijhoff:, The Hague, 1983).
- [46] H. Diamant, *Isr. J. Chem.* **47**, 225 (2007).
- [47] D. C. Prieve, *Adv. Colloid Interface Sci.* **82**, 93 (1999).
- [48] D. H. Van Winkle and C. A. Murray, *J. Chem. Phys.* **89**, 3885 (1988).
- [49] P. González-Mozuelos, M. Medina-Noyola, B. D'Aguanno, J. M. Méndez-Alcaraz, and R. Klein, *J. Chem. Phys.* **95**, 2006 (1991).
- [50] A. Pralle, E.-L. Florin, E.H.K. Stelzer, and J.K.H. Hrber, *Appl. Phys. A* **66**, S71 (1998).
- [51] V. N. Michailidou, G. Petekidis, J. W. Swan, and J. F. Brady, *Phys. Rev. Lett.* **102**, 068302 (2009).
- [52] J. R. Blake, *Proc. Camb. Philos. S-M* **70**, 303 (1971).
- [53] C. Pozrikidis, *Boundary Integral and Singularity Methods for Linearized Viscous Flow* (Cambridge University Press, New York, 1992).
- [54] F. C MacKintosh and C. F Schmidt, *Curr. Opin Cell Biol.* **22**, 29 (2010).
- [55] B. Alberts, A. Johnson, J. Lewis, K. Roberts M. Raff, and P. Walter, *Molecular Biology of the Cell* (Garland Science, New York, 2002).
- [56] D. Bray, *Cell Movements* (Garland Publishing, Inc, New York & London, 1992).
- [57] H. Kojima, A. Ishijima, and T. Yanagida, *Proc. Natl. Acad. Sci. U.S.A* **91**, 12962 (1994).

- [58] F. Gittes, B. Mickey, J. Nettleton, and J. Howard, *J. Cell. Biol.* **120**, 923 (1993).
- [59] A. Ott, M. Magnasco, A. Simon, and A. Libchaber, *Phys. Rev. E* **48**, R1642 (1993).
- [60] J. M. Schurr and K. S. Schmitz, *Annu. Rev. Phys Chem.* **37**, 271 (1986).
- [61] P. A. Janmey and R. T. Miller, *J. Cell Sci.* **124**, 9 (2011).
- [62] C. F. Schmidt, M. Barmann, G. Isenberg, and E. Sackmann, *Macromolecules* **22**, 3638 (1989).
- [63] P.-G. de Gennes, *Macromolecules* **9**, 587 (1976).
- [64] P.-G. de Gennes, *Macromolecules* **9**, 594 (1976).
- [65] T. Gisler and D. A. Weitz, *Phys. Rev. Lett.* **82**, 1606 (1999).
- [66] M. Doi and S. F. Edwards, *The Theory of Polymer Dynamics* (Clarendon Press, Oxford, 1988).
- [67] H. Isambert and A. C. Maggs, *Macromolecules* **29**, 1036 (1996).
- [68] A. Palmer, T. G. Mason, J. Y. Xu, S. C. Kuo, and D. Wirtz, *Biophys. J.* **76**, 1063 (1999).
- [69] T. D. Pollard, L. Blanchoin, and R. D. Mullins, *Annual Review of Biophysics and Biomolecular Structure* **29**, 545 (2000).
- [70] J. Kas, H. Strey, D. Finger, R. Ezzell, E. Sackmann, and P. A. Janmey, *Biophys. J.* **70**, 609 (1996).
- [71] M. L. Gardel, M. T. Valentine, J. C. Crocker, A. R. Bausch, and D. A. Weitz, *Phys. Rev. Lett.* **91**, 158302 (2003).
- [72] P. A. Janmey, S. Hvidt, J. K?s, D. Lerche, A. Maggs, E. Sackmann, M. Schliwa, and T. P. Stossel, *J. Biol. Chem.* **269**, 32503 (1994).

- [73] J. T. Finer, R. M. Simmons, and J. A. Spudich, *Nature* **368**, 113 (1994).
- [74] M. L. Gardel, J. H. Shin, F. C. MacKintosh, L. Mahadevan, P. Matsudaira, and D. A. Weitz, *Science* **304**, 1301 (2004).
- [75] C. P. Brangwynne, G. H. Koenderink, F. C. MacKintosh, and D. A. Weitz, *Phys. Rev. Lett.* **100**, 118104 (2008).
- [76] G. H. Koenderink, Z. Dogic, F. Nakamura, P. M. Bendix, F. C. MacKintosh, J. H. Hartwig, T. P. Stossel, and D. A. Weitz, *Proc. Natl. Acad. Sci. U.S.A* **106**, 15192 (2009).
- [77] T. Toyota, D. A. Head, C. F. Schmidt, and D. Mizuno, *Soft Matter* **7**, 3234 (2011).
- [78] B. Stuhrmann, M. S. E. Silva, M. Depken, F. C. MacKintosh, and G. H. Koenderink, *Phys. Rev. E* **86**, 020901 (2012).
- [79] Marina Soares e Silva, Bjorn Stuhrmann, Timo Betz, and Gijse H Koenderink, *New J. Phys.* **16**, 075010 (2014).
- [80] M. Norstrom and M. L. Gardel, *Soft Matter* **7**, 3228 (2011).
- [81] O. Lieleg, M. M. A. E. Claessens, and A. R. Bausch, *Soft Matter* **6**, 218 (2010).
- [82] F Backouche, L Haviv, D Groswasser, and A Bernheim-Groswasser, *Phys. Biol.* **3**, 264 (2006).
- [83] Y. Ideses, A. Sonn-Segev, Y. Roichman, and A. Bernheim-Groswasser, *Soft Matter* **9**, 7127 (2013).
- [84] S. Kohler, V. Schaller, and A. R. Bausch, *Nat. Mater.* (2011).
- [85] D. Smith, F. Ziebert, D. Humphrey, C. Duggan, M. Steinbeck, W. Zimmermann, and J. Kas, *Biophys. J.* **93**, 4445 (2007).
- [86] M. Soares e Silva, M. Depken, B. Stuhrmann, M. Korsten, F. C. MacKintosh, and G. H. Koenderink, *Proc. Natl. Acad. Sci. U.S.A* **108**, 9408 (2011).

- [87] A. E. Patteson, A. Gopinath, P. K. Purohit, and P. E. Arratia, arXiv:1505.05803 .
- [88] E. Hamoy and M. N. Confesor, IOP Conf. Ser.: Mater. Sci.Eng. **79**, 012013 (2015).
- [89] O. J. N. Bertrand, D. K. Fyngenson, and O. A. Saleh, Proc. Natl. Acad. Sci. U.S.A **109**, 17342 (2012).
- [90] Kyriacos C. Leptos, Jeffrey S. Guasto, J. P. Gollub, Adriana I. Pesci, and Raymond E. Goldstein, Phys. Rev. Lett. **103**, 198103 (2009).
- [91] É. Fodor, M. Guo, N. S. Gov, P. Visco, D. A. Weitz, and F. van Wijland, Europhys. Lett. **110**, 48005 (2015).
- [92] T. Funatsu, Y. Harada, M. Tokunaga, K. Saito, and T. Yanagida, Nature **374**, 555 (1995).
- [93] K. Kitamura, M. Tokunaga, A. H. Iwane, and T. Yanagida, Nature (1999).
- [94] S. M. Block, L. S. B. Goldstein, and B. J. Schnapp, Nature **348**, 348 (1990).
- [95] E. Reisler, C. Smith, and G. Seegan, Journal of Molecular Biology **143**, 129 (1980).
- [96] T. Hayashi and K. Maruyama, J. Biochem. **78**, 1031 (1975).
- [97] L. Haviv, D. Gillo, F. Backouche, and A. Bernheim-Groswasser, J. Mol. Biol. **375**, 325 (2008).
- [98] J. A. Spudich and S. Watt, J. Biol. Chem. **246**, 4866 (1971).
- [99] S. S. Margossian and S. Lowey, Methods Enzymol. **85**, 55 (1982).
- [100] J. C. Crocker and D. G. Grier, J. Colloid Interf. Sci. **179**, 298 (1996).
- [101] M. P. Lettinga and E. Grelet, Phys. Rev. Lett. **99**, 197802 (2007).

- [102] H. Lee, J. M. Ferrer, F. Nakamura, M. J. Lang, and R. D. Kamm, *Acta Biomater.* **6**, 1207 (2010).
- [103] S. Burov, S. M. A. Tabei, T. Huynh, M. P. Murrell, L. H. Philipson, S. A. Rice, M. L. Gardel, N. F. Scherer, and A. R. Dinner, *Proc. Natl. Acad. Sci. U.S.A* **110**, 19689 (2013).
- [104] M. J. Tyska, D. E. Dupuis, W. H. Guilford, J. B. Patlak, G. S. Waller, K. M. Trybus, D. M. Warshaw, and S. Lowey, *Proc. Natl. Acad. Sci. U.S.A.* **96**, 4402 (1999).
- [105] A. Sonn-Segev, A. Bernheim-Groswasser, H. Diamant, and Y. Roichman, *Phys. Rev. Lett.* **112**, 088301 (2014).
- [106] A. Sonn-Segev, A. Bernheim-Groswasser, and Y. Roichman, *Soft Matter* **10**, 8324 (2014).
- [107] O. Siton-Mendelson, B. Gilboa, Y. Ideses, and A. Bernheim-Groswasser, in *Cell and Matrix Mechanics*, edited by R. Kaunas and A. Zemel (CRC Press, Boca Raton, 2015), Chap. 3.
- [108] E. Ben-Isaac, É. Fodor, P. Visco, F. van Wijland, and Nir S. Gov, *Phys. Rev. E* **9**, 012716 (2015).
- [109] B. Cui, H. Diamant, B. Lin, and S. A. Rice, *Phys. Rev. Lett.* **92**, 258301 (2004).
- [110] H. Diamant, Unpublished results .

תקציר

עבודה זו מתארת את היישום של מיקרוראולוגיה במטרה לאפיין את התכונות המבניות, הדינמיות והמכניות של שלושה חומרים רכים וצפופים: תרחיף קולואידים קוואזי-דו-ממדי ליד קיר קשיח, רשת אקטין סבוכה, ורשת אקטין-מיוזין אקטיבית. אנו מדגימים כיצד, מתוך חקירה של תנודות החלקיקים המוטמעים בתוך החומר בלבד, מתקבל מידע רב על המבנה, הדינמיקה והמכניקה של החומר, והיחסים בין תכונות חומר אלו.

המערכת הראשונה שנחקרה היא תרחיף של קולואידים מסיליקה, השוקעים במים ויוצרים תרחיף קוואזי-דו-ממדי מעל למצע שטוח. בדקנו ניסיונית את המבנה והדינמיקה של תרחיפים אלו ככל שצפיפותם גדלה, כלומר ככל שהריכוז השטחי של החלקיקים גדל. החקירה המפורטת כללה הדמייה תלת-מימדית באמצעות שתי שיטות בלתי-תלויות, הדמייה הולוגרפית וקונפוקלית, ובנוסף כללה גם הדמייה דו-מימדית על ידי מיקרוסקופיה פלואורסצנטית. מיקום החלקיקים ותנועתם נותחו וחשפו היווצרות חדה למדי של שכבה שניה ברורה בריכוז שטחי של $0.3 \sim$, ריכוז נמוך בהרבה מזה של האריזה הצפופה. מצאנו כי המעבר למבנה דו-שכבתי, המונע מאנטרופיה, משפיע באופן משמעותי על דיפוזיית החלקיקים הסמוכים למשטח, ועל תלות הדיפוזיה בריכוז החלקיקים. התוצאות הניסיוניות הללו אומתו ע"י סימולציות מחשב.

בסדרת הניסיונות השניה חקרנו את המיקרוראולוגיה של רשתות אקטין סבוכות, מערכת מודל לפולימרים גמישים-למחצה. אנליזה זהירה של ניסיונות מיקרוראולוגיה דו-חלקיקית הובילו אותנו לגילוי תחום חדש של תגובה מכנית ברשתות אקטין, בתחום ביניים של מרחקים. זאת למרות העובדה שהמיקרוראולוגיה של רשתות אקטין נחקרה באופן נרחב בעבר. תגובת הביניים נצפתה במרחקים מפתיעים בגודלם, מסדר גודל של מיקרומטרים אחדים. הסתבר כי תחום תגובה זה הוא בעל אופי כללי הרבה יותר, הרלוונטי לכל נוזל מרוכב המכיל שני מרכיבים. גילוי זה חשף שתכונות החומר הכולל במקרה של נוזלים מרוכבים מופיעות במרחקים גדולים בהרבה מהאורך האופייני של מבנה החומר (לדוגמא, גודל חורי הרשת ברשתות אקטין).

בהמשך, השתמשנו בגילוי תחום תגובת הביניים על מנת לפתח שיטת אנליזה חדשה לניסיונות מיקרוראולוגיה, המבוססת על התיאור התיאורטי של תחום זה. בעזרת שילוב של מיקרוראולוגיה חד-חלקיקית ודו-חלקיקית, הצלחנו לחלץ את אורך הקורלציה הדינמי של רשתות אקטין כתלות במספר פרמטרים, כגון ריכוז ואורך סיב האקטין. עבודה זאת מציגה כלי אפיון חדש לנוזלים מרוכבים. יישום שיטת האנליזה החדשה שלנו על רשתות אקטין עם אורכי סיב משתנים, אפשרה לנו לבדוק את היחס בין אורכי הקורלציה הדינמי והסטטי. בניגוד לדעה הרווחת שאורך הקורלציה הדינמי שקול לאורך הקורלציה של מבנה הרשת, מצאנו שאורך הקורלציה הדינמי מתחיל לגדול כאשר אורך סיב האקטין הוא מסדר גודל של אורך תחום הביניים שהתגלה על ידינו (כלומר כאשר הוא עדיין גדול בהרבה מגודל חורי הרשת).

בסדרת הניסיונות האחרונה, חקרנו את התנודות של חלקיקים בתוך מערכת מודל של חומר רך אקטיבי: ג'ל של אקטין-מיוזין אקטיבי. אופי הדינמיקה מחוץ לשיווי משקל של רשתות אלו נחקר בתנאים שבהם האקטיביות שלהם השתנתה, אם על ידי הגדלת ריכוז המנועים או על ידי שינוי הגודל של חלבוני המנוע. במהלך האנליזה של תנועת החלקיקים המוטמעים ברשתות, הבחנו שבריכוז מנועים גבוה דיו התפלגות גדלי הצעדים של החלקיקים מתאפיינת בסדרה של פסגות ברורות בגדלי צעד גדולים, המצביעים על אירועים בדידים של פעילות המנועים. תצפית זו שונה מההתפלגויות שנמדדו במערכות אקטיביות, אשר מתאפיינות בסטטיסטיקה גאוסיאנית או אקספוננציאלית. פסגות אלו בהתפלגות הן תוצאה של תהליכים אקטיביים ברשת שיש להם אורך אופייני, או מרחק מרבי. ביצענו סימולציות פשוטות ששחזרו את הסמנים של ההתפלגויות שראינו בניסוי, וכך תומכות בפרשנות שלנו לתוצאות אלו. יתר על כן, השתמשנו בהבחנות הללו בכדי להעריך את הכוח שמנוע בודד מפעיל על הרשת.

עבודה זו נעשתה בהנחייתם של

ד"ר יעל רויכמן

פרופ' חיים דימנט

ביה"ס לכימיה, אוניברסיטת תל אביב

מיקרואולוגיה של מערכות צפופות

חיבור לשם קבלת התואר דוקטור לפילוסופיה

מאת

אדר סון-שגב

הוגש לסנאט של אוניברסיטת תל אביב

חשוון תשע"ז

נובמבר 2016